PERMEABILITY UPSCALING: A MODELING INVESTIGATION OF GAS MINIPERMEAMETERS

by

Justin Jayne

Department of Earth &
Environmental Science
New Mexico Tech
Socorro, NM 87801

Submitted in Partial Fulfillment

of the Requirements for the Degree of

Master of Science in Hydrology

New Mexico Institute of Mining and Technology

Socorro, New Mexico

December, 2004

ABSTRACT

Because of technological limitations, the scale of property heterogeneity that can be represented with a computational model is significantly larger than the scale at which properties are measured by most instruments. Consequently, techniques are needed to upscale and synthesize small-scale measurements to infer larger scale effective properties. Laboratory upscaling experiments were conducted by Tidwell and Wilson [2000] using an automated gas minipermeameter system. Repeated permeability measurements on geologic samples showed different but related patterns of spatial variability at different sample supports and, depending on the rock, different upscaling behavior.

We numerically simulated a field of log permeability values prescribed to geostatistically replicate a block of Massillon sandstone. Log permeability values were simulated using sequential Gaussian simulation on a block-centered grid using laboratory data to prescribe geostatistical parameters. The operation of a steady-state gas minipermeameter was modeled by means of the finite-difference method. The laboratory multisupport minipermeameter allows for highly resolved gridded measurements to be made using a set of five interchangeable tip-seals, each twice the size of the next, ranging in inner radius from 0.15 cm to 2.54 cm. The numerical scheme that models the multisupport

minipermeameter replicates change of sample support by holding constant the boundary conditions representing the tip-seal (thereby maintaining constant flow geometry) while repeatedly doubling the resolution of the grid, effectively mimicking the corresponding halving of tip-seal dimensions. The x-y positioner that moves the tip-seal of the multisupport minipermeameter across the face of the rock sample is numerically modeled by shifting the grid of log permeability values row by row relative to the fixed boundary conditions. The multisupport minipermeameter made measurements on a 50×50 grid; due to the time required to perform the computations, the numerical experimental measurement "grid" consists of a transect of 100 points.

Effective log permeability measurements show that the numerically modeled minipermeameter capably replicates the operation of the laboratory instrument. The variance of the numerical effective log permeability decreases as tip-seal size increases, as does the variance of the laboratory data set. This result is consistent with the simple averaging characteristic of both the measurement grid and the change of sample support. In addition, semivariograms calculated from numerical effective log permeabilities show patterns similar to those of the laboratory data, namely that the sill decreases and the range increases as tip-seal size increases. The behavior of the sill is simply a reflection of the upscaling of the variance, and the behavior of the range reflects the fact that as the tip seal size increases, two measurements must be separated that

much farther apart before they become uncorrelated.

The numerical experiment allows for comparison between the numerical effective log permeability and the underlying synthetic log permeability field. In an effort to determine how well the instrument characterizes the spatial structure of the field it samples, we determined that it is neither possible for an instrument to resolve features of the target field smaller than twice the characteristic length (in this case the inner tip-seal radius), nor can a set of measurements made on a regular grid fully resolve features at scales less than twice the measurement grid interval. This result is consistent with the sampling theorem of Fourier analysis. In addition, comparison between the numerical effective log permeability and the mean of the log synthetic permeability field confirms that the two variables are strongly correlated and that minipermeameter measurements of heterogeneous permeability fields are most strongly correlated with the regions of the field that lie nearest the inner and outer edges of the tip-seal. This results confirms the spatial weighting function theories proposed by Aronson [2001] and Molz, et al. [2003] for homogeneous fields.

Though the numerical experiment replicates many operational characteristics of a physical minipermeameter, it failed to capture the most important feature of the laboratory experiment: the upscaling of the mean effective log permeability. While the laboratory values show a strong upward trend as the

tip-seal size increases, the numerical results are essentially flat. The fundamental physical reason for this is that the laboratory sample allows the development of fast flow paths as tip-seal size increases. We identified three primary causes for the failure of the numerical experiment to reproduce the mean upscaling seen in the laboratory. First, small-scale structures of the laboratory sample are not measured by the laboratory instrument, primarily because of the limitations of bandwidth noted above. As a result, these high spatial frequency features are not simulated in the synthetic log permeability field, based as it is on the laboratory data set. Second, the simulated field is assumed to be lognormally distributed, which is an incorrect parameterization of the laboratory measurements. As a result, the semivariogram of the synthetic log permeability field is only approximately representative of the laboratory version. Third, qualitative features of the laboratory measurements are not replicated by the simulation. The sequential Gaussian simulation routine fails to replicate the zones of depositionally related cross-strata unconformably separated by low permeability bounding surfaces. These three shortcomings, at a minimum, should be addressed in order to create a faithful replica of the laboratory sample which will demonstrate effective mean log permeability upscaling.

ACKNOWLEDGMENTS

I wish to thank the members of my committee, Dr. John L. Wilson, Dr. Vincent C. Tidwell and Dr. Fred Phillips for their effort, time and encouragement in seeing me through this project. I give particular acknowledgement to Dr. Wilson and Dr. Tidwell, whose constant guidance and stellar example have proved invaluable over the years.

I offer my thanks to Dr. Steve Schafer, for his patient instruction in the early days of this project; Dr. Edward Bolton, for opening the doors at Yale and providing support and insight during my year in New Haven, Dr. Leo Hickey and the Department of Geology and Geophysics at Yale University, for giving me a home away from home and making available the resources without which this work could not have been done; Dr. Gilbert Kerr and Dr. Carl Axness for lending much needed mathematical insight; and Dr. Roseanna Neupauer for aiding in the typesetting of this document. Special thanks are owed to Dr. Annette Schafer, who provided FDM, the flow code on which this research is built, as well as her tutelage, insight and example.

My deepest thanks go to my wife, Kaatje. Only with your support, encouragement and inspiration have I gotten this far.

This report was typeset with LaTeX[1] by the author.

TABLE OF CONTENTS

LIST OF TABLES

LIST OF FIGURES

vii

viii

ix

xiii

This report is accepted on behalf of the faculty of the Institute by the following committee:

_____

John L. Wilson, Advisor

_____

_____

_____

Justin Jayne   Date

NOMENCLATURE

∇	gradient operator, $\frac{\partial}{\partial x}\tilde{\mathbf{e}}_x + \frac{\partial}{\partial y}\tilde{\mathbf{e}}_y + \frac{\partial}{\partial z}\tilde{\mathbf{e}}_z$
a	inner tip-seal radius
b	outer tip-seal radius
b_d	dimensionless outer tip-seal radius, equal to $\frac{b}{a}$
a_{eff}	effective inner tip-seal radius, equal to $\sqrt{\frac{A_i}{\pi}}$
b_{eff}	effective inner tip-seal radius, equal to $\sqrt{\frac{A_o}{\pi}}$
A_i	discretized area bounded by inner tip-seal radius
A_o	discretized area bounded by outer tip-seal radius
$G_0(b_d)$	analytical geometric factor for the semi-infinite domain
$\widetilde{G_0}(b_d, L_x, L_y, L_z)$	numerical geometric factor for the semi-infinite domain
h	numerical grid separation
k_{eff}	effective permeability
k_{geo}	permeability geometric mean
k_{num}	numerical effective permeability
L_x	length of flow domain in Cartesian x direction
L_y	length of flow domain in Cartesian y direction
L_z	length of flow domain in Cartesian z direction
$m[\cdots]$	arithmetic mean of bracketed quantity
M	molar mass
$\dot{m}$	mass flow rate
p_i	pressure inside tip-seal chamber
p_o	pressure outside tip-seal chamber
$\mathbf{q}_m$	mass flux
Q	volumetric flow rate
R	gas constant
$\mathbf{s}$	lag vector
$\mathbf{s}_d$	dimensionless lag vector
$s^2[\cdots]$	variance of bracketed quantity
T	temperature
$x1$	denotes quantity pertaining to 2.54 cm tip-seal
$x2$	denotes quantity pertaining to 1.27 cm tip-seal
$x4$	denotes quantity pertaining to 0.63 cm tip-seal
$x8$	denotes quantity pertaining to 0.31 cm tip-seal
$x16$	denotes quantity pertaining to 0.15 cm tip-seal
$\gamma(\mathbf{s})$	semivariogram as a function of lag vector $\mathbf{s}$

λ correlation length
μ gas dynamic viscosity
Φ gas pseudo-potential
ρ gas density

CHAPTER 1

INTRODUCTION

1.1   Problem Statement

Groundwater hydrologists depend on simplified abstractions, or models, to represent subsurface flow and transport systems. These models are cast in the form of partial differential equations which in turn are often solved numerically with digital computers. This approach is so ubiquitous that the particular numerical scheme employed is commonly referred to as the "model", a convention we will adhere to herein. A fundamental challenge presented to the modeler is to correctly parameterize the physical properties (porosity, permeability, etc.) of the the porous medium supporting a particular flow and transport system. This challenge appears in the form of two related problems: interpolation and upscaling. The problem of interpolation arises from want of information. The system being modeled can be sampled only sparsely and in a small subset of its extent, necessitating estimation of parameters at unsampled locations. The problem of upscaling arises from the quality of information available. Measurements are typically made at a much smaller scale than that of the model. Upscaling is the process by which properties defined at the measurement scale are assigned to the model scale. Permeability, in particular, is a function of both material properties and the flow geometry imposed by the instrument used to obtain the measurement, so both factors must be taken into account in the upscaling process.

Upscaling, so far as we are concerned, can be construed broadly to mean a method for determining an effective or average property of a heterogeneous porous medium. Couching the properties of the porous medium in the framework of the continuum hypothesis, we suppose that these properties are piecewise continuous fields: every mathematical point in the medium is associated with a property value that we understand to be assigned to a representative elementary volume (REV) centered on the mathematical point [Bear, 1971]. In this sense, we have encountered the upscaling problem at a very basic level. When we agreed to sweep the detailed pore-scale fluid dynamics under the rug and instead concern ourselves with ensemble behavior at the REV scale, sparing us from working directly with the Navier-Stokes equations in the complicated and inaccessible realm of individual pores and allowing us to invoke relatively simple macroscopic equations like Darcy's law, we tacitly invoked an upscaling rule. However, while the REV is large compared to individual pores, it is still small compared to instruments used in the lab or field, so we may regard REV properties as point-scale properties at the lab scale.

At the lab scale, we can formally treat a measurement as a rule specifying how to average point-scale properties to yield an effective property [Beckie, 1996; Desbarats, 1992; Indelman and Dagan, 1993; Oliver, 1990; Rubin and Gomez-Hernandez, 1990]. The volume over which an instrument averages a quality to which it is sensitive is called the sample support. In some cases, the averaging rule depends solely on the intrinsic property of the medium. For example, effective porosity is just the arithmetic mean of the point-scale porosity in the sample support. In other cases the effective property depends on the flow context in which it is measured. Effective permeability, for one, depends on

the geometry of the fluid flow relative to the medium. Famously, for example, a layered system could be correctly parameterized by the arithmetic mean, the harmonic mean or the weighted geometric mean [Desbarats, 1992] depending on whether flow is parallel to the layering, perpendicular to the layering or radial, respectively.

In general, permeability depends on the sample support at which it is measured, as has been demonstrated from both physical [Brace, 1984; Parker and Albrecht, 1987; Clauser, 1992; Hanor, 1993; Schulze-Makuch and Cherkauer, 1997] and computational [Warren and Price, 1961; Desbarats, 1987; Gomez-Hernandez and Gorelick, 1989; Bachu and Cuthiell, 1990; Durlofsky, 1992] experiments. In as much as technological limitations preclude making measurements at the model scale, upscaling from measurement to model parameter is conditioned on spatial statistical characteristics of the point-scale field. These characteristics can be obtained by making multiple measurements on a sampling network [Beckie, 1996]. The efficacy of a sampling campaign depends on both the scale of the sample support of a single measurement (the measurement scale) and the scale of the distance between measurements (the sampling scale). Natural porous media exhibit variability across a range of scales. The measurement scale limits the finest scale over which an effective property can be resolved. As an instrument integrates point-scale properties over its sample support, variation of the field that lies at the scale of the linear dimension of the sample support is lost. Assuming that the sampling scale is larger than the measurement scale, the sampling scale limits both the finest and coarsest scale resolvable by the network of measurement. Spectral analysis shows that the information available from such a network is band-limited. The

Nyquist frequency limits the finest scale theoretically resolvable to twice the smallest distance between measurements; the coarsest scale resolvable is limited to half the greatest distance between measurements [Briggs and Henson, 1995; Bracewell, 2000].

In this research, we examine the effect of both measurement scale and sampling scale on permeability measurements. We have used stochastic simulation to generate a number of synthetic log permeability fields. These fields are subjected to numerical experimentation that simulates measurement of permeability with a gas minipermeameter. The permeameter measurements are made with five "instruments" spanning over three orders of magnitude in sample support arrayed on a regular network. We analyze how measurements made at different scales, but subject to identical flow conditions, relate to one another. We also analyze how a network of such measurements fares at capturing the underlying structure of the synthetic log permeability fields. This computational study parallels laboratory studies performed by Tidwell and Wilson [Tidwell and Wilson, 1997; Tidwell and Wilson, 1999a; Tidwell and Wilson, 1999b; Tidwell et al., 1999; Tidwell and Wilson, 2000]. Tidwell and Wilson developed an apparatus called the multi-support permeameter (MSP) capable of performing just the sort of measurements described above but in the laboratory. They made regularly gridded permeability measurements on rock samples using several different sample supports, different by orders of magnitude on a per volume basis. We use Tidwell and Wilson's work as a starting point, attempting to simulate rock samples that are statistically similar to those tested in the lab by the MSP. We compare the results of our numerical experiments to their laboratory experiments.

The rest of this work is organized as follows. In the remainder of this introductory chapter, we present the specific objectives and scope of our work, discuss the theory and operating principles of gas minipermeameters, and summarize previous work on upscaling. In Chapter 2, we will give an overview of our numerical experimental methods, discussing both the numerical model and the stochastic techniques used to create the synthetic rock samples. In Chapter 3, we present and analyze the results of our numerical experimentation. In Chapter 4, we discuss our conclusions and give recommendations for further work.

1.2 Objective and Scope of Work

The primary objective of this work is to understand the physical processes that contribute to the upscaling of the MSP measurements of the Massillon sandstone. The means to this end is a numerical model of the operation of the MSP on the Massillon sandstone. We conceptually model the permeability of the Massillon as a field of discrete permeability values. Then, we replicate the operation of a gas minipermeameter on the sample by operating on the synthetic permeability field with a linear finite-difference operator that approximates the governing partial differential equation. Solution of the system of difference equations yields an array of pressure values assigned to the points at which we assigned the permeability, from which we can obtain the velocity field and mass transport rate. We then analyze the numerical data to demonstrate similarity to the laboratory data and explore the physical processes that determine the outcome of the measurement.

We designed the series of numerical experiments that closely parallel

(but not replicate) the MSP experiments performed by Tidwell and Wilson [Tidwell and Wilson, 1997; Tidwell and Wilson, 1999a; Tidwell and Wilson, 1999b; Tidwell et al., 1999; Tidwell and Wilson, 2000]. They performed exhaustive measurements on several meter-scale blocks of rock, each representative of a different lithology. Each face was subjected to many thousands of regularly gridded measurements. In the case of the Massillon sandstone, the measurement grid consisted of a 50×50 array, with 1.27 cm grid separation. At each point in the grid, multiple measurements were made with instruments having inner tip-seal radii of 0.15 cm, 0.31 cm, 0.63 cm, 1.27 cm and 2.54 cm, spanning 3.7 orders of magnitude in volumetric sample support. In this work, we simulated only one of the rock samples, a Massillon sandstone, and performed measurements on only one face. Rather than sampling on a square grid, we sampled one hundred points along a single transect. Otherwise, we attempted to retain the same measurement and sampling scales.

Our analysis parallels the statistical approach followed by Tidwell and Wilson [1997; 1999a; 1999b; 2000] for the laboratory experiment to illuminate the interaction of the measurements with the permeability field. We use published experimental semivariograms calculated from the sets of actual MSP measurements made at the smallest available scale to synthesize the underlying log permeability. Direct comparison of the numerical and laboratory results serves to answer whether the small scale measurements are representative of the true sample log permeability. We also examine the dependence of spatial statistics on sample support.

We also test the hypothesis that the upscaling rule enters a transition

phase when the characteristic linear measurement scale is comparable to the correlation length of the log permeability field. We suppose that when the correlation length is either much less than or much greater than this characteristic measurement scale, that the effective permeability is well represented by the geometric mean of the permeability within some neighborhood of the sample support. However, when the correlation length is very near to the characteristic measurement scale, we anticipate that there exists the possibility of fast flow paths becoming significant. We test this hypothesis by measuring the correlation between effective permeability measurements and the geometric mean of the permeability within a nested set of sub-volumes centered on the measurement.

1.3 Background

1.3.1 Permeameters

Gas minipermeameters offer a rapid, non-destructive means of evaluating permeability [Goggin, 1988; Davis et al. 1994; Tidwell and Wilson, 1997; Aronson, 1999;]. The instrument we employ in this study injects gas at constant pressure from a compressed gas source into a rock sample while the user monitors applied pressure and flow rate. The flow of gas at the rock face is controlled by an apparatus consisting of a circular aperture, through which the gas flows, surrounded by an annular *tip-seal* of silicone rubber or similar conformable material (fig. 1.1). Permeability is calculated using a modified form of Darcy's law [Goggin et al. 1988]:

$$k_{eff} = \frac{Q \mu p_i}{\left(a G_0 \left(\frac{p_i^2 - p_0^2}{2}\right)\right)}, \tag{1.1}$$
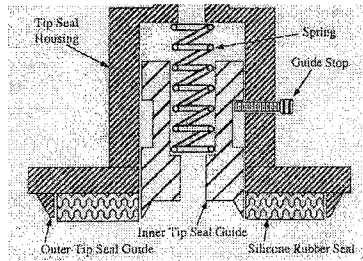
Figure 1.1: Minipermeameter tip-seal [Aronson, 2001]

where k_{eff} is the effective permeability, Q is the volumetric flow rate into the sample, μ is the gas dynamic viscosity, p_i and p_o are the pressure inside the tip-seal chamber and the ambient pressure, respectively, a is the inner tip-seal radius, and G_0 is the geometric factor. G_0 depends on the internal and external radii of the tip-seal and the geometry of the sample domain. Goggin developed tables of geometric factors for cylindrical sample domains using a finite-difference model [1988]. Kerr and Wilson derived an exact analytical solution for a semi-infinite domain [Kerr and Wilson, personal communication, 2001].

The geometry and characteristics of the sample support have been subject to considerable investigation. The sample support for a homogeneous, isotropic semi-infinite half space is approximately hemispherically shaped [Goggin, 1988; Winterbottom, 1990; Aronson, 1999].

Goggin et al. concluded that the difference in permeability between a measurement of effective permeability made on a core plug with a radius and depth of $4a$ (i. e., the radius and depth of the domain are each four times the inner tip-seal radius) and a measurement made on a semi-infinite domain is

less than 5%. Using a finite-difference model, Chen [1992] compared geometric factors obtained for cylindrical domains subject to both first and second type boundary conditions, finding that the geometric factor varied by less than 0.2% for cylindrical domains with radius and depth of $9a$. Chen also determined that almost 40% of the mass flows through the grid-block just inside the tip-seal, and more than 35% exited the sample through the first block outside the tip-seal, noting that these regions contributed the greatest weight to the measurement. Based on laboratory experiments, Suboor and Heller [1995] found that boundary conditions caused effective permeability to vary by less than 1% when the edge of the sample domain was located $2.88a$ from the tip-seal center and the bottom of the sample domain was located $3.50a$ from the tip-seal center. The results cited pertain to the case in which the ratio of outer to inner tip-seal radius, b_d, is 2.

In related work, others have developed *spatial weighting functions*, measures of what regions of the permeability field contribute to the effective permeability. Tidwell et al. [1999] empirically calculated a two-dimensional spatial weighting function using Fourier analysis on gridded MSP measurements. They determined that a cylindrical region with a radius $1.73a$ contributes 90% of the weight of a permeability measurement, and a region with a radius of $1.87a$ contributes 95%. Aronson [1999] used a finite element model to determine that 95% of the contribution to the effective permeability is contained with a cylinder with radius $2.3a$ and depth $3.71a$, and that a 99% contribution is made within a hemisphere of radius $4.16a$. These results arose from Aronson's determination of a spatial weighting function derived by means of adjoint state analysis. Once again, these results are for $b_d = 2$.

Molz et al. [2003] have developed a theory to account for the empirical results given above. Using a streamline-based argument in the context of a steady, homogeneous, and isotropic flow system, they interpreted the spatial weighting function in terms of the ratio of energy dissipation rate per unit volume of porous medium to the total energy dissipation rate over entire flow domain. For non-uniform flow fields, such as that imposed by a gas minipermeameter, this implies that the greatest contribution to the weighting function is made where the magnitude of head gradients is greatest—in the case of the minipermeameter, near the seal boundaries.

1.3.2 Effective Permeability and Upscaling

Permeability upscaling has received wide attention for more than 20 years. By one account [Renard and de Marsily, 1997], compiled six years ago in 1997, more than 200 papers treating this subject appear in the literature. Hence, we will touch on only a few of the most significant theories, focusing on the stochastic theories that provide the framework for this study.

Theories advanced to explain permeability upscaling can broadly be categorized as deterministic, heuristic or stochastic [Renard and de Marsily, 1997; Neuman, 2003]. Deterministic theories are predicated on a complete, a priori knowledge of the permeability field and boundary conditions, and tend to rest on physical arguments. Direct solutions of the flow equation, whether arrived at analytically or numerically, are examples of a deterministic theory. Other examples are streamline-based methods, renormalization and homogeneous-equation methods [Renard and de Marsily, 1997]. Like deterministic theories, heuristic theories require full knowledge of the underly-

ing permeability, but are presented as plausible rules, tending to be purely mathematical in character, for calculating effective permeabilities. Examples of heuristic theories are sampling and various averaging schemes [Renard and de Marsily, 1997].

Our unavoidably incomplete knowledge of how permeability varies in space is addressed by stochastic theories. The stochastic approach to modeling regards permeability as a random variable. A given sample permeability is a single realization of a spatially correlated random function. In the literature, the hypothetical random functions that generate the sample permeability are often considered to be statistically homogeneous or second-order stationary, equivalent terms that indicate the first and second moments (the mean and covariance) of the random variable do not depend on absolute position.

Warren and Price [1961] used a Monte Carlo numerical approach to investigate the effective permeability of heterogeneous formations. Using a three-dimensional finite-difference scheme, they tested spatially uncorrelated lognormal and exponential permeability distributions under conditions of quasi-linear and quasi-radial steady-state flow and quasi-radial transient flow to determine that the geometric mean provided a good estimate of the effective permeability. Matheron [1967] is widely credited [Neuman, 2003; Desbarats, 1987; Desbarats, 1992; Cushman, 1986] with showing rigorously that the effective permeability is equal to the geometric mean in a two-dimensional, lognormally distributed, statistically isotropic medium. This result was confirmed by Dagan [1982]. Gutjahr et al. [1978] used a perturbation approach to calculate the effective permeability in an isotropic, n-dimensional medium, finding that

$$k_{eff} = \bar{k}_{geometric}(1 + (\frac{1}{2} - \frac{1}{n})s^2_{\ln k}), \qquad (1.2)$$

where $\bar{k}_{geometric}$ is the geometric mean of the point-scale permeability, n is the dimension of the medium, and $s^2_{\ln k}$ is the variance of the natural logarithm of the point-scale permeability.

Gelhar and Axness [1983] derived an expression for the effective permeability of a statistically anisotropic medium, proposing that Eq. (1.2) is really just a truncation of the exponential relationship

$$k_{eff} = \bar{k}_{geometric} \exp\left(\frac{1}{2} - \frac{1}{n}\right)s^2_{\ln k}. \qquad (1.3)$$

Neuman [2003] cited this result as originating independently from Landau and Lifshitz [1960] and Matheron [1967]. Dagan [1993] derived an expression for k_{eff} including terms up to order $s^4_{\ln k}$ and found it in agreement with Eq. (1.3). Dykaar and Kitanidis [1992a, 1992b] and Neuman and Orr [1993] and Sanchez-Vila [1995] confirmed Eq. (1.3) for values up to $s_{\ln k} = 7$. Neuman proposed a variation of Eq. (1.3) valid for anisotropic media in [Neuman, 1994].

The theories above assume a sample support that spans many correlation lengths of a statistically homogeneous medium. In this sense, they can be thought of as the limiting case, the upper bound toward which permeability measurements approach as sample support increases. In real geologic samples, permeability seems to change up to the largest observed scales, without appearing to approach an upper bound. One explanation for this is that

permeability possesses structure spanning all scales, so the assumption of statistical homogeneity is never valid. Neuman proposed a universal scaling rule [1990], suggesting that the semivariogram of permeability can loosely be fit to a power model, implying a fractal scaling behavior. Boufadel et al. [2000], Di Frederico and Neuman [1997], Liu and Molz [1997], and Molz et al. [1998] have also elaborated fractal and multifractal scaling theories.

Though considerable work has gone into devising theories to predict the effective permeability of various random fields and into discerning the spatial structure of those fields over many scales, less has been published on how to estimate the spatial structure of the field based on limited samples. In a numerical experiment, Durlofsky [1992] compared sampling (in which the effective permeability of a domain is set to the point-scale value at a single location within that domain), global geometric averaging (in which the the effective permeability of a domain is set to the geometric mean of the permeability of entire domain) and local geometric averaging (in which a domain is subdivided into smaller sub-domains, each possessing an effective permeability equal to the geometric mean of the sub-domain permeability). Examining two-dimensional methods for spatially correlated, lognormal permeability distributions, he determined that local averaging is always more accurate than sampling, that local averaging is more accurate than global averaging , and that sampling is more accurate than global averaging when the size of grid-blocks is smaller than the correlation length. Beckie [1996] used a spatial filtering approach, implemented by analytical and numerical calculations, to compare the effects of measurement scale and sampling scale on the estimation of general model parameters. He defined a "subgrid scale" lying above the measurement scale

and below the sampling scale, that is unresolved by a measurement campaign, leading to the so-called "closure problem" and consequent model errors. He concluded that minimization of subgrid variability can be achieved by increasing the measurement scale (at the cost of lower model resolution) or decreasing the sampling scale (at the cost of increasing the number of measurements that must be made).

CHAPTER 2

METHODS

2.1 The Real World

The numerical experiments that are the subject of this work are intended to parallel the laboratory experiments done by Tidwell and Wilson using the multi-support permeameter (MSP) [Tidwell and Wilson, 1997; Tidwell and Wilson, 1999a; Tidwell and Wilson, 1999b; Tidwell et al., 1999; Tidwell and Wilson, 2000]. The MSP is designed to meet the criteria described by Tidwell and Wilson:

[M]easurements made at different sample supports must be consistent in four basic ways. First, multisupport permeability data must be collected from the same physical sample, thus requiring the measurement technique to be nondestructive. Second, near exhaustive sampling is required at each support to avoid errors induced by sparse data effects. For this reason, large suites of data must be collected at each sample support, requiring measurements to be rapid and inexpensive. Third, measurements must be sensitive to slight changes in permeability at all sample supports; thus measurement error must be small and consistent. Fourth, measurements must be consistent in terms of flow geometry, boundary conditions, and

calculational techniques so as to provide a uniform basis for comparison. [Tidwell and Wilson, 1997]

The MSP consists of a gas minipermeameter coupled with a computer-controlled x-y positioner. Measurements are made by compressing the tip-seal against the flat face of the rock sample while injecting gas at constant pressure. Permeability is obtained using Eq. (1.1). Gas slippage effects were minimized by working at pressures at which they are insignificant. The user specifies a sampling grid that is programmed into the x-y positioner, which positions the tip-seal and compresses it against the rock face at a constant pressure [Tidwell and Wilson, 1997]. Rock samples are meter-scale cubical blocks. In order to assure consistent boundary conditions, the outermost points of the measurement grid are located sufficiently far from the edges of the sample to limit escape of gas from the sides of the block to negligible amounts.

The unique feature of the MSP is its use of different sized tip-seals, which can readily be exchanged, permitting data to be acquired over a range of discrete sample supports in a consistent manner [Tidwell and Wilson, 1997]. The tip-seals employed have inner radii of 0.15 cm, 0.31 cm, 0.63 cm, 1.27 cm and 2.54 cm and an outer radii measuring twice the inner. This arrangement preserves the flow geometry and boundary conditions of each measurement. The inner radius serves as the characteristic length scale of the instrument. Each doubling of the inner radius brings about an increase of the sample volume support by a factor of eight.

We modeled the gas minipermeameter assuming steady-state, isothermal flow of an ideal gas in a semi-infinite domain. Although the radial symme-

try of the instrument begs treatment using either cylindrical-polar or spherical-polar coordinates, we have chosen to operate in three-dimensional Cartesian coordinates, for reasons that we will explain in the next section. Neglecting gas slippage effects, the mass conservation equation is

$$\nabla \cdot (k \frac{\rho}{\mu} \nabla p) = 0,$$ (2.1)

with boundary conditions

$$\begin{cases} p = p_i, & (x - x_c)^2 + (y - y_c)^2 \leq a, \, z = 0, \\ \frac{\partial p}{\partial z} = 0, & a < (x - x_c)^2 + (y - y_c)^2 \leq b, \, z = 0, \\ p = p_o, & (x - x_c)^2 + (y - y_c)^2 > b, \, z = 0, \end{cases}$$ (2.2)
$$x, y \in (-\infty, +\infty), \, z \in [0, +\infty),$$

where ρ is the gas density, p is the gas pressure, x_c and y_c are the x and y coordinates, respectively, of the tip-seal center, and the other symbols are as defined previously. Substituting the ideal gas law, $pV = nRT$, into 2.1, we obtain

$$\nabla \cdot (k \frac{Mp}{\mu RT} \nabla p) = 0,$$ (2.3)

where M is the gas molecular mass, R is the gas constant, and T is absolute temperature.

Following from Goggin et al. [1988], we may use the Kirchhoff transform to linearize Eq. (2.3) in terms of p^2:

$$\nabla \cdot (k \frac{M}{2\mu RT} \nabla p^2) = 0$$ (2.4)

Viscosity is a function of both pressure and temperature. However, viscosity varies little with pressure, and the gas is isothermal, so viscosity is treated as constant in this work.

We may simplify the notation by introducing the pseudo-potential Φ, defined

$$\Phi = \frac{M}{2\mu RT} p^2. \tag{2.5}$$

Combining Eq. (2.1), Eq. (2.4), and Eq. (2.5) yields

$$\nabla \cdot k \nabla \Phi = 0 \tag{2.6}$$

$$\begin{cases} \Phi = \Phi_i, & (x - x_c)^2 + (y - y_c)^2 \leq a, \ z = 0, \\ \frac{\partial \Phi}{\partial z} = 0, & a < (x - x_c)^2 + (y - y_c)^2 \leq b, \ z = 0, \\ \Phi = \Phi_o, & (x - x_c)^2 + (y - y_c)^2 > b, \ z = 0, \end{cases} \tag{2.7}$$

$$x, y \in (-\infty, +\infty), \ z \in [0, +\infty).$$

In general, k is a tensor quantity, but we make the simplifying assumption of treating k as a scalar. Eq. (2.6) is the governing equation of the numerical minipermeameter system.

We may now write Eq. (1.1) in terms of the variables introduced in this section. Substituting Eq. (2.5) into Eq. (1.1), we obtain

$$k_{eff} = Q \frac{\left(\frac{p_i M}{RT} \right)}{aG_0(\Phi_i - \Phi_o)}, \tag{2.8}$$

where p_i is the gas pressure at the inlet. From the ideal gas law, we know that $\rho = pM/Rt$, so

$$k_{\mathit{eff}} = \frac{Q\rho_i}{aG_0(\Phi_i - \Phi_o)} \tag{2.9}$$

The quantity $Q\rho_i$ is just the mass flow rate into the sample, $\dot{m}_i$, leading us to

$$k_{\mathit{eff}} = \frac{\dot{m}_i}{aG_0(\Phi_i - \Phi_o)} \tag{2.10}$$

Eq. (2.10) is used to calculate the permeability k_{eff}. We also use Eq. (2.10) for model calibration, by prescribing k and solving for G_0.

Of course, we must also know $\dot{m}_i$ in order to apply Eq. (2.10). This we obtain by integrating the mass flux, $\mathbf{q}_m$ over the inlet area A_i. In our case, A_i lies in the plane $z = 0$, so

$$\dot{m}_i = \int_{A_i} \mathbf{q}_m \cdot \hat{\mathbf{e}}_z \, dx \, dy, \tag{2.11}$$

where $\hat{\mathbf{e}}_z$ is the unit vector normal to A_i. The mass flux is given by

$$\mathbf{q}_m = -k\frac{\rho}{\mu}\nabla p. \tag{2.12}$$

But note that

$$\begin{aligned} \nabla\Phi &= \nabla(\frac{M}{2\mu RT}p^2), \\ &= \frac{pM}{\mu RT}\nabla p, \\ &= \frac{\rho}{\mu}\nabla p. \end{aligned} \tag{2.13}$$

Substituting Eq. (2.13) into Eq. (2.12) yields

$$\mathbf{q}_m = -k\nabla\Phi, \qquad (2.14)$$

so

$$\dot{m}_i = \int\limits_{A_i} -k\nabla\Phi \cdot \hat{\mathbf{e}}_z \, \mathrm{d}x \, \mathrm{d}y. \qquad (2.15)$$

Eq. (2.10) becomes

$$k_{eff} = \frac{\int\limits_{A_i} -k\nabla\Phi \cdot \hat{\mathbf{e}}_z \, \mathrm{d}x \, \mathrm{d}y}{aG_0(\Phi_i - \Phi_o)}. \qquad (2.16)$$

We introduce here a system of non-dimensional quantities:

$$x_d \equiv \frac{x}{a}, \qquad (2.17)$$

$$y_d \equiv \frac{y}{a}, \qquad (2.18)$$

$$z_d \equiv \frac{z}{a}, \qquad (2.19)$$

$$b_d \equiv \frac{b}{a}, \qquad (2.20)$$

$$\nabla_d \equiv \frac{\partial}{\partial x_d}\hat{\mathbf{e}}_x + \frac{\partial}{\partial y_d}\hat{\mathbf{e}}_y + \frac{\partial}{\partial z_d}\hat{\mathbf{e}}_z, \qquad (2.21)$$

$$\Phi_d \equiv \frac{\Phi - \Phi_o}{\Phi_i - \Phi_o}, \qquad (2.22)$$

$$k_d \equiv \frac{k}{k_0}, \qquad (2.23)$$

where $\hat{\mathbf{e}}_x$, $\hat{\mathbf{e}}_y$, and $\hat{\mathbf{e}}_z$ are unit vectors oriented in the subscripted directions, and k_0 is an arbitrary reference permeability. Eq. (2.18) – Eq. (2.23) allow us to define a dimensionless mass flow rate from Eq. (2.15),

$$\dot{m}_d = \int\limits_{A_i} -k_d \nabla_d \Phi_d \cdot \hat{\mathbf{e}}_z \, \mathrm{d}x_d \, \mathrm{d}y_d, \tag{2.24}$$

which in turn yields an equation for the dimensionless effective permeability based on Eq. (2.16),

$$k_{eff,d} = \frac{1}{G_0} \int\limits_{A_i} -k_d \nabla_d \Phi_d \cdot \hat{\mathbf{e}}_z \, \mathrm{d}x_d \, \mathrm{d}y_d, \tag{2.25}$$

The minipermeameter governing equation , Eq. (2.6), and its boundary conditions, Eq. (2.7), can be recast

$$\nabla_d \cdot k_d \nabla_d \Phi_d = 0 \tag{2.26}$$

$$\begin{cases} \Phi_d = 1, & (x - x_c)^2 + (y - y_c)^2 \leq 1,\ z_d = 0, \\ \frac{\partial \Phi_d}{\partial z_d} = 0, & 1 < (x - x_c)^2 + (y - y_c)^2 \leq b_d,\ z_d = 0, \\ \Phi_d = 0, & (x - x_c)^2 + (y - y_c)^2 > b_d,\ z_d = 0, \end{cases} \tag{2.27}$$

$$x_d, y_d \in (-\infty, +\infty),\ z_d \in [0, +\infty).$$

The stage is set. We numerically solve Eq. (2.26) subject to the boundary conditions (2.27) with k_d given by a stochastically simulated permeability field. The effective permeability is calculated by solving Eq. (2.25), also numerically. We discuss the numerical model and the simulation procedure in the following sections.

2.2   The Model

We model the system using a block-centered finite-difference scheme, working in three-dimensional Cartesian coordinates. The numerical scheme is

described in detail in Appendix A. Though the annular boundary conditions imposed by the instrument invites treatment in a curvilinear coordinate system, we elect to work in Cartesian coordinates because we are addressing a problem of upscaling. In a numerical treatment, use of cylindrical or spherical coordinates results in grid-blocks whose volume is scaled by the radial distance from the origin of the coordinate system. Permeability values assigned to these blocks would have to be based on an upscaling rule. This would prove especially challenging for comparing measurements made with different tip-seals: the size of grid-blocks contributing most heavily to the measurement, those located directly beneath the edges of the tip-seal, would be scaled by the size of the tip-seal itself. It would be very difficult to disentangle the effect of the changing boundary condition from actual upscaling behavior.

While it becomes necessary later on to assume an upscaling rule when simulating the log permeability, as discussed in §2.3, we elect to use the Cartesian coordinate system, which permits grid-blocks to be of a uniform size throughout the domain.

2.2.1 Boundary Conditions

We now describe the numerical boundary conditions we use to replicate the operation of the instrument on a sample. Recall that the boundary conditions of the minipermeameter are given by Eq. (2.26). The boundary conditions pose two immediate problems. First, we must find a way to assemble circular boundaries from square grid-blocks. Second, we must replicate an infinite domain using a finite number of grid-blocks.
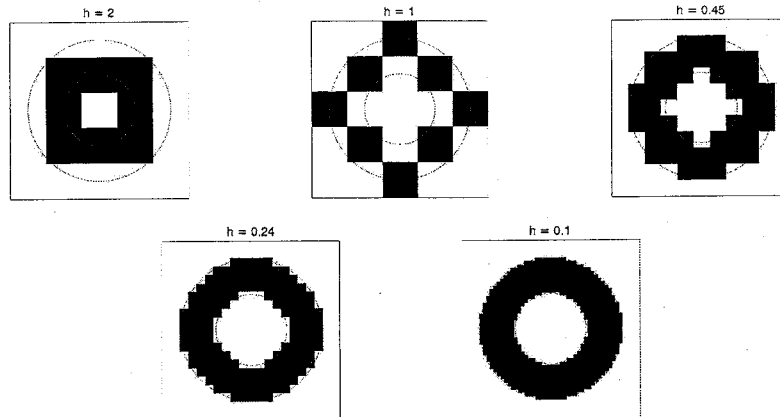
Figure 2.1: Discretized boundary conditions

In addressing the first of these problems, we reasoned that we might approximate the circular tip-seal by using many small grid-blocks. Projecting the concentric circular profile onto the nominal top surface of the domain, on which the tip-seal boundary condition is applied, we designate grid-blocks whose centroid falls on or within the inner circle to lie inside the tip-seal, blocks whose centroid lies between the circles we designate to lie under the tip-seal, and blocks whose centroid lies outside the outer circle we designate to lie outside the tip-seal, as illustrated in Fig. (2.1), which shows the discretization as a function of the dimensionless grid separation h_d (recall $h_d = \frac{h}{a}$). In the figure, the concentric circles represent the edges of the tip seal and the black squares represent grid-blocks assigned a no flow boundary. grid-blocks on the top surface are chopped (see Appendix A); all other boundaries are full blocks. Note that the approximation becomes better as h becomes smaller. However, it is clear that the area inscribed by the circular approximation will always be greater than that of the true circle. Hence, we define the effective radius, r_{eff},

of a circular approximation as the radius of a circle with the same area as the approximation, A_{circ},

$$r_{eff} = \sqrt{\frac{A_{circ}}{\pi}} \tag{2.28}$$

The effective inner and out radii are defined

$$a_{eff} \equiv \sqrt{\frac{A_i}{\pi}} \tag{2.29}$$

$$b_{eff} \equiv \sqrt{\frac{A_o}{\pi}} \tag{2.30}$$

We use effective radii to define the instrument geometry, so the non-dimensional outer radius is calculated

$$b_{d,eff} = \frac{b_{eff}}{a_{eff}} \tag{2.31}$$

Effective radii are used as a metric to determine the physical analogue to the discretized boundary conditions. For example, the nominal inner and outer radii of the discretization shown as "h=1" in Fig. (2.1) are 1.00 and 1.97, respectively. However, the effective inner and outer radii are 0.985 and 1.968, respectively, yielding $b_{d,eff} = 1.9975$. This, in fact, is the discretization used for the model. In addition, the effective radius is used in the calculation of the effective permeability from Eq. (2.16), in which a_{eff} is substituted for a in the denominator.

We address the second problem by using a domain sufficiently large that the influence of the boundary conditions at the sides and bottom of the domain is negligibly small. The farther the edges of the synthetic sample lie from the central axis of the synthetic sample support (along which the measurement is made), the better the approximation to an infinite domain.

It is evident that the demands of our two approximations act at cross purposes. Good approximation of the annular boundary conditions at the tip-seal requires that grid blocks be very small relative to the tip-seal itself. Good approximation of an infinite half space requires that either grid-blocks be numerous and/or large in size. With limited computational resources at our disposal, in the sense that we are limited in the number of grid-blocks we may use in our simulation, we must contend with the fact that excellence of one approximation may be purchased at the price of mediocrity of the other. We describe now our attempts to optimize the configuration of the domain.

We use the geometric factor, G_0, as our primary metric for evaluating the suitability of various configurations of the domain. Prescribing a uniform permeability $k_d = 1$, we calculate geometric factors by rearranging Eq. (2.25)

$$G_0 = \int_{A_i} -\nabla_d \Phi_d \cdot \hat{\mathbf{e}}_z \, \mathrm{d}x_d \, \mathrm{d}y_d, \qquad (2.32)$$

For numerical reasons, we can more accurately calculate the mass flux into the rock by using the surface defined by the sides and bottom of the grid-blocks lying adjacent to the inlet of the instrument (i. e., the layer of grid-blocks we designated "in" when prescribing the boundary conditions) than we can by using the top surface of those blocks. This is easily done using the same approach shown in Eq. (A.5) (see Appendix A). For the N_{in} blocks lying inside the tip-seal,

$$\int_{A_i} -\nabla_d \Phi_d \cdot \hat{\mathbf{e}}_z \, dx_d \, dy_d \approx$$

$$\sum_{n=1}^{N_{in}} -\nabla_d \Phi_d \cdot \hat{\mathbf{e}}_z h_x h_y \approx$$

$$\sum_{n=1}^{N_{in}} \left[\left(\frac{\Phi_{d,n} - \Phi_{d,n-1}}{h_x} h_y h_z \right) - \left(\frac{\Phi_{d,n+1} - \Phi_{d,n}}{h_x} h_y h_z \right) \right.$$
$$+ \left(\frac{\Phi_{d,n} - \Phi_{d,n-N_x}}{h_y} h_x h_z \right) - \left(\frac{\Phi_{d,n+N_x} - \Phi_{d,n}}{h_y} h_x h_z \right)$$
$$\left. + \left(\frac{\Phi_{d,n} - \Phi_{d,n-N_x N_y}}{h_z} h_x h_y \right) \right] \tag{2.33}$$

We begin by testing the effect of the dimensionless grid separation h_d on the numerically calculated geometric factor $\widetilde{G}$. Our test domain is a homogeneous, isotropic, cubical region measuring 10 dimensionless length units on a side and with dimensionless permeability $k_d = 1$. We denote the theoretical geometric factor that obtains for this scenario $G(10)$ and the numerically calculated geometric factor $\widetilde{G}(10)$. We set the nominal dimensionless inner and outer radii of the simulated permeameter $a = 1$ and $b = 2$, though the actual effective radii vary as a function of h_d. The purpose of this test is to compare $\widetilde{G}(10)$ to the geometric factor for the physical analogue to this system $G(10)$. If the discretization scheme is valid, we should see $\widetilde{G}(10)$ approach $G(10)$ as $h_d \to 0$. While we don't know exactly what value $G(10)$ takes, we can estimate it. The numerical work done by Goggin et al. [1988] and Chen [1992] and laboratory work done by Suboor and Heller [1995] suggest that $G(10)$ for this finite domain should differ from the analytical solution for a semi-infinite domain, $G_0 = 5.099$, by less than 1%. Thus, we expect that $G(10) = 5.099 \pm 0.051$.
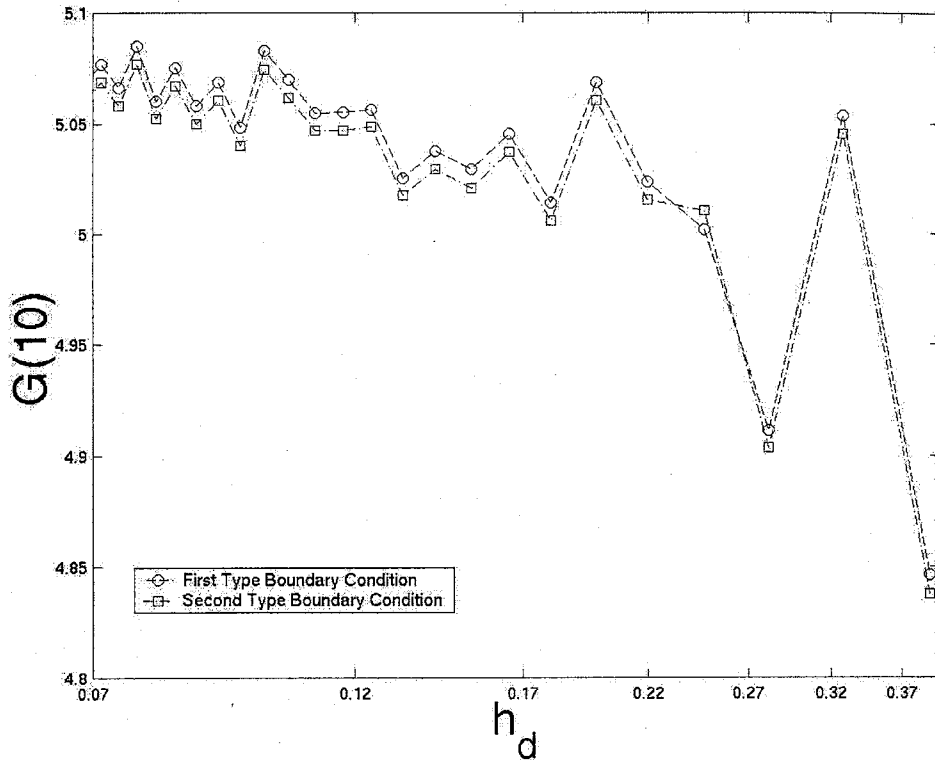
Figure 2.2: Geometric factors for numerical minipermeameters as a function of dimensionless grid separation

Further, based on work by Chen [1992], $G(10)$ will lie between the geometric factor derived from a simulation in which the sides and bottom of the domain (which we refer to as the "far" boundaries from here on) are given a no-flow boundary condition, $\widetilde{G}_{nf}(10)$, and that for a simulation in which those boundaries are prescribed a side-of-grid-block constant potential $\Phi = 0$, $\widetilde{G}_p(10)$. We plot curves of $\widetilde{G}(10)$ in Fig. (2.2). Analysis is complicated by the fact that the $b_{d,eff}$ varies as we change h_d (Table (2.1)), accounting for the jaggedness of the
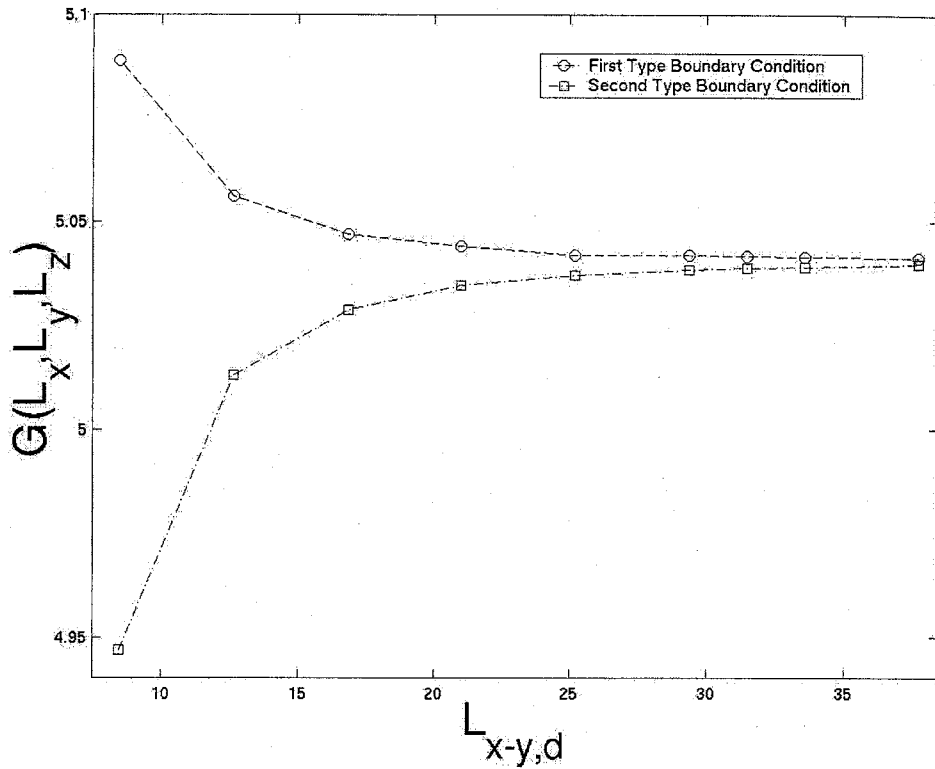
Figure 2.3: Geometric factors for numerical minipermeameters as a function of domain size

curves. Nonetheless, we do see convergence to a value in the expected range— for $h = 0.0687$, $\widetilde{G}_{nf}(10) = 5.0597$ and $\widetilde{G}_{p}(10) = 5.0675$, the values differing by less than two parts in a thousand. This confirms that the discretization scheme is valid.

Next, we test the location of the far boundaries. Setting $h_d = 0.1$, we generate a series of homogeneous, isotropic sample domains ranging in size from $5.1 \times 5.1 \times 2.5$ dimensionless length units to $36.1 \times 36.1 \times 18.1$ dimension-

h_d	a	b	b_d
0.3922	1.0139	2.0873	2.0587
0.3279	0.9962	2.0348	2.0426
0.2817	0.9667	2.0166	2.0860
0.2469	0.9751	2.0331	2.0849
0.2198	1.0300	2.0032	1.9449
0.1980	1.0055	2.0141	2.0031
0.1802	1.0012	1.9946	1.9922
0.1653	0.9913	2.0109	2.0109
0.1527	1.0082	2.0109	1.9945
0.1418	0.9768	1.9943	2.0415
0.1324	0.9942	2.0010	2.0127
0.1242	0.9837	1.9885	2.0215
0.1170	1.0072	2.0069	1.9925
0.1105	0.9916	2.0037	2.0206
0.1047	1.0112	1.9921	1.9699
0.0995	1.0121	2.0030	1.9791
0.0948	0.9991	2.0045	2.0064
0.0905	1.0018	2.0043	2.0006
0.0866	1.0023	2.0051	2.0006
0.0830	1.0009	2.0024	2.0006
0.0797	1.0022	2.0069	2.0025
0.0766	1.0093	2.0023	1.9839
0.0738	1.0002	2.0025	2.0022
0.0712	1.0007	1.9985	1.9972
0.0687	0.9999	2.0003	2.0004

Table 2.1: Effective dimensionless radii for fig. (2.2)

less length units, where $a = 1$ and $b = 2$. We calculate the numerical geometric factor as a function of domain size, $\widetilde{G}(L_x, L_y, L_z)$, for both no-flow and constant potential far boundary conditions. The objective here is to test the sensitivity of the measurement to conditions at the far boundaries. This gives us a guideline as to how far we must set the far boundaries from the measurement location in order to claim that we are simulating an infinite domain (or, put another way, defines the effective sample support for the numerical minipermeameter). In addition, we obtain the value of the geometric factor $\widetilde{G}_0$ for our numerical minipermeameter sampling a "semi-infinite" domain, when $h_d = 0.1$, $a = 0.9853$, $b = 1.9682$, and $b_d = 1.9975$. We plot curves of $\widetilde{G}(L_x, L_y, L_z)$ in Fig. (2.3). Based on the largest simulation domain, $\widetilde{G}_0$ is 5.040 ± 0.002. The relative difference between outcomes of the two far boundary conditions drops below 0.1% by the point the domain is $25.1 \times 25.1 \times 12.5$ length units.

Based on these tests, we have chosen to use a $25.1 \times 25.1 \times 12.5$ synthetic sample domain with a grid separation $h_d = 0.1$ for the experiments described below. For this discretization, $\widetilde{G}_0 = 5.05358$, $a_{eff} = 0.985$, $b_{eff} = 1.968$, and $b_{d,eff} = 1.9975$. The effective inner radius a_{eff} and numerical geometric factor $\widetilde{G}_0 = 5.05358$ are used to calculate the effective permeability from Eq. (2.16).

2.2.2 Numerical Experimental Design

The underlying log permeability field of the laboratory sample is characterized by a nested semivariogram with a maximum correlation length of 13.0 dimensionless length units. Tidwell and Wilson [1997] used a 50×50 measurement grid, with measurement points separated by 0.5 dimensionless length

units. Unfortunately, computational limitations forbid making an equivalent number of numerical measurements. Instead, we make measurements at 100 locations on a single transect, with measurements separated by 0.5 length units. This scheme allows us to sample a statistically significant number of points in a single direction at the cost of limiting our numerical estimate of the spatial structure to the transect direction. The longest correlation length of the synthetic log permeability parallel to the transect is 7.09 dimensionless length units.

The dimensions of the flow domain in the numerical experiment are constant relative to the tip-seal: the length and breadth of the flow domain are always 25.1 times the inner tip-seal radius and the depth of the flow domain is always 12.5 times the inner tip seal radius. At this point, we introduce some notation. Henceforth, the model 2.54 cm tip-seal and the log permeability field associated with it are denoted by either an "x1" or subscript "1". The 1.27 cm, 0.63 cm, 0.31 cm, and 0.'5 cm tip-seals and fields are denoted by "x2", "x4", "x8", and "x16", respectively, or the subscripts "2", "4", "8", and "16", respectively. The correlation lengths of the log permeability field remain fixed, and thus are not constant relative to either the tip-seal or the flow domain. For example, the correlation length perpendicular to bedding of the large-scale exponential semivariogram structure is 7.09 times the inner radius of the x1 tip-seal (i. e., the model 2.54 cm tip-seal). The flow domain used to test the x2 tip-seal is 25.1 times the inner tip-seal radius, but now the correlation length perpendicular to bedding of the large scale exponential semivariogram is 14.18 times the x2 inner tip-seal radius. We discuss the details of how we create the log permeability fields used in the numerical experiment in the following

section.

2.2.3 Geostatistical Simulation of Synthetic Permeability

Ideally, the geostatistical simulation procedure should replicate, at least in the statistical sense, the point-scale permeability of the laboratory rock samples. Given such a simulation procedure, we would then calculate effective permeability on a gridded set of locations with the numerical minipermeameter, using different sizes of tip-seal at each point on the grid. This ideal approach is impractical for several reasons. First, we have no way of knowing the true point-scale log permeability of the rock samples. Second, even if we did know (or assumed) the point-scale permeability, a synthetic sample simulated with the necessary resolution would consist of on order of 10^{10} grid-blocks, exceeding what we can handle with the available computational resources by four orders of magnitude. Third, even if we had the resources to synthesize and test such a field, we are unable to replicate the different tip-seal sizes in a consistent fashion.

Our solution is to assume the statistics calculated from the set of laboratory measurements obtained with the smallest tip-seal is representative of the true point-scale permeability. This assumption provides a testable hypothesis, viz., "How well do the measurements made at the smallest support capture the underlying permeability field?" Using those statistics and the measurements from which they are calculated, we conditionally synthesize a log permeability field using sequential Gaussian simulation [Deutsch and Journel, 1998] and measure its effective permeability. Our choice of coordinate system, however, presents us with a dilemma. As we are unable to synthesize a single permeabil-

ity field and subject it to a consistent set of tests corresponding to interrogation by different sizes of tip-seal, we must choose between maintaining consistent boundary conditions while changing the permeability, or maintaining a consistent permeability while changing boundary conditions. We have chosen the former. The objective is to formulate a procedure by which we synthesize a three-dimensional log permeability field of sufficient breadth and depth that a measurement made at the center of the top surface is unaffected by conditions at the sides and bottom (so that, as far as the instrument knows, it is measuring a sample of infinite breadth and depth) and of sufficient length that we may move the instrument along this direction, making measurements at regular intervals. We will call this large- scale field the "superblock". The superblock is the field that is tested by the largest tip-seal. In order to subject this field to measurement by successively smaller tip-seals, we require a means of "magnifying" the superblock, i. e., increasing resolution relative to the fixed boundary conditions imposed by the instrument. In the laboratory, the tip-seals decrease in size by a factor of two with each step, so in the numerical experiment the resolution of the synthetic log permeability field increases by a factor of two in all directions with each step. Rather than use successively smaller tip-seals for the numerical experiment, as was done in the laboratory, the dimensions of the flow domain are halved and the grid resolution doubled with each magnification. As discussed in the previous section, the trick is to do this in such a way that each magnification of the log permeability field behaves as much as possible like halving the size of the tip-seal. We attempt this by requiring that the statistical properties of the field should be invariant in the procedure of magnification, or, at least, that the changes it undergoes should be physically

sensible. We devised a two-step procedure of simulation and interpolation to accomplish this.

In overview, we initially create a coarse-grid geostatistical simulation of the superblock, modeled to bear a statistical likeness to the small tip-seal data set. This is the permeability seen by the largest of the numerical tip-seals. We measure the permeability at the first station on the transect by discarding all the simulated log permeability values lying outside a $251 \times 251 \times 125$ node region (as defined at the end of §2.2.2) centered on that station. The truncated "local" field is used in the numerical flow calculation. Remaining at this point on the transect, we magnify the local field by a factor of two by inserting new node points between the previously simulated ones and then conditionally simulate log permeability values on the new nodes. We are unable to simulate the entire magnified field, containing as it does eight times the number of grid points as the original, so we truncate the outside edges and bottom half of the original field. Recall that the tip-seal applied to the magnified field is half the size of that for the original, so the truncation only removes information to which the instrument is relatively insensitive. We magnify and simulate the local field four times, to provide more detailed grids for measurements made with successively smaller tip-seals. Once we have completed the full suite of measurements at a given point, we move to the next station on the transect, repeating the procedure of simulation and magnification. We discuss the procedure in detail next.

We used sequential Gaussian simulation to generate log permeability values on the nodes. Sequential Gaussian simulation has the property of hon-

oring global statistics of the simulated random function, which was the critical objective of the simulation routine. In addition, sequential Gaussian simulation is very fast compared to other routines such as Turning Bands, which is vital considering that the numerical experiment requires simulation of five hundred realizations. Geostatistical simulation routines like sequential Gaussian simulation differ from estimators like Kriging in that the former are designed to maximize local accuracy without regard to global fidelity. However, sequential Gaussian simulation is built on the foundation of Kriging, so we will discuss Kriging before discussing simulation.

All versions of Kriging are elaborations on the basic linear regression estimator:

$$\left[Z^*_{Krig}(\mathbf{x}) - m(\mathbf{x})\right] = \sum_{i=1}^{n} \lambda_i \left[Z(\mathbf{x}_i) - m(\mathbf{x}_i)\right] \tag{2.34}$$

where $Z(\mathbf{x}_i)$ is the random variable model at location $\mathbf{x}_i$, $\mathbf{x}_i$ is the location of the ith data value and $m(\mathbf{x})$ is the attribute mean in the neighborhood of $\mathbf{x}$; $Z^*_{Krig}(\mathbf{x})$ is the estimated random variable at some other location to be estimated, $\mathbf{x}$ [Deutch and Journel,1998]. Kriging has the property of being the best linear unbiased estimator. The estimate is best in the sense that the mean of the estimation errors m_r is set to 0 and unbiased in the sense that the error variance s_r^2 is minimized. The weights are calculated to optimize m_r and s_r^2 by solving the equation

$$\sum_{j=1}^{n} \lambda_j C(\mathbf{x}_j - \mathbf{x}_i) = C(\mathbf{x} - \mathbf{x}_i), \tag{2.35}$$

where $C(\mathbf{x}_j - \mathbf{x}_i)$ is the model covariance between attribute values at $\mathbf{x}_j$ and $\mathbf{x}_i$ and $C(\mathbf{x} - \mathbf{x}_i)$ is the covariance between the location of the point to be

estimated, $\mathbf{x}$, and $\mathbf{x}_i$. Note that we must have prior knowledge of the covariance model in order to make the estimate. The estimation variance is:

$$s^2_{Krig} = C(0) - \sum_{i=1}^{n} \lambda_i C(\mathbf{x} - \mathbf{x}_i). \qquad (2.36)$$

In sequential Gaussian simulation, we begin by performing a normal score transformation on the data and then fitting a semivariogram model to the transformed data. We then work out a random path through the locations we wish to simulate. At each point, we calculate the Kriged estimate and variance, conditioning on both the original data and simulated values. The simulated value at that point is a number drawn at random from a normal distribution that has a mean equal to the Kriged estimate and a variance equal to the Kriged variance. Obtaining such a distribution is simply a matter of scaling a zero-mean, unit-variance normal distribution by s_{Krig} and adding z^*_{Krig}. If there are no nearby data for Kriging or if we are performing an unconditional simulation, then the global mean and variance are used–the simulated value is simply a random number drawn from a zero-mean, unit variance normal distribution. Once the simulation is complete, we back transform the data to the original distribution, taking care to avoid introducing bias [Deutch and Journel, 1998]. In our case, we assume that the permeability is lognormally distributed, so we need not apply a normal score back-transform. We do, of course, exponentiate $\ln(k)$ before the fluid-flow simulation using the methods of §2.2.1.

The initial synthetic log permeability field, $\ln(k_1(\mathbf{x}_0))$, corresponds to a subregion of the rock sample interrogated by the largest tip-seal. The permeability field used for the fluid flow simulation is the exponentiation of the log permeability, $k_1(\mathbf{x}_0)$. As discussed in the previous section, we need not

necessarily simulate the entire rock sample for any single test, only the effective sample support, the box-shaped subregion, with a length and width of 25.1 dimensionless units and a depth of 12.5 dimensionless units. We set $b_{d,eff} = 1.998$, as close as possible to 2, and $h_d = 0.1$. The effective permeability calculated from the measurement of $k_1(\mathbf{x}_0)$ is $k_{eff,1}(12.55, 12.55, 0)$ (the coordinates are of the tip-seal center). Next, we change tip-seals, switching to the next smallest instrument. In order to maintain consistency of the boundary conditions, we retain the same domain and instrument parameters, but we change the look of the permeability field. Imagine that rather than shrinking the instrument with respect to a fixed permeability field, we magnify the permeability field with respect to a fixed instrument (or, more accurately, with respect to a fixed set of boundary conditions that defines the instrument). It works like this: We discard the points from $k_1(\mathbf{x}_0)$ that lie outside the sample support of the new, smaller tip-seal. If the initial simulation consists of $251 \times 251 \times 251$ grid points, we keep the central 125×125 grid points lying in a horizontal slab that extends 61 grid points from the top surface. The grid points of the previous simulation are co-located with the grid points of the new simulation. However, the absolute grid separation of the new domain is half that of the previous domain, so there are now rows, columns and layers of new grid points that lie between those of the previous domain. We assign the punctual permeability values from $k_1(\mathbf{x}_0)$ to their collocated grid blocks in the new domain and then obtain permeability values for the remaining vacant grid-blocks with conditional sequential Gaussian simulation. Call the new field $k_2(\mathbf{x}_0)$. Note that in doing this, we have assumed an upscaling rule. The punctual values from $k_1(\mathbf{x}_0)$, originally assigned the relatively coarse grid-blocks of the initial simulation,
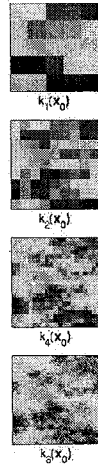
Figure 2.4: Magnified natural log permeability fields

are now passed to the finer grid-blocks of the current simulation. Basically, we have assumed that the spatial correlation structure exists across all scales, but that the model is indifferent to information that lies below the grid-block scale. This amounts to using the crudest of low-pass filters, simple sampling, for an upscaling rule. What consequences of this rule might we anticipate? Given that all the fields are sufficiently large as to ensure second order stationarity, simple sampling should guarantee that the sample statistics of the synthetic log permeability fields remain constant across all grid-block supports.

We run the magnification routine a total of four times, creating the conditional permeability fields $k_2(\mathbf{x}_0)$, $k_4(\mathbf{x}_0)$, $k_8(\mathbf{x}_0)$, $k_{16}(\mathbf{x}_0)$. The $k_1(\mathbf{x}_0)$, $k_2(\mathbf{x}_0)$, $k_4(\mathbf{x}_0)$, $k_8(\mathbf{x}_0)$, $k_{16}(\mathbf{x}_0)$ fields correspond to the permeability fields interrogated by the 2.54 cm, 1.27 cm, 0.63 cm, 0.31 cm and 0.15 cm tip-seals, re-

spectively. We illustrate this process for the $\ln(k_1(\mathbf{x}_0)) - \ln(k_8(\mathbf{x}_0))$ in Fig. (2.4) ($\ln(k_{16}(\mathbf{x}_0))$ is omitted for the sake of clarity). In this figure, we show a two-dimensional slice of the log permeability field as seen by each tip-seal. The length and breadth of the slice are both five global dimensionless units. The top image is from within $\ln(k_1(\mathbf{x}_0))$, consisting of five by five grid-blocks, is drawn form the initial unconditional simulation. The second image from the top is from the same portion of $\ln(k_2(\mathbf{x}_0))$ and consists of nine by nine grid blocks. Rows and columns of new blocks have been inserted between those from the initial simulation of this region. This can be seen by scanning along the top row of grid-blocks. The first, third, fifth, seventh and ninth grid-blocks of the $\ln(k_2(\mathbf{x}_0))$ field correspond to the first, second, third, fourth and fifth grid blocks of the $\ln(k_1(\mathbf{x}_0))$ field, respectively. The grid-block centers of these odd numbered blocks from $\ln(k_2(\mathbf{x}_0))$ share the same global coordinates with the corresponding grid-blocks from $\ln(k_1(\mathbf{x}_0))$, and so share the same value of log permeability. The inserted grid-blocks in the $\ln(k_2(\mathbf{x}_0))$ field are conditionally simulated on the information passed from the $\ln(k_1(\mathbf{x}_0))$ field. Similarly, the third image from the top, taken from the $\ln(k_4(\mathbf{x}_0))$ field, is made up of collocated log permeability values passed from the $\ln(k_2(\mathbf{x}_0))$ field and conditionally simulated log permeability values at the intervening grid-blocks. The bottom image form the $\ln(k_8(\mathbf{x}_0))$ field is generated the same way from the $\ln(k_4(\mathbf{x}_0))$ field above it. This algorithm ensures that information is preserved across all scales.

We now are ready to move the numerical instrument to a new position on the measurement grid. In this study, the grid is actually a transect, so we describe in detail only the routine for repositioning in a single direction. The

transect consists of 100 measurement points extending in the y direction, perpendicular to bedding. The measurement points are separated by 0.5 global dimensionless length units, equal to half the inner radius of the $x1$ tip-seal. The routine can easily be generalized to simulate measurements made on a two-dimensional or even three-dimensional grid. We now introduce a global, dimensionless Cartesian coordinate system with an origin at the lower, left corner of top layer of the initial simulation $k_1(\mathbf{x}_0)$, so the sample domain $\mathbf{x}_0$ is bounded on the outside by the planes $x_{global} = 0, x_{global} = 25.1, y_{global} = 0, y_{global} = 25.1, z_{global} = 0, z_{global} = 12.45$ with the center of the tip-seal positioned at $x_{global} = 12.55, y_{global} = 12.55, z_{global} = 0$. (recall that the top layer consists of chopped blocks). Distances in the global system, designated with a subscript "*global*", are always given in dimensionless units scaled by the inner radius of the largest tip-seal and referenced to the origin at the corner of $k_1(\mathbf{x}_0)$. By contrast, distances in local coordinates are scaled by the inner radius of the tip-seal in current use and are referenced to the lower, left corner of the top layer of the current domain.

Suppose now that we move the instrument 0.5 dimensionless units in the positive y direction. We designate the sample supports associated with the first shift $\mathbf{x}_1$. The sample support of the largest tip-seal is now bounded by the planes $x_{global} = 0, x_{global} = 25.1, y_{global} = 0.5, y_{global} = 25.6, z_{global} = 0, z_{global} = 12.45$. We obtain the shifted permeability field $k_1(\mathbf{x}_1)$ by discarding the points from $k_1(\mathbf{x}_0)$ that lie outside the boundaries of the shifted field (the lower five rows, consisting of grid-blocks from the initial realization $ix_0 = 1 \ldots 251, iy_0 = 1 \ldots 5, iz_0 = 1 \ldots 125$) and conditionally simulating the vacant points of the new simulation (the upper five rows, consisting of

$ix_1 = 1 \ldots 251, iy_1 = 247 \ldots 251, iz_1 = 1 \ldots 125$). The effective permeability calculated from measurement of $k_1(\mathbf{x}_1)$ is $k_{eff,1}(x_{global} = 12.55, y_{global} = 13.05, z_{global} = 0)$.

Moving on to the second largest tip-seal, the boundaries of the field $k_2(\mathbf{x}_0)$ are the planes $x_{global} = 6.275, x_{global} = 18.825, y_{global} = 6.275, y_{global} = 18.825, z_{global} = 0, z_{global} = 6.225$. The boundaries of the shifted field $k_2(\mathbf{x}_1)$ are the planes $x_{global} = 6.275, x_{global} = 18.825, y_{global} = 6.775, y_{global} = 19.325, z_{global} = 0, z_{global} = 6.225$. We retain all the points previously simulated from both $k_1(\mathbf{x}_0)$ and $k_2(\mathbf{x}_0)$ that lie within the boundaries of $k_2(\mathbf{x}_1)$, and conditionally simulate the remaining vacant grid points. Similarly, we pass all points from the simulations $k_1(\mathbf{x}_0)$, $k_2(\mathbf{x}_0)$, and $k_4(\mathbf{x}_0)$ lying within $x_{global} = 9.4125, x_{global} = 15.6875, y_{global} = 10.4125, y_{global} = 16.6875, z_{global} = 0, z_{global} = 3.1125$ to $k_4(\mathbf{x}_1)$. We repeat the procedure for $k_8(\mathbf{x}_1)$ and $k_{16}(\mathbf{x}_1)$. An image of the three-dimensional $x1$ superblock is shown in Fig. (2.5); similar images of the other superblocks are unavailable due to memory limitations. We show plan views of the superblock fields in Fig. (2.6) – Fig. (2.9), showing only k_1–k_8. The grid spacing of the k_{16} field is so dense that it is not possible to assemble an image due to memory limitations.

Consider the set of geostatistical simulations used here. The synthetic field is modeled on a set of MSP measurements with a 0.15 cm tip-seal on a 50×50 grid with grid centers separated by 1.27 cm (Fig. 2.10) [Tidwell and Wilson, 2000]. The image shows the natural logarithm of the measured permeability normalized by the mean of the set. Fig. (2.11) and Fig. (2.12) show the histogram and semivariograms, respectively, calculated from the data.
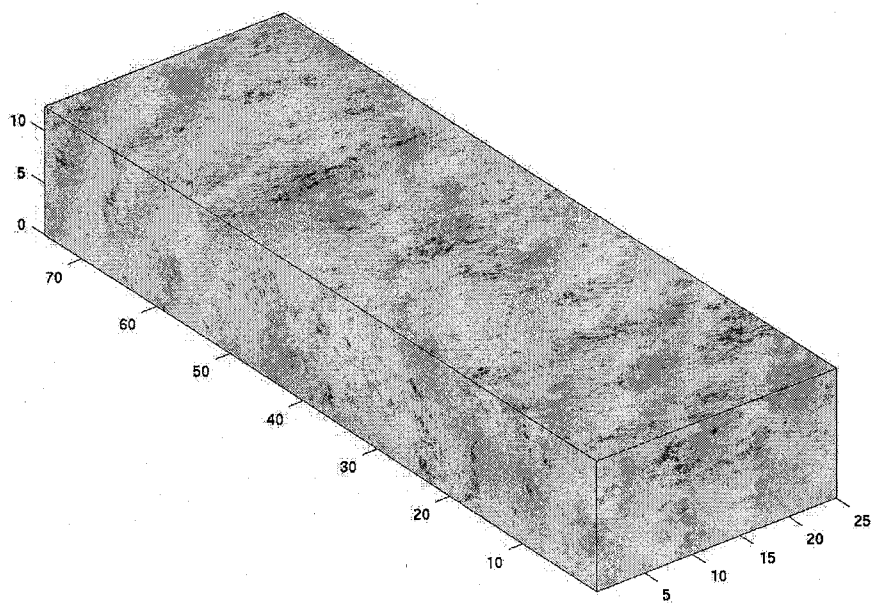
Figure 2.5: Synthetic permeability field, $\ln\left(k_1\right)$

k_1 (x,y,z = 0 cm)
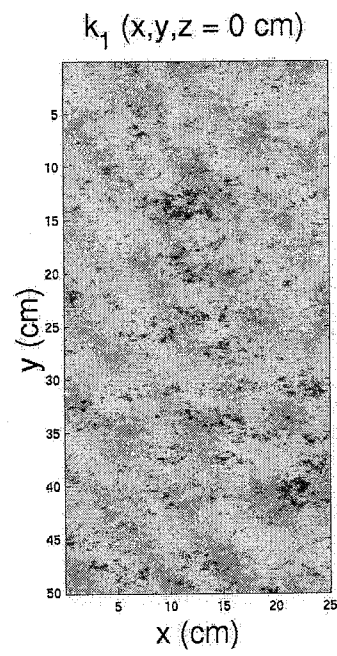
Figure 2.6: Plan view of $\ln(k_1)$ synthetic permeability field
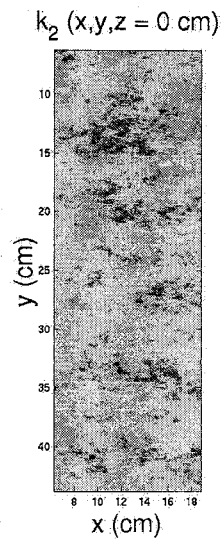
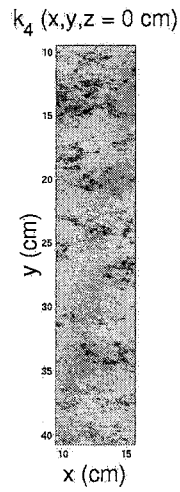Figure 2.7: Plan view of $\ln(k_2)$ synthetic permeability field

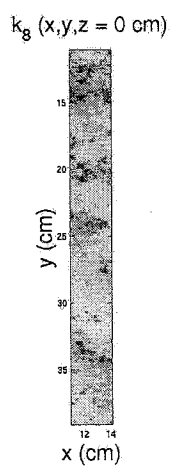Figure 2.8: Plan view of $\ln(k_4)$ synthetic permeability field

Figure 2.9: Plan view of $\ln(k_8)$ synthetic permeability field
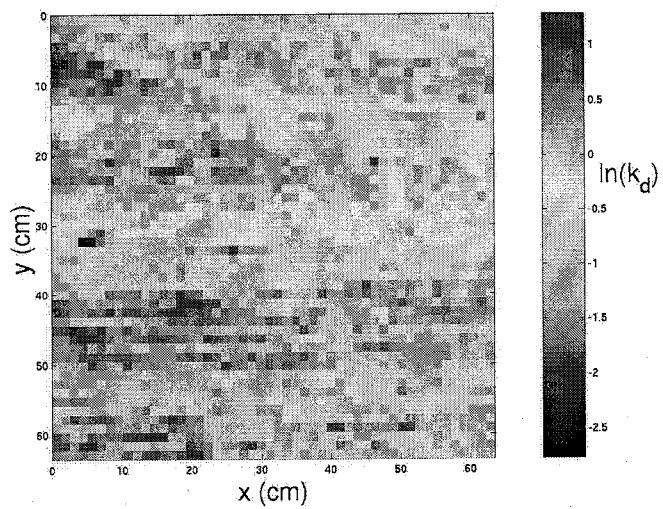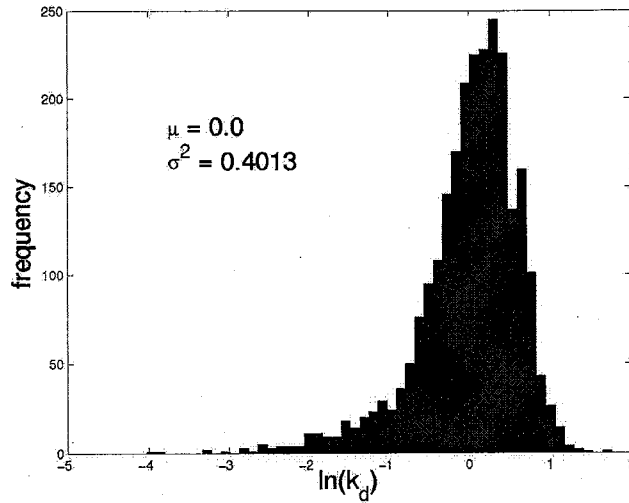

Figure 2.10: Massillon sandstone, $\ln k_d$

Figure 2.11: Massillon sandstone, histogram of $\ln k_d$ for $a = 0.15$cm

Tidwell and Wilson [2000] fit a nested, anisotropic semivariogram model to the sample semivariogram. We used their two-dimensional model as the basis for our three-dimensional model, assuming the Massillon to be isotropic in the xz direction, parallel to the bedding. The three-dimensional semivariogram model, shown as a solid line in Fig. (2.12), is

$$\gamma(\mathbf{s}_d) = s_1^2 \left(1 - \exp\left[-3\mathbf{s} \cdot \lambda_1'\right]\right) + s_2^2 \left(1 - \exp\left[-3\mathbf{s} \cdot \lambda_2'\right]\right) + s_3^2 \left(1 - \cos\left[-2\pi\mathbf{s} \cdot \lambda_3'\right]\right),$$
$$(2.37)$$

where s_j^2 is the variance component for the jth model ($j = 1, 2, 3$), λ_j' (not to be confused with the Kriging weight λ) is the reciprocal correlation length in the principal directions

$$\lambda_j' = \frac{1}{\lambda_{x,j}}\hat{\mathbf{e}}_x + \frac{1}{\lambda_{y,j}}\hat{\mathbf{e}}_y + \frac{1}{\lambda_{z,j}}\hat{\mathbf{e}}_z$$

for the jth model, in which $\lambda_{x,j}$ is the correlation length of the jth model in the
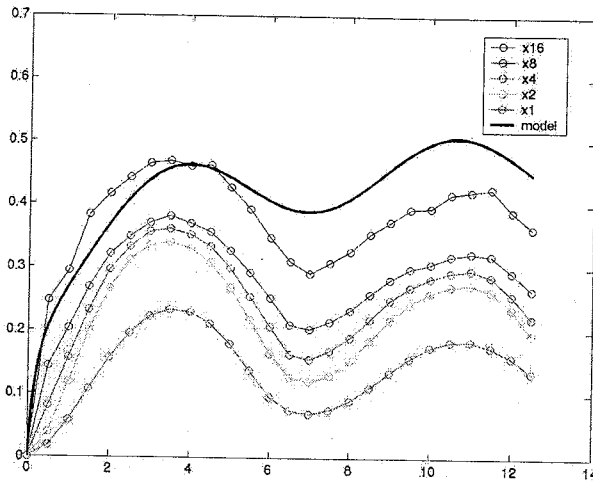
Figure 2.12: Massillon sandstone, semivariograms of $\ln k_d$

Model Index	s^2	λ_x	λ_y	λ_z
1	0.17	1.06	0.59	1.06
2	0.23	13.0	7.09	13.0
3	0.055	1×10^6	7.09	1×10^6

Table 2.2: Model $\ln (k)$ semivariogram parameters [Tidwell and Wilson, 2000]

x direction, and $\mathbf{s}_d = s_{d,x} \hat{\mathbf{e}}_x + s_{d,y} \hat{\mathbf{e}}_y + s_{d,z} \hat{\mathbf{e}}_z$ is the dimensionless lag vector (lag normalized by inner tip seal radius) in the principal directions. Note that s^2 only refers to a variance and $\mathbf{s}$ or $s_{d,x/y/z}$ only refer to separation vectors. Values of the various parameters are presented in Table (2.2).

The synthetic log permeability is a lognormally distributed field represented by a nested, anisotropic semivariogram:

The dimensions of the superblocks and their univariate statistics are

Magnification	Dimensionless Width	Dimensionless Length	Dimensionless Depth	$m[\ln(k)]$	$s^2[\ln(k)]$
x 1	25.1	75.1	12.5	-0.03029	0.44238
x 2	12.55	62.55	6.25	-0.05343	0.42875
x 4	6.275	56.275	3.125	-0.1374	0.42932
x 8	3.138	53.138	1.562	-0.23743	0.51383
x 16	1.569	51.569	0.78125	-0.2439	0.5751

Table 2.3: Superblock dimensions and statistics

presented in Table (2.3), and their semivariograms are shown in Fig. (2.13), on which the dashed lines represent the semivariograms calculated from the synthetic fields, and the solid lines represent the model values.

Both the mean and the variance vary, and neither shows any particular pattern in doing so. What accounts for this? If there is any pattern at all, it is that the variance increases as the size of the grid-blocks decreases. This result is consistent with the regularization described by Journel and Huijbregts in [1978], but is unexpected in this context. Journel and Huijbregts demonstrated that the variance of a *volume averaged* property increases as sample support decreases. This should not be the case here. Our scheme presumes that the permeability is continuous and that as we change magnification level we are simply evaluating that continuous function at finer and finer resolution. As mentioned earlier, this amounts to high-frequency sampling of the permeability, which should have no effect on the summary statistics under the assumption that the sampling region is sufficiently large to ensure stationarity. From Fig. (2.13), the semivariogram in the x direction is very faithfully replicates the model, the semivariogram in the z direction consistently lies above the model, and the semivariogram in the y direction shows an increase in the
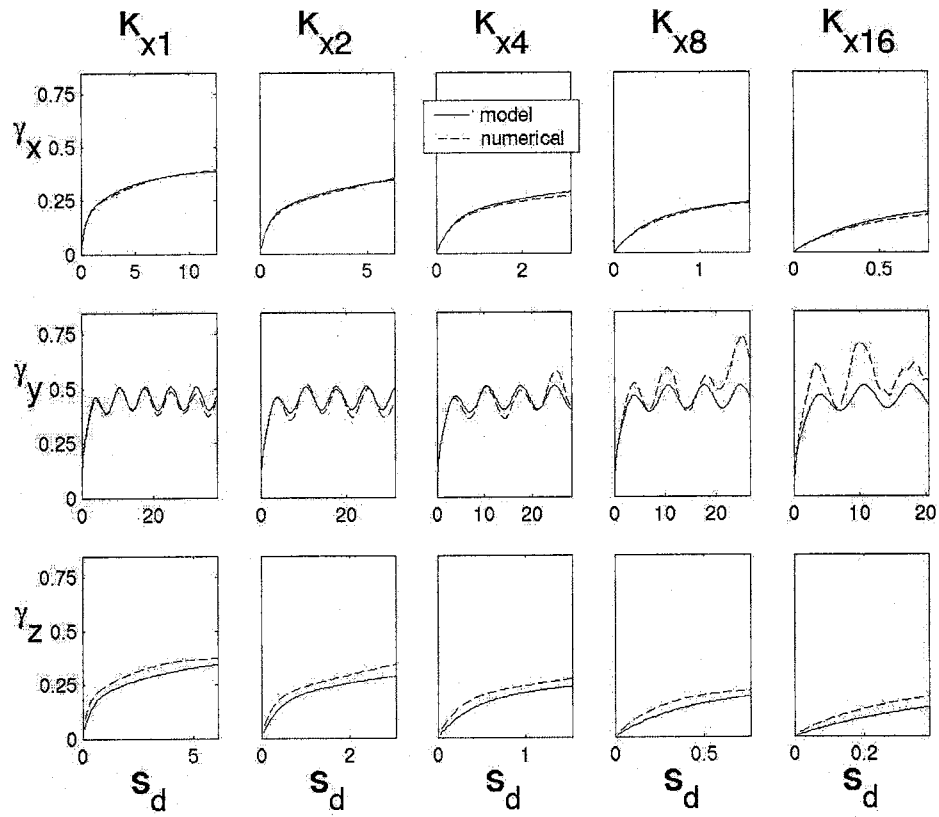
Figure 2.13: Superblock semivariograms of $\ln(k)$

amplitude of the hole-effect variance as magnification level increases. If we had somehow inadvertently introduced regularization, it would not look like this.

In fact, what is going on is that the assumption of stationarity is not valid for the high magnification superblocks. These regions, as can be seen from Table (2.1) and Fig. (2.6)–Fig. (2.9), are relatively narrow and shallow, and hence not representative of the global statistics. This can be shown by calculating the mean, variance and semivariogram of the coarse k_1 superblock in the sub-volumes that overlap the higher magnification superblocks. Table (2.4) shows the univariate statistics in the overlapping volumes. In comparison with Table (2.3), the statistics closely resemble those of the magnified superblocks. Fig. (2.14)–Fig. (2.17) superimpose y-direction semivariograms calculated from the high resolution superblocks, k_2–k_{16}, on y-direction semivariograms calculated from the corresponding subvolumes of k_1. The semivariograms very nearly overly each other for k_2– k_8. Only the semivariograms for k_{16} are noticeably different, though the difference is considerably less than that between the model and experimental values. Overall, the similarities give some reassurance that the departure of the magnified superblocks from the expected statistical measures is simply a result of local bias due to the limited size of the domain. The magnified fields do preserve the statistics of the data on which they were conditionally simulated (i. e., the k_1 log permeability field in the corresponding subvolume).

Magnification of Overlapped Volume	$m[\ln(k_1)]$	$s^2[\ln(k)]$
x 2	-0.05892	0.42962
x 4	-0.14173	0.43551
x 8	-0.22487	0.52365
x 16	-0.2475	0.65288

Table 2.4: Statistics of $\ln(\mathbf{k}_1)$ in magnified sub-volumes
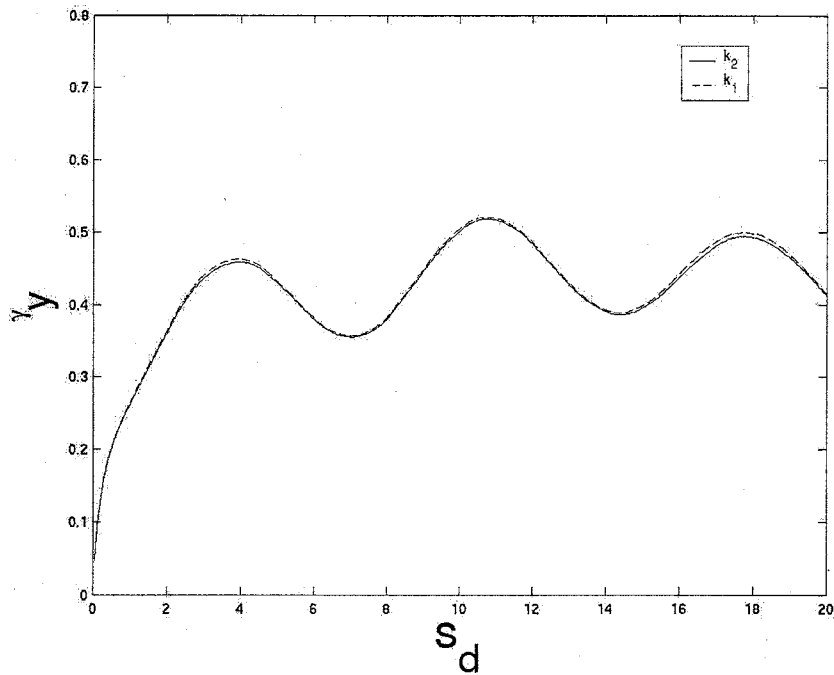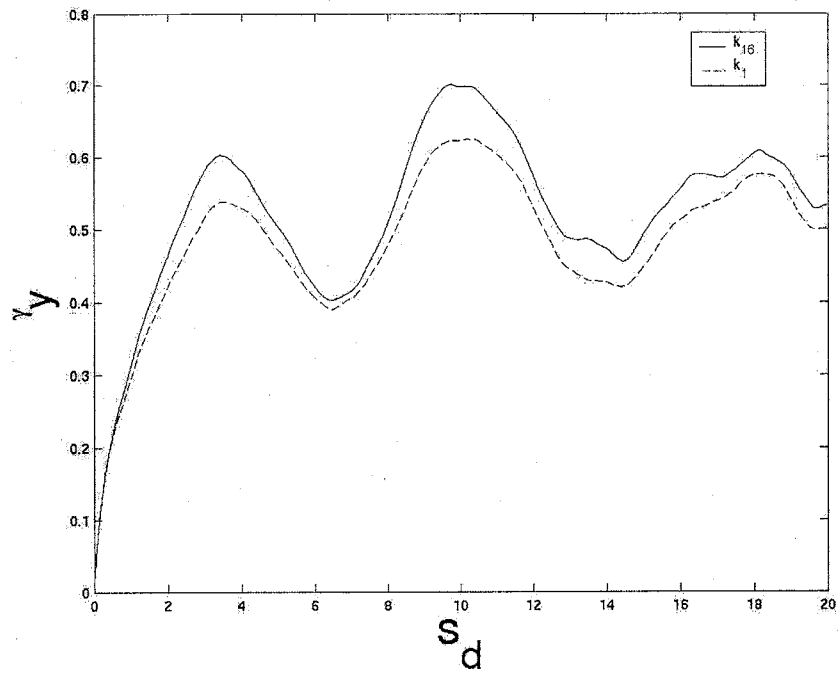

Figure 2.14: Comparison between semivariogram, γ_y, for k_2 superblock (solid line) and corresponding volume of k_1 superblock (dashed line)
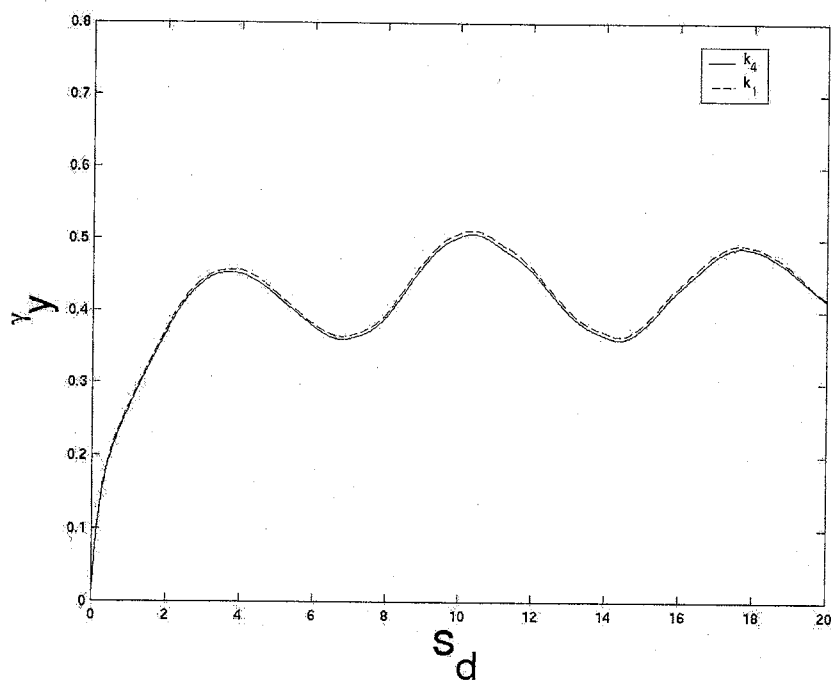
Figure 2.15: Comparison between semivariogram, γ_y, for k_4 superblock (solid line) and corresponding volume of k_1 superblock (dashed line)
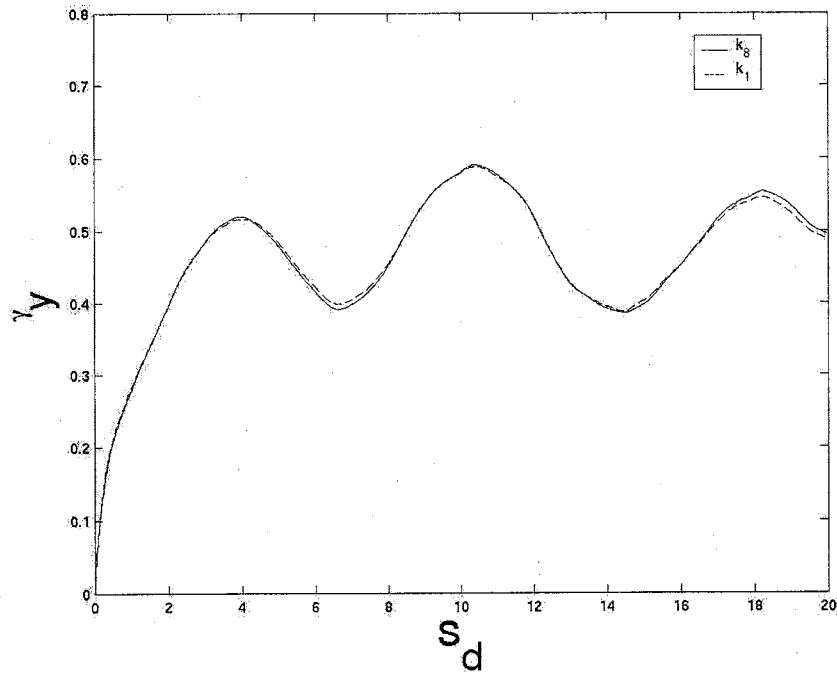
Figure 2.16: Comparison between semivariogram, γ_y, for k_8 superblock (solid line) and corresponding volume of k_1 superblock (dashed line)

Figure 2.17: Comparison between semivariogram, γ_y, for k_{16} superblock (solid line) and corresponding volume of k_1 superblock
(dashed line)

CHAPTER 3

RESULTS AND DISCUSSION

3.1 Univariate Statistical Comparison of Numerical and Laboratory Results

The effective, numerically calculated log permeability along the numerically-modeled transect is shown in Fig. (3.1). A single transect of the laboratory data consists of only fifty measurement points. In order to facilitate comparison between the numerical and laboratory results, we compare a transect of the laboratory data across the bedding (the 26th column of Fig. (2.10)) to an arbitrary selection of fifty consecutive points in the numerical transect in Fig. (3.2). The laboratory data have been normalized to display on the same scale used for the numerical data. The laboratory values of the natural log of the dimensionless permeability for the xi tip-seal, $\ln(k_{d,i})$, were normalized by subtracting the sample mean of the natural log of the $x16$ (i. e.,0.15 cm) tip-seal from each value, so

$$\ln(k_{lab,normalized}) = \ln(k_{d,i,lab}) - m[\ln(k_{d,16,lab})].$$

We obtain the dimensionless permeability k_d by dividing by the unit permeability. For the sake of brevity, we suppress the subscripts "normalized" and "d", so that from here on, $\ln(k_{lab})$ really means $\ln(k_{d,lab,normalized})$ and $\ln(k_{num})$ really means $\ln(k_{d,num})$. Except where otherwise noted, the subscripts "num"

56
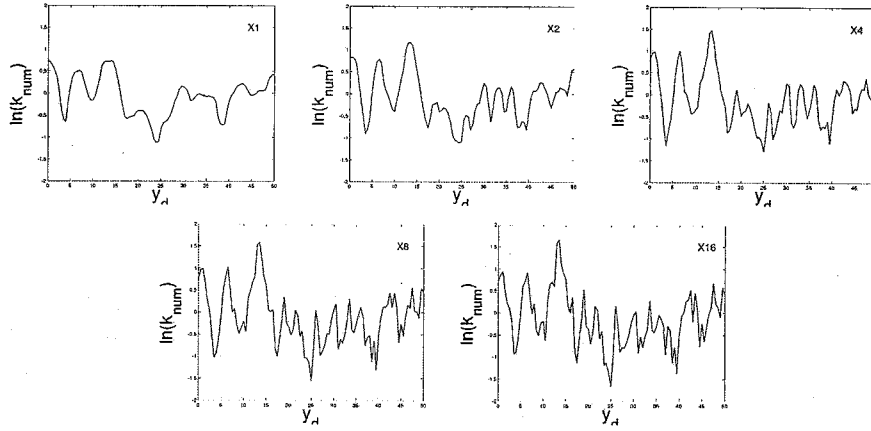
Figure 3.1: Natural log of the numerical dimensionless permeability

Magnification	$m[\ln(k_{num})]$	$s^2[\ln(k_{num})]$	$m[\ln(k_{lab})]$	$s^2[\ln(k_{lab})]$
x 1	-0.0636	0.1983	1.1997	0.1449
x 2	-0.0848	0.2783	0.8524	0.2254
x 4	-0.1115	0.3408	0.5438	0.2593
x 8	-0.1198	0.3805	0.2666	0.3007
x 16	-0.1316	0.4091	0.0000	0.4013

Table 3.1: Univariate statistics of numerical and laboratory results

and "lab" also refer to the measurements of the effective permeability, not the point-scale permeability of the underlying field.

A casual inspection of Fig. (3.2) is revealing. First, both sets of measurements show the distinctly periodic character at the expected wavelength. Second, both sets of measurements are smoothed as the tip-seal size increases. However, while the $\ln(k_{1,num})$ and $\ln(k_{1,lab})$ values appear comparably smooth, the laboratory results seem to posses more power at high spatial frequencies for the smaller tip-seals. In plain English, the $x2$–$x16$ laboratory results look
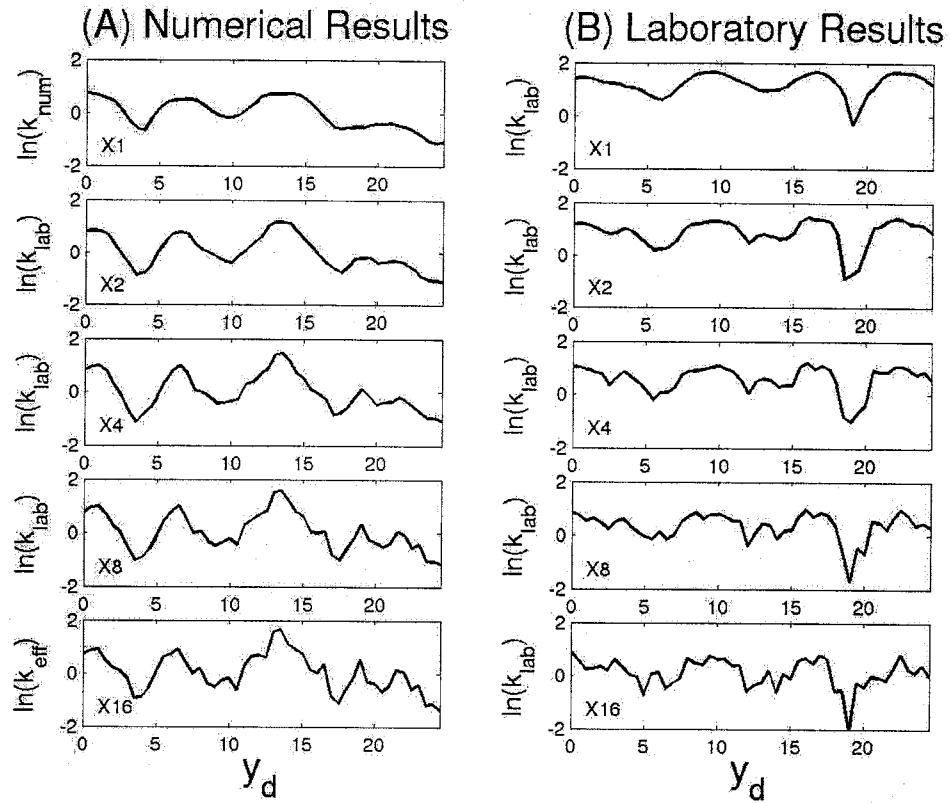
Figure 3.2: Comparison between numerical and laboratory $\ln(k_d)$
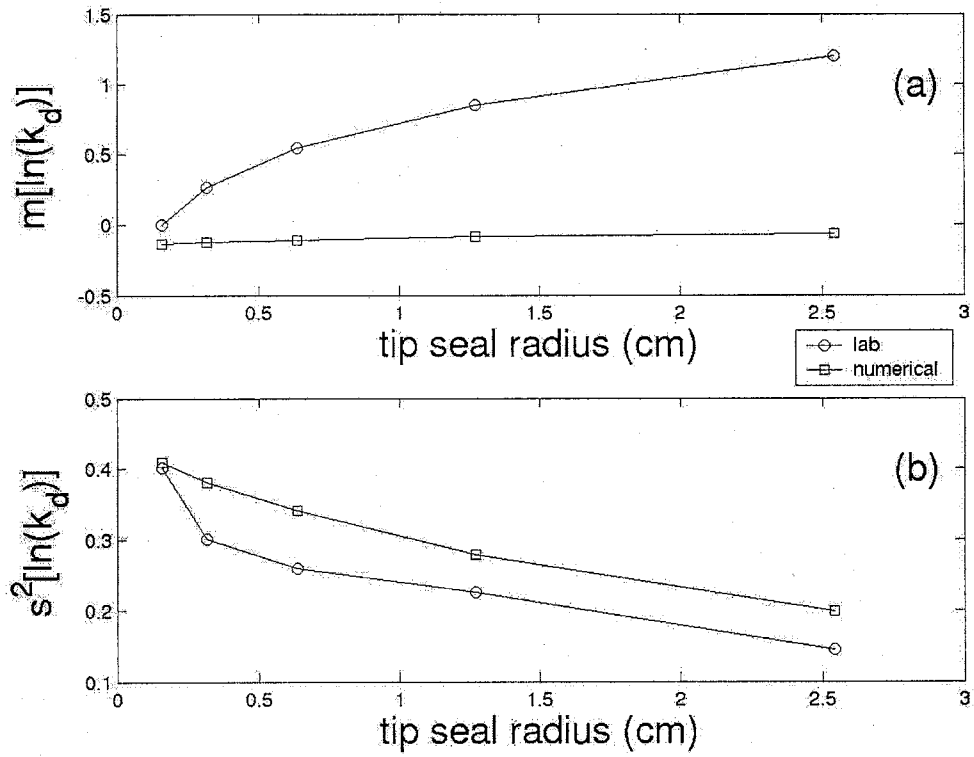
Figure 3.3: Permeability upscaling: a comparison between numerical and laboratory results

more jagged than the corresponding numerical results. One metric of smoothness is the variance, plotted for the complete sets of numerical and laboratory measurements (not just the transects shown on Fig. (3.2)) on Fig. (3.3b) and tabulated in Table (3.1). The variance of both data sets is nearly identical for the $x16$ tip seal, but the variance of the laboratory results is lower than that of the laboratory results for the larger tip-seals, confirming our qualitative observation. Compare the change in the variance of the numerical effective log permeability in Table (3.1) to the change in the variance of the log permeability of the synthetic field in Table (2.3). The log permeability variance of the synthetic field decreased from $x16$ to $x1$ as a result of local bias. Thus, the decrease in the variance of the effective numerical values may simply reflect the decrease in the variance of the underlying field that the numerical min-permeameter samples. However, we reject this conclusion on the basis that the laboratory values, which exhaustively sample the rock face and are thus less prone to the effects of local bias, also show a decrease in log effective permeability as tip-seal size increases. Third, a clear trend in the mean of the laboratory results is apparent: $\ln(k_{lab})$ increases as tip-seal size increases. No such trend is apparent for the numerical results. The mean of the two sets of measurements is plotted on Fig. (3.3a) and tabulated in Table (3.1). We see the obvious trend for the laboratory data here, but only slight upward trend for the numerical results. The trend in the numerical results is consistent, but so small that we cannot give it significance.

Two effects, overlapping and increase of support, may be at work to lower the variance as tip-seal size increases. By overlapping, we mean that for a pair of measurement points, the sample support at each point increases
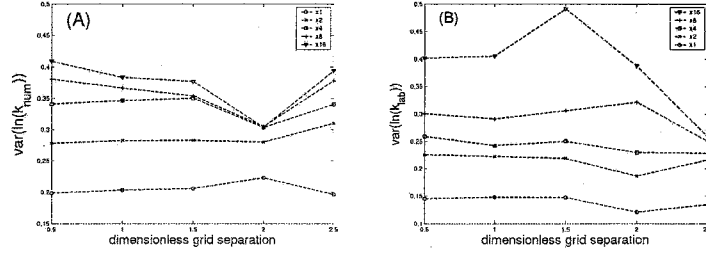
Figure 3.4: Variance of $\ln(k_d)$ as a function of grid separation for (A), numerical results and (B), laboratory results.

with the size of the tip-seal used to make the measurement. As a result, the supports of the two measurements intersect one another to a greater extent for larger tip-seals. We can distinguish the effect of overlap from the effect of sample support by considering the variance of the data as a function of grid separation. The measurement grid for both numerical and laboratory data sets is 0.5 dimensionless length units. We calculate the variance of data subsets consisting of measurements separated by 1.0, 1.5, 2.0 and 2.5 dimensionless length units. The results are plotted on Fig. (3.4). There is no particular trend in the variance as we change the separation between measurements. This means that the smoothing is not, as far as we can tell, a function of overlap, but of change of sample support only.

As the tip-seal size increases, so too does the volume of the sample support. As the linear dimensions of the sample support approach the correlation length of a given characteristic spatial structure of the underlying permeability, we lose the ability to resolve that structure. Compare the size of each tip-seal to the correlation lengths of the underlying permeability field. We define the dimensionless correlation length $\lambda_d \equiv \frac{\lambda}{a}$, where λ is the correlation

length and a is the inner tip-seal radius. The dimensionless correlation lengths for the three characteristic spatial structures estimated from the laboratory data set [Tidwell and Wilson, 1997] in the principal directions, $\lambda_{d,xn}^i$, $\lambda_{d,yn}^i$, and $\lambda_{d,zn}^i$, for each tip-seal are shown in Table (3.2). The superscript "i" in this case indexes the characteristic spatial structure, per Table (2.2), and the subscript "n" refers to the tip-seal size. For example, $\lambda_{d,y2}^1$ refers to the dimensionless correlation length of the small- scale exponential structure in the y direction (i. e., perpendicular to bedding) relative to the $x2$ tip-seal. The small-scale dimensionless correlation length changes as we go from the $x1$ tip-seal to the $x16$ tip-seal from $\lambda_{d,y1}^1 = 0.59$ to $\lambda_{d,y16}^1$. The dimensionless correlation length goes from being somewhat smaller than the $x1$ tip seal to being just less than an order of magnitude larger than the $x16$ tip-seal. Thus, we expect that the signal from the small-scale structure to be completely filtered out for the $x1$ tip-seal and to reemerge as tip-seal size decreases. Referring to Table (2.2), this would mean that the difference in variance between measurements of the $x1$ tip-seal and $x16$ tip-seal should be about 0.17, the sill value of the small-scale exponential structure. From Table (3.1), the difference is 0.2108 for the numerical data set and 0.2664 for the laboratory data set. We interpret this to mean that the small-scale structure is completely filtered out and that. In addition, the $x1$ tip-seal is too big to completely resolve even the large-scale exponential structure, as variance of 0.1983 is less than the sill value of the large-scale exponential structure, 0.23. We will revisit this issue again when we analyze semivariograms calculated from both numerical and laboratory results.

We interpret the similarity in the variance upscaling between the numerical and laboratory results as confirmation of the validity of the magnifi-

Magnification	Small-Scale		Large-Scale		Hole-Effect	
	$\lambda^1_{d,y}$	$\lambda^1_{d,(x,z)}$	$\lambda^2_{d,y}$	$\lambda^2_{d,(x,z)}$	$\lambda^3_{d,y}$	$\lambda^3_{d,(x,z)}$
x 1	0.59	1.06	7.09	13.0	7.09	N/A
x 2	1.18	2.12	14.18	26.0	14.18	N/A
x 4	2.36	4.24	28.36	52.0	28.36	N/A
x 8	4.72	8.48	56.72	104.0	56.72	N/A
x 16	9.44	16.96	113.44	208.0	113.44	N/A

Table 3.2: Dimensionless correlation lengths [Tidwell and Wilson, 1997]

cation routine as a means of parameterizing the permeability field at different scales. Heuristically, the variance reveals the smoothing or averaging of the underlying field by the instrument. The consistency in the scaling of the variance between numerical and laboratory experiments suggests that the numerical model of the log permeability field as the resolution of the grid increases corresponds to the behavior of the physical log permeability field as the size of the tip-seal decreases.

The most glaring difference between the laboratory and numerical results is the upscaling of the mean log permeability. This is important because the trend in the mean is the crucial element we wish to explore. The laboratory results show an obvious increase in the mean as tip-seal size increases, while the mean of the numerical results appears essentially unchanged. In fact, the mean log permeability of the numerical measurements *does* increase, but much less than that of the laboratory measurements (see Fig. (3.3a) and Table (3.1)). In this case, we cannot blame to discrepancy on the smaller sample size of the numerical data set: statistics calculated on single transects taken from the laboratory data show virtually the same upscaling trends in both mean and

variance of the ensemble laboratory data as shown in Fig. (3.3).

Clearly, the synthetic permeability does not possess whatever quality or qualities that account for the upscaling of the laboratory field. We show in Fig. (2.13) that the synthetic numerical permeability faithfully reproduces the prescribed statistics of Eq. (2.88). What, then, is the missing ingredient? Physically, the upward trend in the mean log effective permeability is caused by relatively greater mass transport of gas by larger tip-seals than smaller tip-seals on average. The most plausible mechanism for enhanced mass transport as a function of tip seal radius is the availability of preferential flow paths. Such flow paths would arise if the permeability field were characterized by connectivity of like permeability values extending over the range of spatial scales corresponding to the range of measurement scales that demonstrate the upscaling trend. In a medium characterized by the sort of laminar anisotropy present in the Massillon sandstone, connectivity of either low or high permeability regions would have the effect of creating channels of relatively high permeability. Channelization of permeameter flow was not apparent in the numerically modeled Massillon. We identify three possible causes for the absence of channelization: the synthetic log permeability field is qualitatively different from actual log permeability field; the punctual log permeability values of the laboratory sample are not Normally distributed, as the synthetic field is; and the simulation fails to capture the small-scale features of the laboratory sample. We discuss the first two of these in the remainder of this section and the last in the following section.

We immediately note the qualitative difference between the permeability map of the laboratory data set and the synthetic permeability. Compare

Fig. (2.6) to Fig. (2.10). Both permeability fields are anisotropic and show a bedding pattern. The laboratory image, however, shows far more structure. Perpendicular to bedding, the synthetic field shows alternating bands of high and low values of equal thickness, while the laboratory image is characterized by wide bands of high permeability values alternating with thinner lenses (bounding surfaces) of low permeability values. Parallel to bedding, both high and low permeability regions are coherent over greater widths. In addition, an angular unconformity is present in the laboratory image at the top left. It is clear that simulation that honors semivariograms, as is the case for the synthetic field, does not necessarily honor the physical features from which those semivariograms are calculated. As noted by Pyrcz and Deutsch [2003], the relationship between a hole-effect semivariogram and the field from which it is calculated is non-unique: any number of periodic structures (e. g., regularly or irregularly clustered lenses, regular or irregular strata) may have identical spatial correlation structure. Correctly reproducing the qualitative features of the laboratory sample might entail using a hierarchical simulation procedure, in which regions of "high" or "low" permeability are simulated using an indicator algorithm, then punctual permeability values are assigned using a second simulation routine (perhaps sequential Gaussian simulation) within each region.

We can also see substantial quantitative differences between the numerical and laboratory permeabilities. Fig. (3.5) and Fig. (3.6) show the cumulative distribution functions of $\ln(k_{num})$ and $\ln(k_{lab})$, respectively. The results are consistent with what we have seen already. Both sets of CDFs become narrower as tip-seal size increases, showing the decreasing trend in variance. The increase in the mean log permeability is seen in the positive shift of the
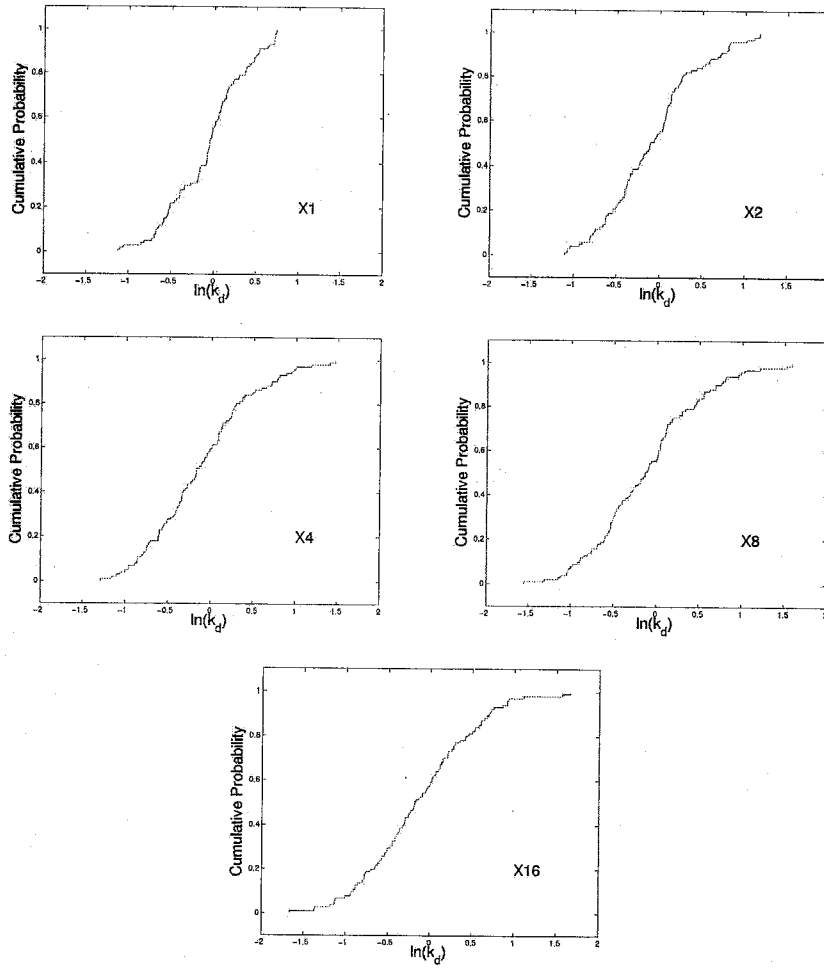
Figure 3.5: Cumulative distribution functions for numerical data set
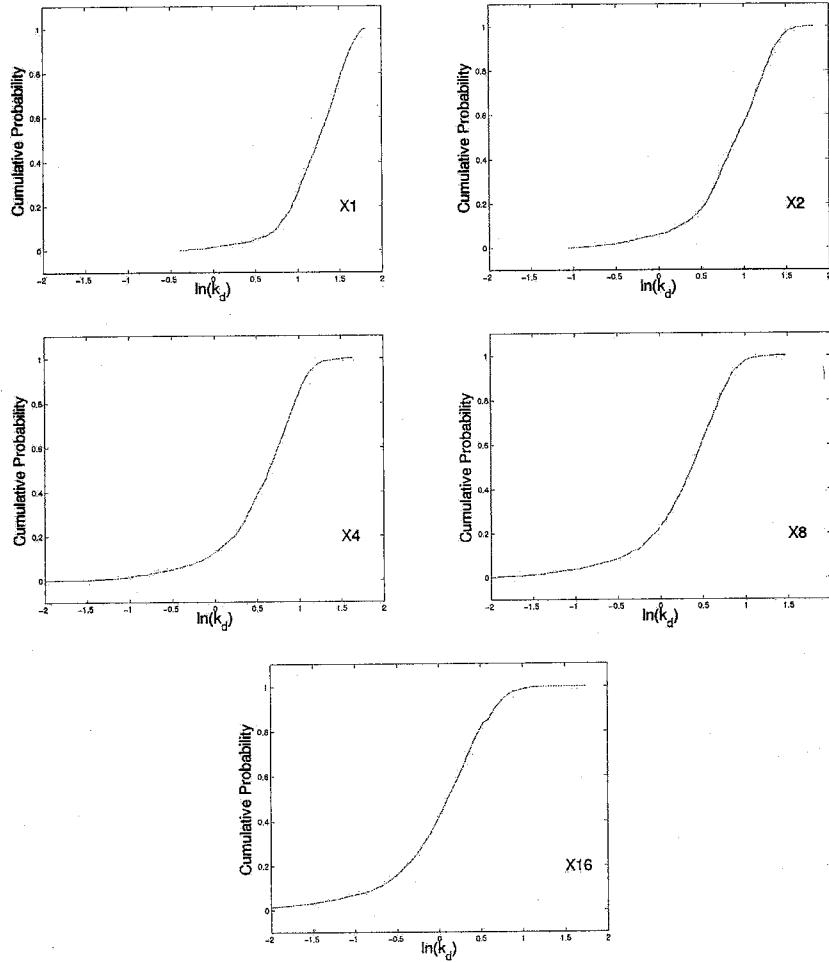
Figure 3.6: Cumulative distribution functions for laboratory data set
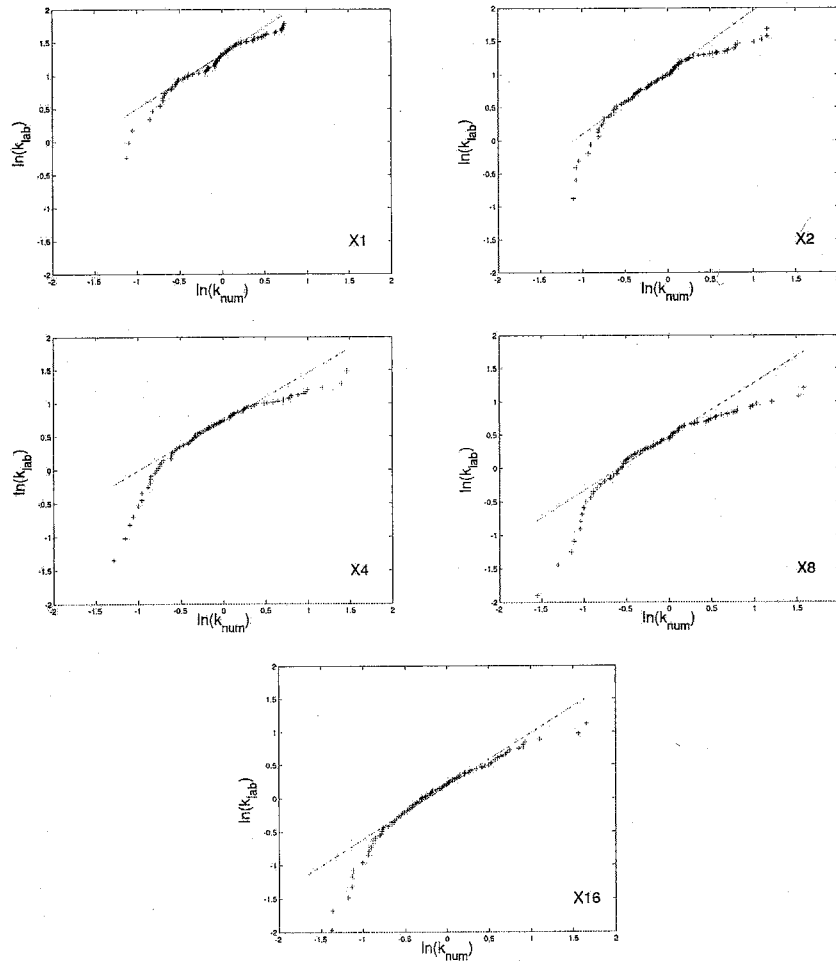
Figure 3.7: Q-Q plots of numerical and laboratory data

CDFs as tip-seal size increases. We see the slight increase in the mean of the numerical results better here than in Fig. (3.4a). Also note that the laboratory results are negatively skewed compared to the corresponding numerical results, indicating that the laboratory measurements are not log-normally distributed (*cf.* Fig. 2.10), contrary to the simplifying assumption made by Tidwell and Wilson [1997].

The skew is even more apparent from Fig. (3.7), Q-Q plots comparing quantiles of the numerical and laboratory data. The Q-Q plots vividly show the much greater upward trend in the mean of the laboratory results as tip-seal increases, as compared to the numerical results. While the long lower tail of the laboratory results was previously evident, we can also see much more clearly a truncated upper tail. In fact, we see that the negative skew becomes more pronounced as tip-seal size decreases: the negative tail gets longer and the positive tail more truncated. Overall, we conclude that the upward shift of the mean is not a result of a few outliers, but is an across-the-board increase in effective permeability. We don't see a similar pattern in the numerical results, which are predictably lognormally distributed.

This distributional anomaly is significant. The long low-value tail has the effect of moving log permeability values in the tail farther away from the median than they would be for a Gaussian distribution. As a consequence, the skewed distribution has a break, where the tail begins, below which punctual log permeability values are lower than they would be in the Gaussian distribution. The break divides the skewed distribution into a sub-populations of low and high log permeability values. In a Gaussian distributed, spatially correlated

field, like log permeabilities tend to cluster together, with regions of high log permeability smoothly transitioning to regions of low log permeability. A log permeability field that follows the skewed distribution characteristic of the laboratory data loses some of that smoothness.

To illustrate this, imagine that we perform a Normal-score transform on the one of the Gaussian-distributed synthetic log permeability fields used here. For the sake of illustration, suppose the break dividing the high and low sub-populations is located at $\ln(k_d) = -1$ (see Fig. (2.11)). All punctual log permeability values below -1 in the original synthetic field will be assigned some lower value according to the transform table. The spatial structure of log permeabilities would be unaffected, but the punctual log permeabilities below -1 would now be lower in comparison to the remainder of the field, creating distinctive "blocks" of low log permeabilities within a matrix of otherwise Gaussian-distributed high log permeabilities. By increasing the constrast between high and low values, the Normal-score transform creates the potential for channelization of flow through connected high log permeability regions bounded by connected low log permeability regions. Treated as a hypothesis, this scenario can be easily tested by employing a Normal-score transform on the sequential Gaussian simulated log permeability values, and running the flow code on both the transformed and untransformed fields.

3.2 Geostatistical Comparison of Numerical and Laboratory Results

Fig. (3.8) shows a set of three superimposed semivariograms for each tip-seal. The black dots are semivariograms calculated from the numerical ef-

fective log permeability values, the solid lines are semivariograms we fit to the numerical semivariograms (i. e., the solid lines are fit to the black dots), and the dashed lines are the semivariograms Tidwell and Wilson [1997] fit to the $x16$ tip-seal laboratory data set. Superimposed on the semivariograms calculated from the numerical measurements are semivariograms fitted to the calculated versions and semivariograms fitted to the appropriate set of laboratory measurements. Both sets of fitted semivariograms retain the nested functional form of Eq. (2.88), but the sill/amplitude and range parameters have been changed to achieve the best fit. The parameters for the semivariograms fitted to the numerical data are shown in Table (3.3) and the parameters Tidwell and Wilson [2000[fit to the laboratory data are shown in Fig. (3.4). We did the fitting by eye, emphasizing closeness of fit at short ranges over long ranges. It can be seen that the fit, while as good as possible for the given functional form, is questionable. Note the pronounced long-range upward trend in the semivariogram calculated from the numerical data (the black dots in Fig. (3.8)), which seems to be the primary culprit for the poor fit to the numerical semivariogram.

What accounts for this long range trend in the effective numerical log permeability that is not present in the effective laboratory log permeability (Fig. (2.12))? The trend is present for all tip-seal sizes, so this is not an upscaling trend so much as something symptomatic of the instrument itself. The first question that should be answered is whether the trend is present in the underlying permeability field. Referring to Fig. (2.13), it appears that this is the case, that the underlying synthetic log permeability field does show a similar upward trend. Thus, this feature in the semivariogram calculated from the effective numerical log permeability reflects to some degree the same feature

71
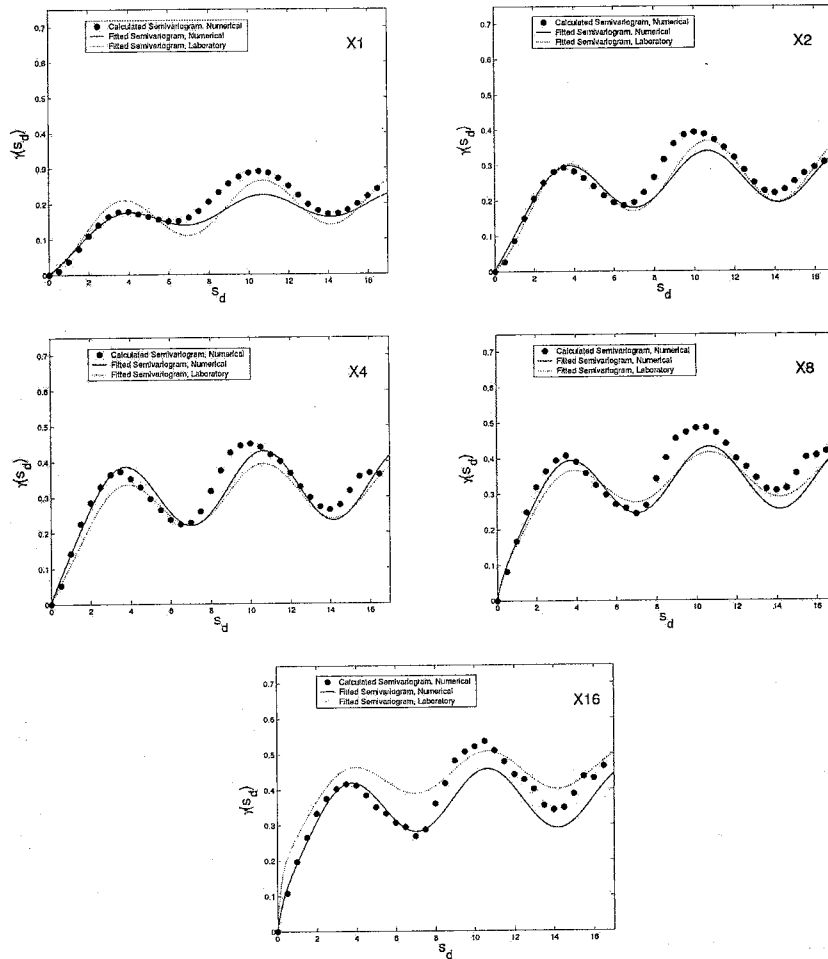
Figure 3.8: Numerical and laboratory empirical semivariograms and semivariogram fitted to laboratory semivariogram.

Magnification	Small-Scale		Large-Scale		Hole-Effect	
	s_1^2	$\lambda_{y,1}$	s_2^2	$\lambda_{y,2}$	s_3^2	$\lambda_{y,3}$
x 1	0.045	9.0	0.12	12.09	0.035	7.09
x 2	0.065	3.0	0.13	10.09	0.075	7.09
x 4	0.075	2.0	0.16	9.09	0.10	7.09
x 8	0.085	1.2	0.17	7.59	0.09	7.09
x 16	0.1	0.99	0.19	7.09	0.085	7.09

Table 3.3: Semivariogram parameters Fit to numerical data

Magnification	Small-Scale		Large-Scale		Hole-Effect	
	s_1^2	$\lambda_{y,1}$	s_2^2	$\lambda_{y,2}$	s_3^2	$\lambda_{y,3}$
x 1	$\cdots$	$\cdots$	0.15	15.94	0.068	7.09
x 2	$\cdots$	$\cdots$	0.20	11.22	0.090	7.09
x 4	0.02	1.30	0.22	8.86	0.080	7.09
x 8	0.06	0.83	0.23	7.68	0.065	7.09
x 16	0.17	0.59	0.23	7.09	0.055	7.09

Table 3.4: Semivariogram parameters fit to laboratory data [Tidwell and Wilson, 2000]

in the underlying permeability field of which the effective values are a measure.

Examination of the semivariogram parameters fitted to the numerical effective log permeability semivariogram does reveal upscaling behavior complementary to that seen for the laboratory data. As with Tidwell and Wilson [2000], the sill values of both exponential semivariogram structures decreases as tip-seal size increases, with the relative contribution of the small-scale structure decreasing rapidly. The amplitude of the hole-effect structure increases with tip-seal size to a point and then drops. We see here clearly the preferential filtering we noted above in our discussion of the global variance. For the laboratory results, the contribution of the small-scale structure is entirely filtered

out for the $x1$ and $x2$ tip-seals, which is intuitively sensible and in keeping with Beckie's [1996] observation that physics above the Nyquist frequency cannot be resolved. The contribution of the small-scale structure to the semivariogram fit to the numerical results does not fall off nearly as precipitously as for the laboratory results nor is it filtered out completely. Also consistent with Tidwell and Wilson [2000], the range of the exponential structures increases with tip-seal size.

The significance of the upscaling of the sill values has already been discussed in the previous section. The upscaling of the correlation length, as noted by Tidwell and Wilson [2000], simply reflects the fact that, as the tip-seal size increases, two measurements must be separated that much farther apart before the become completely uncorrelated. Once again, these results give us confidence that the numerical scheme accurately models a real world gas minipermeameter, but they tell us little about upscaling processes.

On a different track, one of the questions we wish to answer in this study is how well the gas minipermeameter measures the spatial structure of the underlying permeability. Overall, none of the tip-seals provides a very accurate representation. However, comparing Table (3.3) and Table (3.4), we see that the accuracy of the estimated semivariograms increases as the tip-seal size decreases. For the exponential structures, two trends are apparent: as tip-seal size decreases, the sill approaches the prescribed value from below and the correlation length approaches the prescribed value from above. For the hole-effect structure, the wavelength is accurate for all tip-seals. The hole-effect amplitude also appears to be headed in the right direction as the tip-seal size

decreases, though it is not possible to know if the amplitude and correlation length parameters would truly converge to the correct value. This gives us an indication as to how small the tip-seal must be relative to the correlation length of a permeability field semivariogram in order resolve that correlation length. In the numerical data set, only the correlation length of the large scale exponential structure is well resolved (in that the estimated correlation length from Table (3.3) reflects the actual correlation length from the underlying field), and then only by the $x16$ tip-seal, for which the correlation is 113.44 times the length of the inner tip-seal radius. This suggests that in order for a tip-seal to be used to correctly estimate a correlation length, the inner tip-seal radius must be around two orders of magnitude smaller than the correlation length to be estimated. If this is the case, then the largest correlation length that could be well estimated in the laboratory by the MSP would around one hundred times the inner radius of the smallest tip-seal, or 15 cm. If this is so, then the parameterization of the small-scale exponential semivariogram structure is likely not representative of the actual structure: extrapolating the trends from Table (3.4), the true semivariogram would have a correlation length less than the estimated 0.59 dimensionless length units and a sill higher than the estimated 0.17. It is also plausible that spatial structure exists for this sample at a smaller scale than even the small-scale exponential structure that is completely or nearly completely unresolved, and so a parameterization of the Massillon sandstone based on the small

The incomplete picture of the underlying spatial structure of the Massillon is consistent with the closure problem discussed by Beckie [1996]. Beckie designates variability of the target field (i. e., the field interrogated by an in-

strument) that lies below the scale of the measurement grid as "sub-grid", and notes that such variability can only be partially resolved by a gridded set of measurements. That is precisely the situation encountered here by both laboratory and numerical experiments. While the measurement scale is varied using tip-seals of different size, the sampling scale remains fixed at 1.27 cm between points on the measurement grid (in the case of the laboratory experiment) or transect (in the case of the numerical experiment). Gridded measurements are band-limited and cannot fully resolve variability below the Nyquist interval of the sampling scale, which in this case would be 2.54 cm.

This inability of the smallest laboratory tip-seal to measure the smallest features of the sample may be another reason the numerical experiment fails to upscale in the expected manner. The synthetic field is paramterized by semi-variograms drawn from the laboratory 0.15 cm tip-seal data set, which we have shown to be an incomplete representation of the actual spatial structure of the Massillon. We may reasonably expect that there exist spatial structures smaller than 2.54 cm and these features will contribute, to some degree, to the effective permeability measured by the instrument. We don't know to what extent such features might affect log permeability upscaling, but their absence from the synthetic field begs investigation.

3.3 Spatial Weighting Functions

In order to evaluate the spatial weighting function of the numerical minipermeameter, we have compared effective permeability to the geometrical mean of the underlying field. At each measurement location on the transect, we calculated the geometric mean of the local permeability in a number of

Region	r_d	h_d
A	$\frac{1}{\sqrt{2}}$	$\frac{1}{\sqrt{2}}$
B	1	1
C	$\sqrt{2}$	$\sqrt{2}$
D	2	2
E	3	3
F	4	4
G	5	5
U	inside radius, 1 outside radius, 2	1.5

Table 3.5: Dimensions of averaging regions

concentric cylindrical regions. The axis of the cylinders coincides with the axis of the tip-seal and the dimensions of the cylinders are scaled by the local coordinate system (*cf.* §2.2.3). Thus, the radius, r_{A1}, of the averaging volume A_1 is given by $r_{A1} = \frac{1}{\sqrt{2}}a_1$, where a_1 is the x1 inner tip seal radius. Similarly, the height, h_{A1}, of the averaging volume A_1 is given by $h_{A1} = \frac{1}{\sqrt{2}}a_1$. We define dimensionless radii and heights by normalizing by the appropriate inner tip-seal radius, so that for the $A1$ averaging volume,

$$r_{d,A1} \equiv \frac{(1/\sqrt{2})a_1}{a_1} = \frac{1}{\sqrt{2}},$$

$$h_{d,A1} \equiv \frac{(1/\sqrt{2})a_1}{a_1} = \frac{1}{\sqrt{2}}.$$

The dimensions of the averaging volumes are given in Table (3.5). The region U is an annulus that lies directly beneath the tip seal and extends a depth one-and-a-half times the inner tip seal radius. The region H is the full local domain.

We compare natural log of effective permeability to the natural log of

the geometric mean in each of the cylindrical regions in the figures shown in Appendix B and scatter plots in Appendix C, and in Fig. (3.9)–Fig. (3.17) for the $x16$ tip seal only. In a qualitative sense, we see that the correlation between the geometric mean and the effective permeability is strongest in regions A–C and U, and that the strength of correlation across all regions is better for small tip-seals than large ones.

In order to quantify the cross-correlation between the effective permeability and the volume average, Fig. (3.18) shows the correlation coefficient,

$$\rho = \frac{\frac{1}{N} \sum_{i=1}^{N} \ln\left(k_{eff}\right) \ln\left(k_{geo}\right) - m[\ln\left(k_{eff}\right)] m[\ln\left(k_{geo}\right)]}{\sqrt{s^2[\ln\left(k_{eff}\right)]} \sqrt{s^2[\ln\left(k_{eff}\right)]}}, \qquad (3.1)$$

for regions A–F and U across all sample supports. Two patterns are apparent in Fig. (3.18). First, correlation to the effective log permeability is better for the smaller averaging volume (with an important caveat) and becomes worse as the averaging volumes increase. Second, the correlation between all pairs of effective log permeability and volume average decreases as tip-seal size increases.

That the effective log permeability correlates most strongly with the geometric mean of the small volume averages is not surprising. However, the strongest correlation is not for Region A, the smallest of the averaging volumes, but for Region U (for $x16$, $x8$ and $x4$) and Region B (for $x2$ and $x1$). Both Regions U and B include the grid-blocks that lies adjacent to the edge of the inner tip-seal radius. This is consistent with the work of Aronson [2001] and Molz et al. [2003], who showed for a homogeneous, isotropic permeability field that the narrow annulus lying under the inner radius of the tip-seal contributes most heavily to the effective log permeability. The volumes that encompass
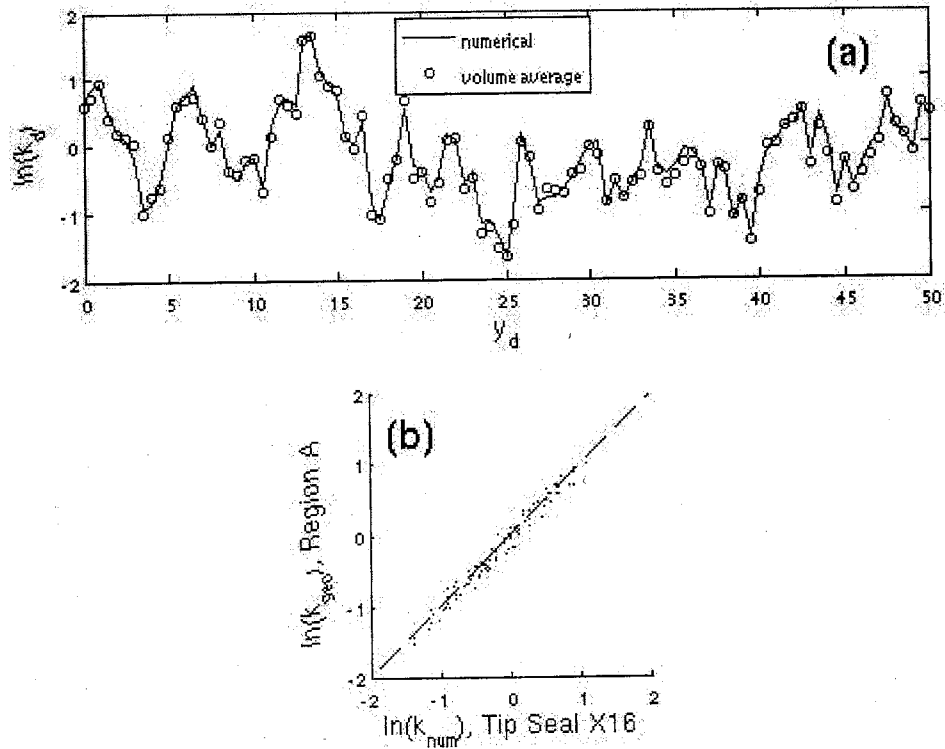
Figure 3.9: (a), Comparison between $\ln\left(k_{16,num}\right)$ and $\ln\left(k_{A16}\right)$. (b), Scatter plot of $\ln\left(k_{A16}\right)$ vs. $\ln\left(k_{16,num}\right)$.

this annulus, Regions B, C and U, all show the strongest correlation with the effective permeability. Region A is next best correlated, followed by Regions D, E, F, G, and H, in that order.

The reasons for the decrease in correlation between the effective log permeability and all volume averages as tip-seal size increases are less clear. We can interpret this in terms of the relationship between the inner tip-seal radius and the correlation length of the underlying permeability field. Recall
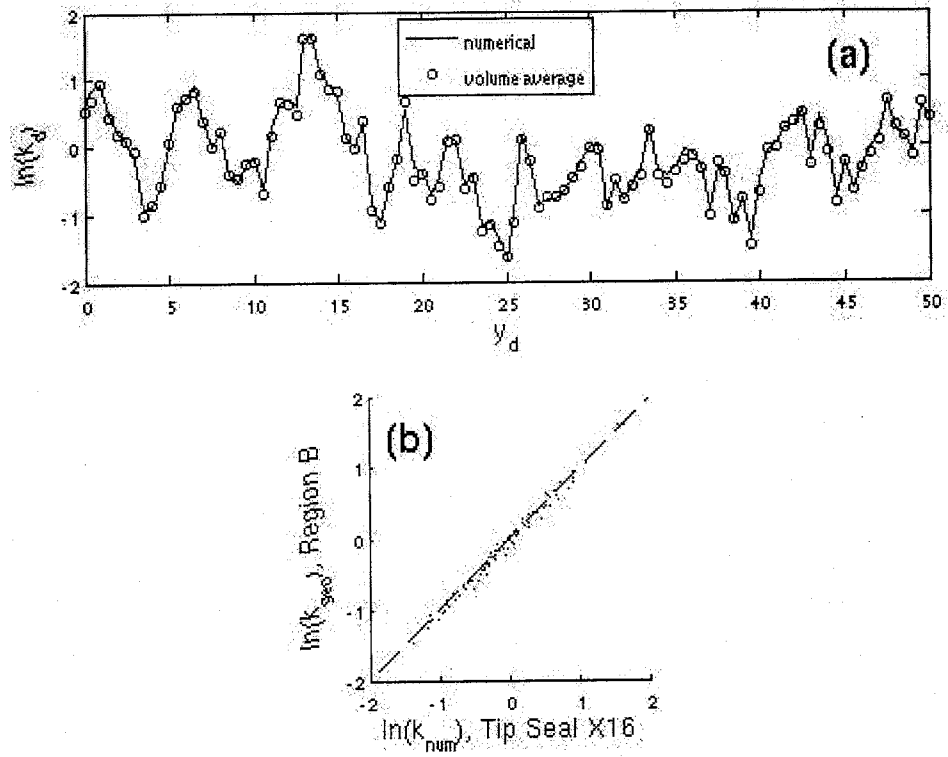
Figure 3.10: (a), Comparison between $\ln\left(k_{16,num}\right)$ and $\ln\left(k_{B16}\right)$. (b), Scatter plot of $\ln\left(k_{B16}\right)$ vs. $\ln\left(k_{16,num}\right)$.
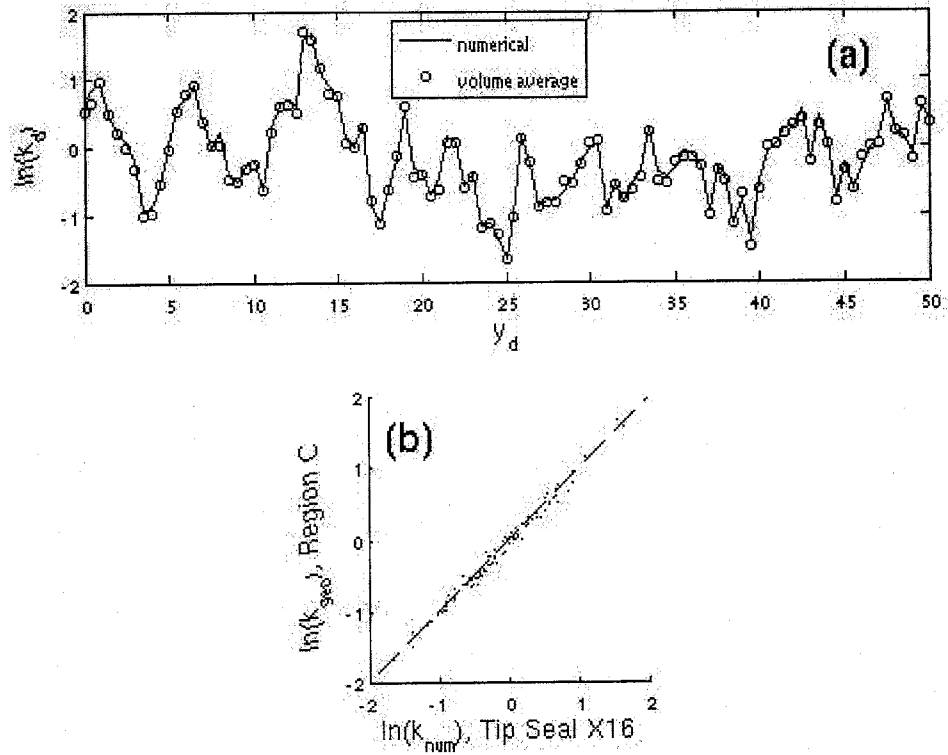
Figure 3.11: (a), Comparison between $\ln\left(k_{16,num}\right)$ and $\ln\left(k_{C16}\right)$. (b), Scatter plot of $\ln\left(k_{C16}\right)$ vs. $\ln\left(k_{16,num}\right)$.
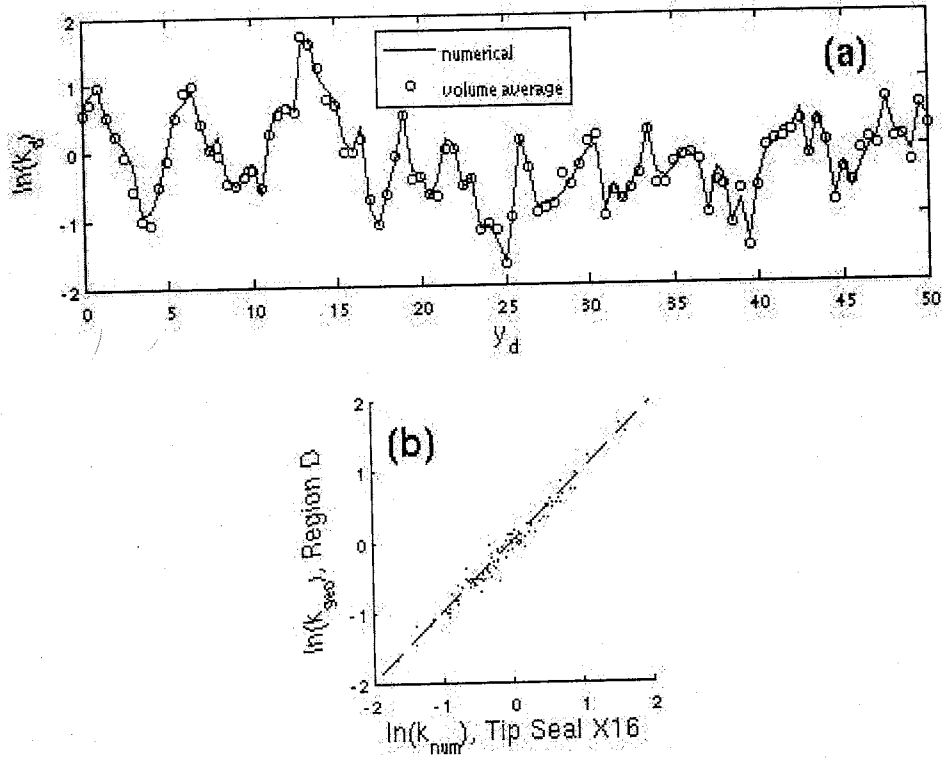
Figure 3.12: (a), Comparison between $\ln\left(k_{16,num}\right)$ and $\ln\left(k_{D16}\right)$. (b), Scatter plot of $\ln\left(k_{D16}\right)$ vs. $\ln\left(k_{16,num}\right)$.
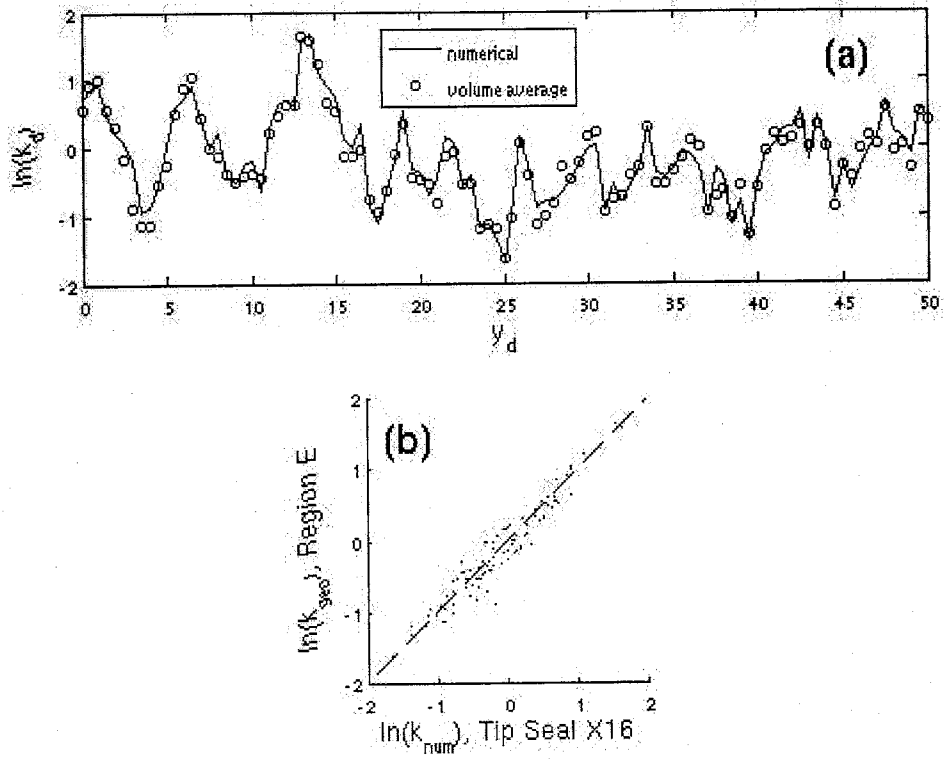
Figure 3.13: (a), Comparison between $\ln\left(k_{16,num}\right)$ and $\ln\left(k_{E16}\right)$. (b), Scatter plot of $\ln\left(k_{E16}\right)$ vs. $\ln\left(k_{16,num}\right)$.
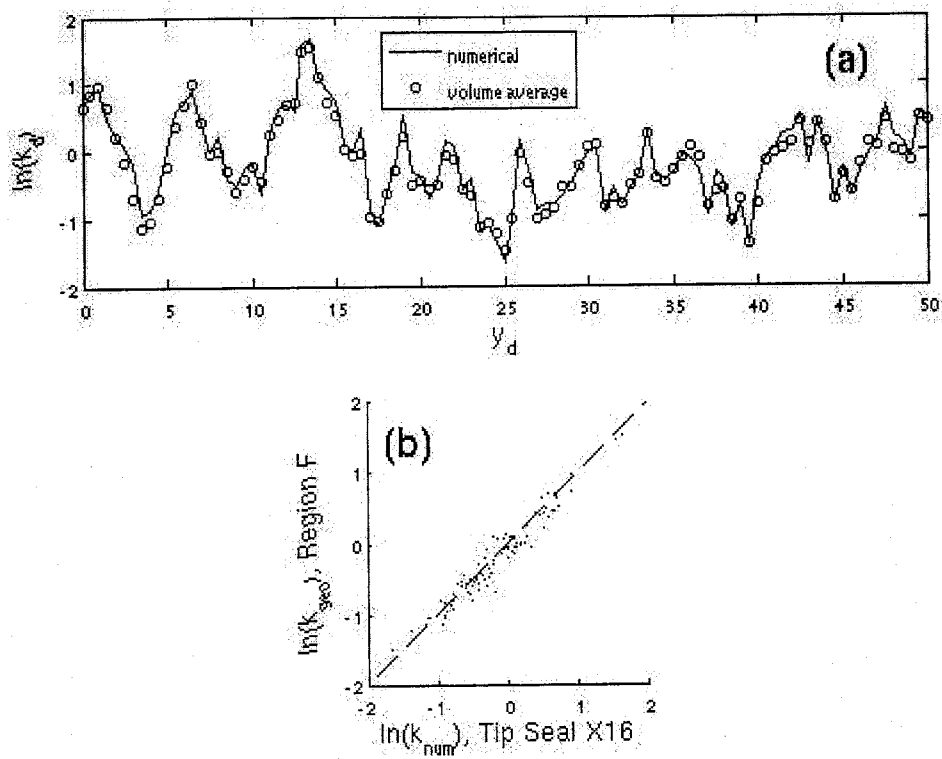
Figure 3.14: (a), Comparison between $\ln\left(k_{16,num}\right)$ and $\ln\left(k_{F16}\right)$. (b), Scatter plot of $\ln\left(k_{F16}\right)$ vs. $\ln\left(k_{16,num}\right)$.
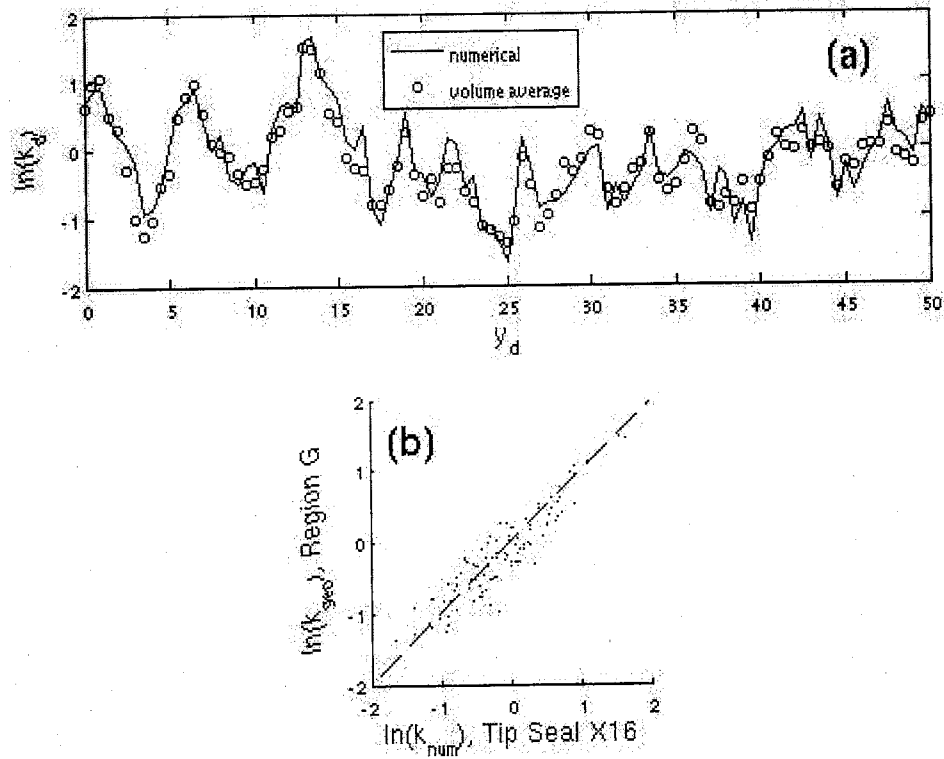
Figure 3.15: (a), Comparison between $\ln(k_{16,num})$ and $\ln(k_{G16})$. (b), Scatter plot of $\ln(k_{G16})$ vs. $\ln(k_{16,num})$.
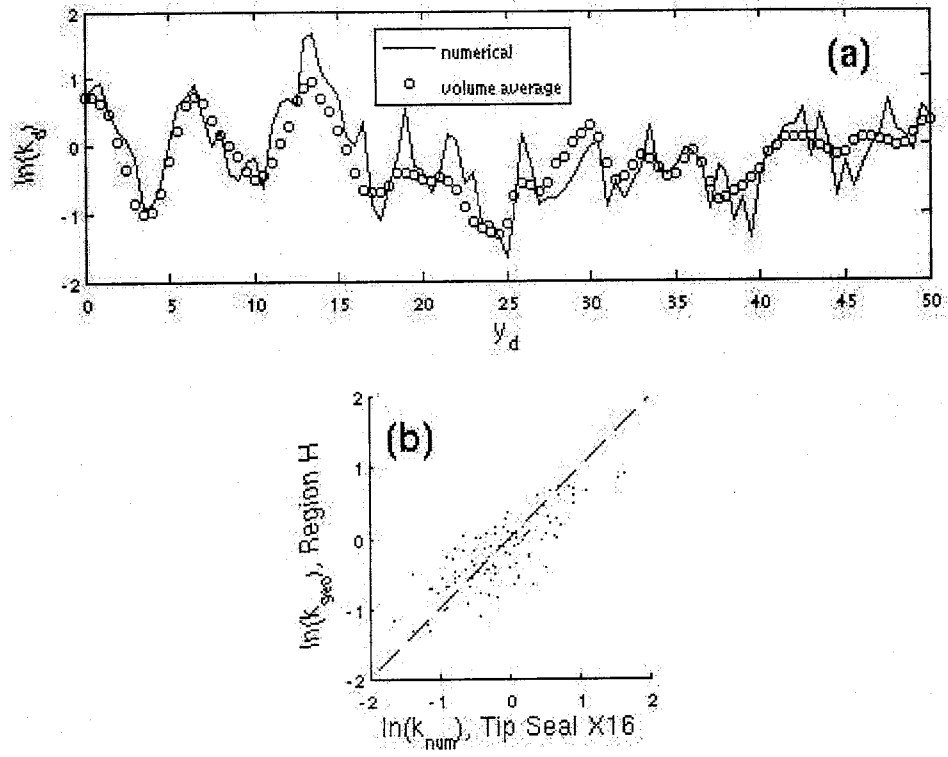
Figure 3.16: (a), Comparison between $\ln(k_{16,num})$ and $\ln(k_{H16})$. (b), Scatter plot of $\ln(k_{H16})$ vs. $\ln(k_{16,num})$.
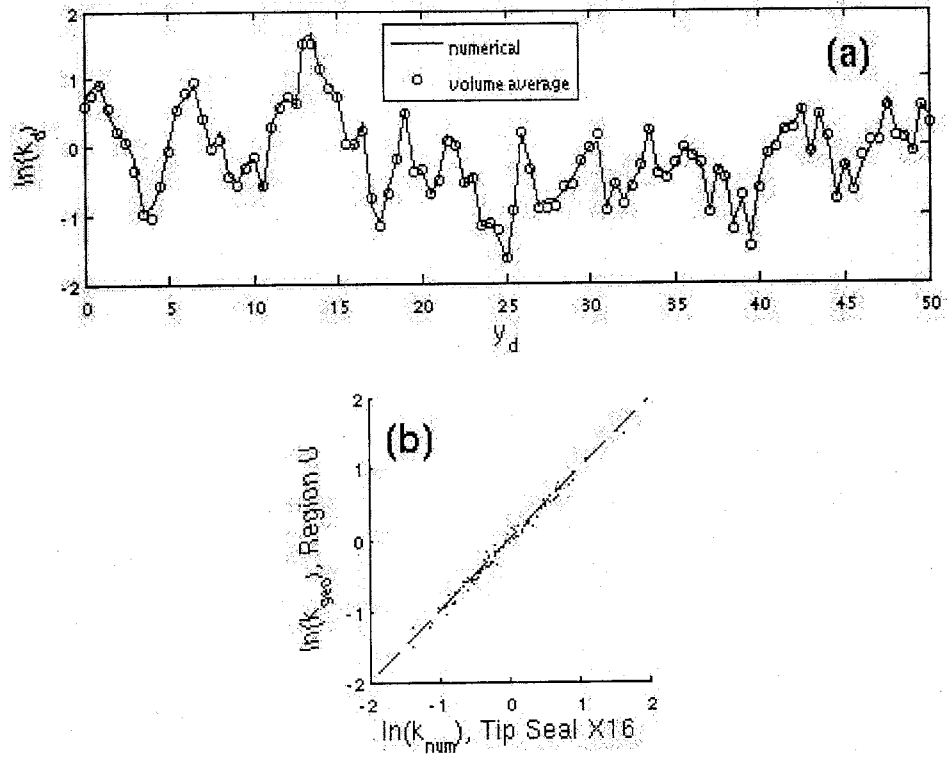
Figure 3.17: (a), Comparison between $\ln\left(k_{16,num}\right)$ and $\ln\left(k_{U16}\right)$. (b), Scatter plot of $\ln\left(k_{U16}\right)$ vs. $\ln\left(k_{16,num}\right)$.
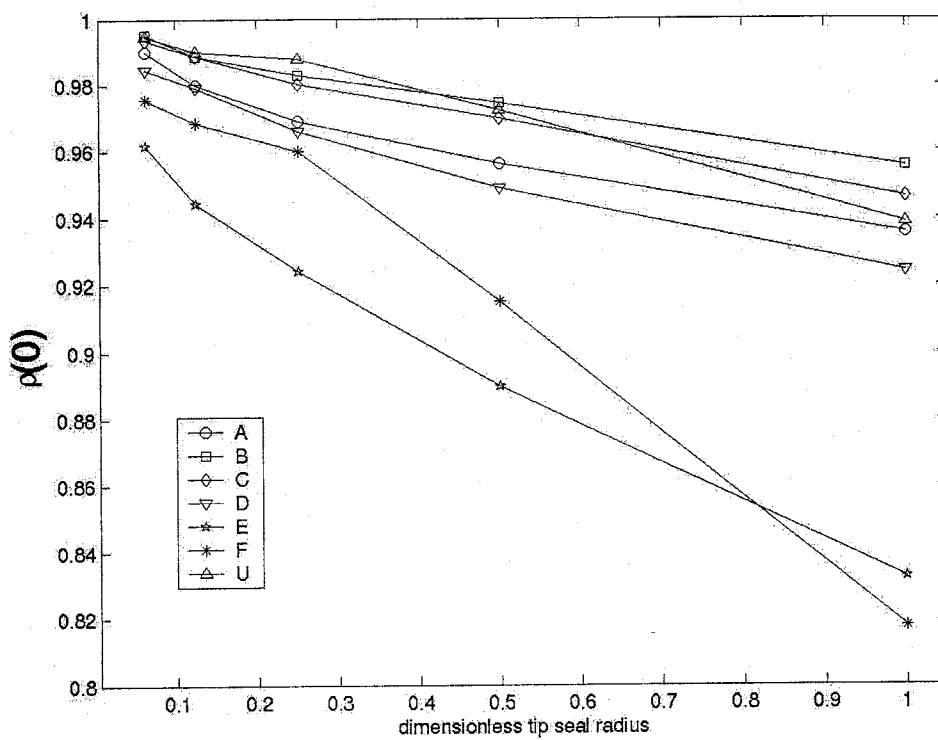
Figure 3.18: Correlation coefficient upscaling

that the minpermeameter acts as an averaging device, weighting the domain nearest the edges of the tip seal (particularly the inner tip-seal) most heavily. At the same time, we are calculating the geometric mean within subregions of the domain, but without giving greater weight to any part of the subregion. Thus, the volume average always gives disproportionate weight to portions of the domain removed from those portions that truly contribute to the effective permeability. When the correlation length is approximately the same size as the inner tip seal radius, the underlying permeability field is more uniform in the neighborhood of the tip-seal, so the greater weight given by the volume geometric averaging to portions of the domain removed from the tip-seal edges has little effect. However, as the correlation length decreases relative to the inner tip-seal radius, the underlying permeability field becomes less uniform, and the volume geometric mean includes values that are increasingly dissimilar to those near the tip-seal edges. This has the effect moving the log geometric mean away from the effective log permeability.

We plot the upscaling trends of the natural log of the geometric mean in Fig. (3.19). Comparing to Fig. (3.4a), the natural log of the geometric mean in regions A–D and U show an upward trend, as we would expect. The overall change in permeability is similar, though the volume-averaged lines do not increase monotonically, as the numerical line does. An interesting feature is that $m[\ln(k_{geo})]$ is biased low compared to the numerical values. The magnitude of the upscaling is comparable to that of log numerical effective permeability, on the order of 0.1.
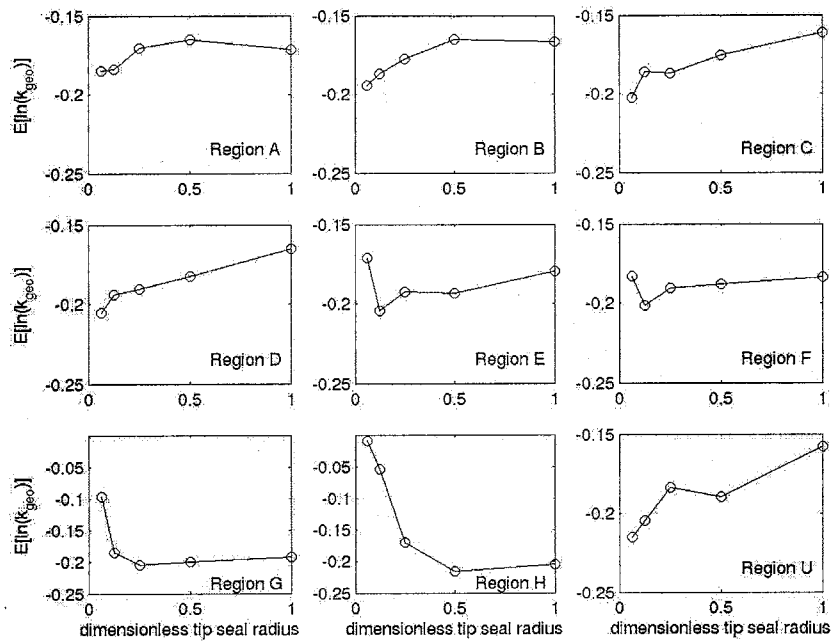
Figure 3.19: Upscaling trends in $m[\ln(k_{geometric})]$

CHAPTER 4

CONCLUSIONS AND RECOMMENDATIONS

4.1 Conclusions

From the performance of the numerical model, we are able to draw the following conclusions. We distinguish two categories, permeability simulation and measurement of the effective numerical permeability.

From the exercise of simulating the synthetic permeability field, we conclude that:

- Sequential Gaussian simulation alone is inadequate to faithfully reproduce the global characteristics of the laboratory sample. Though the semivariogram of the synthetic log permeability matches that of the laboratory sample, it is clear that this is insufficient to guarantee a qualitative match.

- Small-scale properties of the laboratory sample, if they exist, are not captured by the laboratory measurements nor replicated in the synthetic sample. We draw this conclusion based on the resolution of the measurement grid (see below). We speculate that these small-scale structures play a role in determining the effective permeability and thus influence upscaling of the mean log effective permeability. In order to test this hypothesis, it would be necessary to prescribe a small-scale structure and

90

demonstrate the desired upscaling pattern. The primary obstacle to this is creating a model with sufficient grid resolution to support a smaller scale. If this were possible, we might guess at the small-scale structure and test for upscaling. Guessing would be required because we are unable to measure the small-scale variation directly. We might, however, use optical images or x-ray tomography reconstruction of the pore space to constrain our guesses to semivariogram models that are likely representative of the true small-scale structures.

From the set of measurements by the numerical minpermeameter, we conclude that:

- Estimates of spatial structures calculated from gridded measurements are subject to preferential filtering. This filtering limits how well structures of the measured field can be resolved as a function of both the measurement scale (the scale of the instrument) and the sample scale (the scale of the measurement grid). It has already been established that it is not possible to resolve structures below either the measurement scale or the sample scale [Beckie, 1996]. In this case, the sample scale was held constant and the measurement scale varied. As predicted, the numerical minipermeameter does filter out the contribution of structures with correlation lengths on the order of the inner tip seal radius. We also determined that in order to completely resolve spatial structures at the theoretical limit of the sample scale, the measurement scale must be two orders of magnitude smaller than the correlation length. At this point, this result can only be generalized for gas minipermeameters with $b_d = 2$.

- We confirm that the gas minipermeameter measurement is strongly correlated to the geometric mean of the underlying permeability field. In particular, the measurement correlates best with those small (i. e., $r_d \leq \sqrt{2}, h_d \leq \sqrt{2}$) cylindrical regions that encompass the annular region lying beneath the inner radius of the tip-seal. This confirms that the spatial weighting function derived by Aronson [2000] and Molz, et al. [2003] for homogeneous fields is valid for heterogeneous fields.

Beyond these largely performance related conclusions, we must yet address the physical processes that contribute to permeability upscaling. What, then, have we learned, in a general sense, about upscaling? Answering this question requires us to explore the implications of the negative result of the numerical experiment.

The physical explanation for the lack of mean effective log permeability is that the synthetic permeability field does not allow for increased relative flow (on average) as tip seal size increases. As discussed in §3.1, this is probably due to an absence of preferential flow paths. It appears that the numerical scheme provides an accurate model of minipermeameter operation, and the magnification routine gives a good account of modeling the change of scale, which leaves the permeability simulation routine accountable for the negative result.

We attribute this failure to three things. First, an inability of the laboratory measurements to fully characterize the Massillon sandstone, particularly the small-scale structures. This may be indicative of the closure problem discussed by Beckie [1996]. Beckie notes that parameters cannot vary

below twice the measurement scale (in this case the inner tip-seal radius), nor can parameters be explicitly resolved below twice the grid scale (the factor of two is consequence of these limits being functions of the Sampling Theorem [Bracewell, 2001]). While the measurement scale measurement scale for the laboratory data on which we based the simulation is 0.15 cm, allowing structures as small as 0.30 cm to be resolved in theory, the grid scale is 1.27 cm. This means that structures with a correlation length less than 2.54 cm cannot be completely resolved. Visual inspection of the Massillon shows structures below this scale, making it plausible that permeability structures also exist here.

Second, semivariograms and distributions of the synthetic log permeability are not well matched to those of the laboratory sample. In particular both the synthetic log permeability and the effective log permeability show long range upward trends, denoting lower correlation at long lags, that are not present in the laboratory data. Also, the distribution of the laboratory log permeability is significantly skewed, showing a extended tail of low log permeability values and a truncated tail of high log permeability values. Both these characteristics stand to have a significant bearing on the numerical measurements.

Third, the synthetic field is qualitatively much different from the laboratory specimen. Absent from the synthetic field are the bounding surfaces that separate zones of depositionally related cross-strata. As observed by Tidwell and Wilson [2000], the statistics of the cross-strata are representative of separate population parameters from those of the bounding surfaces, with the bounding regions contributing the negative skew of the distribution. This bi-

modality is not reflected in the synthetic log permeability. The stratified structure of the laboratory Massillon almost certainly contributes to the upscaling of the mean log permeability.

Without capturing these characteristic structures of the laboratory specimen, it is unlikely that we could expect to replicate the same upscaling pattern in the numerical experiment.

4.2   Recommendations for Future Work

Our recommendations for future work parallel the concluding points made above.

- Simulating values at a significantly smaller scale than that used herein would prove technically challenging. Decreasing grid spacing by a factor of 10 would require storing permeability values for no less than 7.88×10^9 grid points. Using single-precision format, storing the coefficient matrix, state vector and load vector would require about 176GB. With 64-bit processors entering wide commercial distribution, it might, in theory, be possible to solve this system on a desktop machine. However, the time required to do so might make doing so prohibitive.

  Setting aside for the moment the technical issues, decreasing the grid resolution would also require knowledge of the small-scale correlation structure. The finest grid separation used in the current study is on the order of 10^{-1}mm or $10^2 \mu$m. Decreasing this by a factor of 10 would require knowledge of the correlation structure at the micron scale. Chapin [2001] has analyzed the pore structure of the Massillon sandstone, which is at

the desired scale, and calculated spatial correlation using spectral analysis. Should computational limitations prove surmountable, future workers might attempt to derive effective permeability values from Chapin's pore scale analysis, and thence prescribe smaller scale semivariograms.

- Tidwell and Wilson [2000] fit a standard nested semivariogram structure to their data. This nested structure was the best fit using the standard functional forms available to model semivariograms. However, this functional form did not provide a faithful replica of the Massillon semivariogram during simulation. Better fidelity might be achieved by using a look-up table composed of the empirical covariances in place of covariances derived from the nested function that was fit to the data. However, care would have to be taken to ensure that the empirical covariance matrix would be non-negative definite.

- The physical characteristic of the Massillon might better be replicated in the synthetic log permeability by incorporating several approaches to simulation. Recall that the Massillon is characterized by the presence of several bounding surfaces, representing unconformities separating different depositional events. In addition, the laboratory data indicate that the permeability does not follow a log-normal distribution. Performing a normal score back-transform of the Gaussian distributed simulated log permeabilities, using a transformation table based on the laboratory log permeabilities, would a necessary step in future work. Better fidelity still might be achieved by conditioning the simulation on the laboratory data. This would require first performing a forward normal score trans-

form, followed by simulation, followed by back-transformation. A related approach to reproducing the pattern of depositionally related regions separated by bounding surfaces would be to use an indicator algorithm, follow by punctual simulation within each indicator region. Doing so would more accurately take into account the weak bimodality of the population. This approach, too, could be conditioned on the laboratory data set.

- The magnification routine was based on a sampling upscaling rule: the punctual permeability value at the node points was passed from one magnification to the next. This means that for a given volume of the domain occupied by a single grid-block at one magnification, and several grid-blocks at a higer magnification, that no averaging takes place to incorporate information about any of the fine grid blocks into the assigned permeability of the coarse grid-block, other than for the grid-block that is co-located. It would be worthwhile to explore different averaging rules to see what effect would take place.

- It would be very helpful to increase both the physical and parameter space covered by the measurement grid. This might be accomplished by extending the measurement grid into two or three dimensions, and covering a region that encompasses many correlation lengths. In this study, the measurement transect encompassed about seven correlation lengths of the large scale correlation structure. Ideally, subsequent studies might encompass at least fifty correlation lengths in all directions.

- A Monte Carlo approach would be complementary or supplementary to extending the measurement grid. Replicating the numerical experiment

using multiple realizations of the synthetic permeability field provides a more thorough exploration of the parameter space, giving assurance that the results are general and not a fluke of a single permeability field. might be taken, in which a two-dimensional grid of similar size to the transect used here would be generated for many independent realizations.

- A useful test of upscaling volumes corresponding to minipermeameter measurements would be to subject each of the volume averages to linear flow conditions. Using cubical rather than cylindrical volumes would be a natural choice. Each sub-volume would simply be subjected to linear flow in each of the principal directions, giving effective permeability values that would be consistent with the sort of conditions encountered in most typical applications. Optimally, these linear conditions would be tested using several different boundary conditions: no flow, prescribed potential and periodic, reflecting a variety of possible modeling scenarios.

- It would be of great interest to visualize flow through the synthetic samples. Such visualization could include stream lines and stream tubes to identify preferential flow paths, which would help to ascertain the physical reasons for permeability upscaling. In addition, use of a particle tracker would expand the scope of the work to include dispersivity upscaling.

APPENDIX A

Finite-Difference Method

We model the operation of the minipermeameter using a block-centered, finite-difference scheme. The domain is discretized into $N_x \times N_y \times N_z$ rectangular grid-blocks. grid-block are identified by the indices ix, iy, and iz, corresponding to relative position along the x, y, and z axes, respectively. Material properties within each grid-block are assumed to homogeneous and the state variable Φ is evaluated at a grid point at the center of each block.

We may derive a system of equations for Φ at each grid point based on a simple material balance argument (note that this derivation leads to exactly the same system of equations as the more conventional derivation based on Taylor series expansion of the differential operator.)

Let's proceed by considering a simple example, a 3×2 two-dimensional grid (Fig. 2.1). Physically, the figure represents a rectangular block with no flow boundaries at the top and bottom (indicated by hash marks) and prescribed potentials, Φ_A and Φ_B on the left and right sides, respectively. The coordinate system of the model is defined in the lower left corner of the figure. We denote the width of the blocks as h_x, their height as h_y, and their thickness as b. Model grid points are indicated by black dots. The ix and iy indices are displayed at the top right of each grid-block. Assume the grid-blocks have a thickness b. Displayed at the bottom right of each grid-block is the global index l, calculated
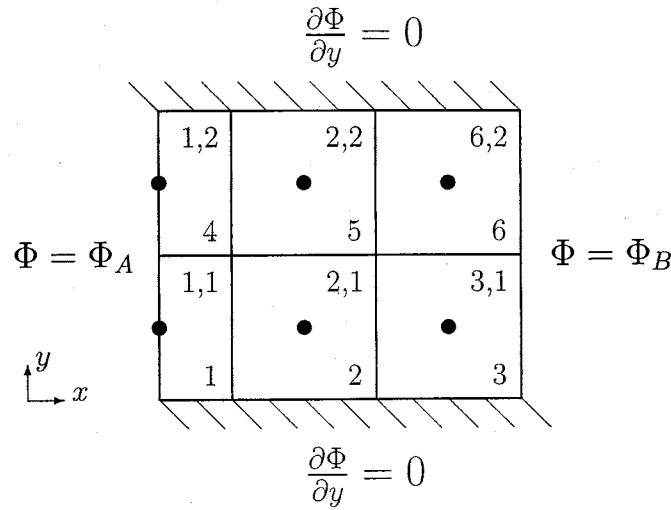
Figure A.1: A simple 3×2 grid

$$l = ix + (iy - 1)N_x \tag{A.1}$$

This global index allows us to label grid-blocks with a single number, which will prove to be convenient when putting the system of equations into matrix-vector form. Notice that the leftmost grid-blocks have been "chopped", the boundary is described by a plane cutting through the center of the grid-blocks, so that the grid point lies at the surface, but the distances between grid points are uniform in each direction, $h_x = h_y = h$, consistent with the grid layout used in this work. The derivation that follows [Wilson, personal communication 2002] can easily be modified to accommodate a non-uniform grid.

Under conditions of steady-state flow, the principle of mass conservation informs us that the net mass flux through the boundaries of a control volume must be zero. If we suppose our control volume, Ω to be an arbitrary

grid-block (ix, iy), with boundary $\partial\Omega$, we can use Eq. (2.14) to express this idea as

$$\oint_{\partial\Omega} \mathbf{q}_m \cdot d\mathbf{A} = 0, \tag{A.2}$$

$$\Rightarrow \oint_{\partial\Omega} -k\nabla\Phi \cdot d\mathbf{A} = 0. \tag{A.3}$$

Assuming that grid-blocks are connected through block faces, so that block (ix, iy) is connected only to blocks $(ix - 1, iy)$, $(ix, iy - 1)$, $(ix + 1, iy)$, and $(ix, iy + 1)$, we can approximate Eq. (A.3) for an interior grid-block (that is, a grid-block that does not lie on the boundary of the domain) with a system of one-sided difference equations (we have suppressed the subscript m, though we maintain that $\mathbf{q}$ means the mass flux).

$$\oint_{\partial\Omega} \mathbf{q} \cdot d\mathbf{A} \approx$$

$$-\mathbf{q}_{ix-\frac{1}{2},iy}\, h_y b + \mathbf{q}_{ix+\frac{1}{2},iy}\, h_y b + -\mathbf{q}_{ix,iy-\frac{1}{2}}\, h_x b + \mathbf{q}_{ix,iy+\frac{1}{2}}\, h_x b \tag{A.4}$$

$$= k_{ix-\frac{1}{2},iy}\Big(\frac{\Phi_{ix,iy} - \Phi_{ix-1,iy}}{h_x}\Big)h_y b$$

$$- k_{ix+\frac{1}{2},iy}\Big(\frac{\Phi_{ix+1,iy} - \Phi_{ix,iy}}{h_x}\Big)h_y b$$

$$+ k_{ix,iy-\frac{1}{2}}\Big(\frac{\Phi_{ix,iy} - \Phi_{ix,iy-1}}{h_y}\Big)h_x b$$

$$- k_{ix,iy+\frac{1}{2}}\Big(\frac{\Phi_{ix,iy+1} - \Phi_{ix,iy}}{h_y}\Big)h_x b \tag{A.5}$$

where $\mathbf{q}_{ix-\frac{1}{2},iy}$ is the mass flux across the interface between grid-block (ix, iy) and grid-block $(ix - 1, iy)$. Similarly, $\mathbf{q}_{ix+\frac{1}{2},iy}$, $\mathbf{q}_{ix,iy-\frac{1}{2}}$, and $\mathbf{q}_{ix,iy+\frac{1}{2}}$ are the

100

fluxes between grid-block (ix, iy) and, respectively, $(ix + \frac{1}{2}, iy)$, $(ix, iy - \frac{1}{2})$, and $(ix, iy + \frac{1}{2})$. The permeabilities are effective values between grid-blocks, designated using the same convention (for example, $k_{ix+\frac{1}{2},iy}$ is the effective interblock permeability between blocks (ix, iy) and $(ix + \frac{1}{2}, iy)$). We use the harmonic mean for the interblock permeability,

$$k_{ix-\frac{1}{2},iy} = \frac{2}{\frac{1}{k_{ix,iy}} + \frac{1}{k_{ix-\frac{1}{2},iy}}} \tag{A.6}$$

$$k_{ix+\frac{1}{2},iy} = \frac{2}{\frac{1}{k_{ix+\frac{1}{2},iy}} + \frac{1}{k_{ix,iy}}} \tag{A.7}$$

$$k_{ix,iy-\frac{1}{2}} = \frac{2}{\frac{1}{k_{ix,iy}} + \frac{1}{k_{ix,iy-\frac{1}{2}}}} \tag{A.8}$$

$$k_{ix,iy+\frac{1}{2}} = \frac{2}{\frac{1}{k_{ix,iy+\frac{1}{2}}} + \frac{1}{k_{ix,iy}}} \tag{A.9}$$

These equations are valid for *interior* grid-blocks, but what about grid-blocks that lie on the boundaries of the domain? Prescribed flux boundary conditions (a.k.a. second type or Neumann) are handled easily by direct substitution into Eq. (2.31). For example, later on we will be required to set a no-flow boundary condition on a chopped block. To do so means literally doing nothing: the appropriate flux term in the equation corresponding to Eq. (2,31) is zero, so it does no appear at all thereafter. Prescribed potential boundary conditions (a.k.a. first type or Dirichlet) are handled in a couple of different ways. For a chopped block, such as the left boundary in Fig. 2.1, the boundary condition is applied directly to the grid point so the solution is trivial—$\Phi_{ix,iy}$ is simply the boundary condition! For a full block, such as the right boundary

in Fig. 2.1, the boundary condition is applied to the side of the grid-block. We make use of the same one-sided difference equation we used to calculate fluxes between grid-blocks. For example, the mass flux across the right surface of one of grid-block (3,1) in Fig. 2.1 is given by,

$$\mathbf{q}_{3,1} = -k_{3,1}\frac{\Phi_B - \Phi_{3,1}}{h_x/2}\hat{\mathbf{e}}_x \qquad (A.10)$$

For those who may feel squeamish at this point, asserting that the flux given by Eq. (A.10) should correctly be assigned to a surface that lies halfway between the side of the grid-block and the grid point, be reassured that this is the same result obtained from the more conventional derivation by assigning a layer of fictitious grid-blocks on the boundary.

Using this approach, we obtain a system of six equations and six unknowns. At this point, we begin labeling Φ using the global index l.

$$\Phi_1 = \Phi_A, \qquad (A.11)$$

$$k_{1.5,1}\left(\frac{\Phi_2 - \Phi_1}{h_x}\right)h_y b - k_{2.5,1}\left(\frac{\Phi_3 - \Phi_2}{h_x}\right)h_y b - k_{2,1.5}\left(\frac{\Phi_5 - \Phi_2}{h_y}\right)h_x b = 0, \quad (A.12)$$

$$k_{2.5,1}\left(\frac{\Phi_3 - \Phi_2}{h_x}\right)h_y b - k_{3,1}\left(\frac{\Phi_B - \Phi_3}{h_x/2}\right)h_x b - k_{3,1.5}\left(\frac{\Phi_6 - \Phi_3}{h_y}\right)h_x b = 0, \quad (A.13)$$

$$\Phi_4 = \Phi_A, \qquad (A.14)$$

$$k_{1.5,2}\left(\frac{\Phi_5 - \Phi_4}{h_x}\right)h_y b - k_{2.5,2}\left(\frac{\Phi_6 - \Phi_5}{h_x}\right)h_y b - k_{2,1.5}\left(\frac{\Phi_5 - \Phi_2}{h_y}\right)h_x b = 0, \quad (A.15)$$

$$k_{2.5,2}\left(\frac{\Phi_6 - \Phi_5}{h_x}\right)h_y b - k_{3,2}\left(\frac{\Phi_B - \Phi_6}{h_x/2}\right)h_x b - k_{3,1.5}\left(\frac{\Phi_6 - \Phi_3}{h_y}\right)h_x b = 0. \quad (A.16)$$

We can rearrange Eq. (A.11) – Eq. (A.16), as

$$\Phi_1 = \Phi_A \qquad (A.17)$$

$$k_{1.5,1}\frac{h_y b}{h_x}\Phi_1 + (k_{1.5,1}\frac{h_y b}{h_x} + k_{2.5,1}\frac{h_y b}{h_x} + k_{2,1.5}\frac{h_x b}{h_y})\Phi_2$$
$$- k_{2.5,1}\frac{h_y b}{h_x}\Phi_3 - k_{2,1.5}\frac{h_x b}{h_y}\Phi_5 \;=\; 0 \qquad (A.18)$$

$$-k_{2.5,1}\frac{h_y b}{h_x}\Phi_2$$
$$+ (k_{2.5,1}\frac{h_y b}{h_x} + 2k_{3,1}\frac{h_y b}{h_x} + k_{3,1.5}\frac{h_x b}{h_y})\Phi_3$$
$$- k_{3,1.5}\frac{h_x b}{h_y}\Phi_6 \;=\; 2k_{3,1}\frac{h_y b}{h_x}\Phi_B \qquad (A.19)$$

$$\Phi_4 = \Phi_A \qquad (A.20)$$

$$-k_{2,1.5}\frac{h_x b}{h_y}\Phi_2 - k_{1.5,2}\frac{h_y b}{h_x}\Phi_4$$
$$+ (k_{1.5,2}\frac{h_y b}{h_x} + k_{2.5,2}\frac{h_y b}{h_x} + k_{2,1.5}\frac{h_x b}{h_y})\Phi_5 - k_{2.5,2}\frac{h_y b}{h_x}\Phi_6 \;=\; 0 \qquad (A.21)$$

$$-k_{3,1.5}\frac{h_x b}{h_y}\Phi_3 - k_{2.5,2}\frac{h_y b}{h_x}\Phi_5$$
$$+(k_{2.5,2}\frac{h_y b}{h_x} + 2k_{3,2}\frac{h_y b}{h_x} + k_{3,1.5}\frac{h_x b}{h_y})\Phi_6 \;=\; 2k_{3,2}\frac{h_y b}{h_x}\Phi_B \qquad (A.22)$$

This linear system of equations can be written in matrix vector form

$$A\mathbf{\Phi} = \mathbf{f}. \qquad (A.23)$$

The coefficient matrix A is,

$$A = \begin{pmatrix} 1 & 0 & 0 & 0 & 0 & 0 \\ -T_{1.5,1} & \begin{matrix} T_{1.5,1}+T_{2.5,1} \\ +T_{2,1.5} \end{matrix} & -T_{2.5,1} & 0 & -T_{2,1.5} & 0 \\ 0 & -T_{2.5,1} & \begin{matrix} T_{2.5,1}+2T_{3,1} \\ +T_{3,1.5} \end{matrix} & 0 & 0 & -T_{3,1.5} \\ 0 & 0 & 0 & 1 & 0 & 0 \\ 0 & -T_{2,1.5} & 0 & -T_{1.5,2} & \begin{matrix} T_{1.5,2}+T_{2.5,2} \\ +T_{2,1.5} \end{matrix} & -T_{2.5,2} \\ 0 & 0 & -T_{3,1.5} & 0 & -T_{2.5,2} & \begin{matrix} T_{2.5,2}+2T_{3,2} \\ +T_{3,1.5} \end{matrix} \end{pmatrix}, \tag{A.24}$$

where,

$$T_{ix+\frac{1}{2},iy} \equiv k_{ix+\frac{1}{2},iy}\frac{h_y b}{h_x}, \tag{A.25}$$

$$T_{ix,iy+\frac{1}{2}} \equiv k_{ix,iy+\frac{1}{2}}\frac{h_x b}{h_y}. \tag{A.26}$$

The state vector, $\boldsymbol{\Phi}$, is

$$\boldsymbol{\Phi} = \begin{bmatrix} \Phi_1 \\ \Phi_2 \\ \Phi_3 \\ \Phi_4 \\ \Phi_5 \\ \Phi_6 \end{bmatrix}, \tag{A.27}$$

and the load vector, $\mathbf{f}$, is

$$\mathbf{f} = \begin{bmatrix} \Phi_A \\ 0 \\ 2k_{3,1}\frac{h_y b}{h_x}\Phi_B \\ \Phi_B \\ 0 \\ 2k_{3,2}\frac{h_y b}{h_x}\Phi_B \end{bmatrix}. \tag{A.28}$$

104

The coefficient matrix A represents the connections between blocks, the state vector $\boldsymbol{\Phi}$ contains the potential at each grid point, and the load vector $\mathbf{f}$ contains information about sources, sinks and boundary conditions. The coefficient matrix A is pentadiagonal, in that there exist non-zero entries exist only for $a_{n,n}$, $a_{n,n\pm1}$, and $a_{n,n\pm N_x}$, and symmetric. The $a_{n,n}$ entries correspond to the grid-block with global index $l = n$. The $a_{n,n\pm1}$ entries represent the connection between adjacent grid blocks in the x direction, the $a_{n,n\pm N_x}$ represent the connection between adjacent grid-blocks in the y direction. Our objective is to solve Eq. (A.23), which for this system we could easily do even by hand using Gaussian elimination.

We can easily generalize the equations derived above for a three-dimensional system. Construction of the coefficient matrix A and load vector $\mathbf{f}$ can be prescribed by an algorithm whereby we visit each grid-block in the domain in turn, assigning elements in A and $\mathbf{f}$ on the basis of connection to neighboring blocks and boundary conditions. For an arbitrary grid-block (ix, iy, iz) with global index l, the assignments are given as follows:

- If one of the faces of grid-block l is a chopped block boundary with a prescribed potential Φ_0, then

$$a_{l,l} = 1 \tag{A.29}$$

$$b_l = \Phi_0 \tag{A.30}$$

In this case, we go no farther. Nothing more need be done, so we move onto the next grid-block.

- If grid-block l does not lie on a chopped block, then A and b depend on the connections of block l to either its neighbors or the boundaries. Note that the elements of the main diagonal of A and of b receive input from connections through all six faces of block l. We describe this below by updating these entries, adding new values to the old as we calculate them.

    - Let's begin with the connection between an arbitrary grid-block (l) and its horizontal neighbors. The connection is maintained through the opposing faces of the block with area given by $h_y h_z$. We define the "left" face as the interface between blocks (l) and ($l-1$) (or equivalently between (ix,iy,iz) and ($ix-1,iy,iz$)) and the "right" face as the interface between blocks (l) and ($l+1$) (i. e., between (ix,iy,iz) and ($ix+1,iy,iz$)). There are three possibilities: the interface may be a side-of-grid-block first type boundary condition, it may be a second type boundary condition, or it may neighbor another grid-block.

        1. If either the face is a side-of-grid-block boundary with prescribed potential Φ_0, then

        $$a_{l,l} = 2k_{ix,iy,iz}\frac{h_y h_z}{h_x} \tag{A.31}$$

        $$f_l = 2k_{ix,iy,iz}\frac{h_y h_z}{h_x}\Phi_0 \tag{A.32}$$

        2. If either the left or right face is a boundary with a prescribed mass flux, $\mathbf{q}_0$, then we do nothing to A, but we update $\mathbf{f}$ with

        $$f_l = \pm\mathbf{q}_0 \cdot \hat{\mathbf{e}}_x h_y h_z + f_{l,old} \tag{A.33}$$

106

The normal vectors point out from the grid-block, so an inward flux is negative and and outward flux is positive. Note that if the boundary is no-flow, then both A and $\mathbf{f}$ are unchanged, hence the appellation on a no-flow boundary as a "natural" boundary condition.

3. If the left face neighbors another grid-block, then

$$a_{l,l} = k_{ix-\frac{1}{2},iy,iz}\frac{h_y h_z}{h_x} + a_{l,l;old} \tag{A.34}$$

$$a_{l,l-1} = -k_{ix-\frac{1}{2},iy,iz}\frac{h_y h_z}{h_x} \tag{A.35}$$

If the right face abuts another grid-block, then

$$a_{l,l} = k_{ix+\frac{1}{2},iy,iz}\frac{h_y h_z}{h_x} + a_{l,l;old} \tag{A.36}$$

$$a_{l,l+1} = -k_{ix+\frac{1}{2},iy,iz}\frac{h_y h_z}{h_x} \tag{A.37}$$

In neither case is $\mathbf{f}$ affected.

– The connection between arbitrary grid-block (l) and its front and back neighbors is maintained through the opposing faces of the block with area given by $h_x h_z$. We define the "front" face as the interface between blocks (l) and ($l - N_x$) (or equivalently between (ix,iy,iz) and ($ix,iy - 1,iz$)) and the "back" face as the interface between blocks (l) and ($l + N_x$) (i. e., between (ix,iy,iz) and ($ix,iy + 1,iz$)).

1. If either face is a boundary with prescribed potential Φ_0, then we update A and $\mathbf{f}$ with

$$a_{l,l} = 2k_{ix,iy,iz}\frac{h_x h_z}{h_y} + a_{l,l;old} \tag{A.38}$$

107

$$f_l = 2k_{ix,iy,iz} \frac{h_x h_z}{h_y} \Phi_0 + f_{l,old} \qquad (A.39)$$

2. If either the front or back face is a boundary with a prescribed mass flux, $\mathbf{q}_0$ we update $\mathbf{f}$ with

$$f_l = \pm \mathbf{q}_0 \cdot \hat{\mathbf{e}}_y h_x h_z + f_{l,old} \qquad (A.40)$$

3. If the front face neighbors another grid-block, then

$$a_{l,l} = k_{ix,iy-\frac{1}{2},iz} \frac{h_x h_z}{h_y} + a_{l,l;old} \qquad (A.41)$$

$$a_{l,l-N_x} = -k_{ix,iy-\frac{1}{2},iz} \frac{h_x h_z}{h_y} \qquad (A.42)$$

If the back face neighbors another grid-block, then

$$a_{l,l} = k_{ix,iy+\frac{1}{2},iz} \frac{h_x h_z}{h_y} + a_{l,l;old} \qquad (A.43)$$

$$a_{l,l+N_x} = -k_{ix,iy+\frac{1}{2},iz} \frac{h_x h_z}{h_y} \qquad (A.44)$$

- Finally, the connection between arbitrary grid-block (l) and its top and bottom neighbors is maintained through the opposing faces of the block with area given by $h_x h_y$. We define the "top" face as the interface between blocks (l) and ($l+N_x N_y$) (or equivalently between (ix,iy,iz) and ($ix,iy,iz+1$)) and the "bottom" face as the interface between blocks (l) and ($l - N_x N_y$) (i. e., between (ix,iy,iz) and ($ix,iy,iz-1$)).

1. If either face is a boundary with prescribed potential Φ_0, then we update A and $\mathbf{f}$ with

$$a_{l,l} = 2k_{ix,iy,iz} \frac{h_x h_y}{h_z} + a_{l,l;old} \qquad (A.45)$$

108

$$f_l = 2k_{ix,iy,iz}\frac{h_x h_y}{h_z}\Phi_0 + f_{l,old} \qquad (A.46)$$

2. If either the top or bottom face is a boundary with a prescribed mass flux, $\mathbf{q}_0$, then we do nothing to A, but we update $\mathbf{f}$ with

$$f_l = \pm\mathbf{q}_0 \cdot \hat{\mathbf{e}}_z h_x h_y + f_{l,old} \qquad (A.47)$$

3. If the top face neighbors another grid-block, then

$$a_{l,l} = k_{ix,iy,iz+\frac{1}{2}}\frac{h_x h_y}{h_z} + a_{l,l;old} \qquad (A.48)$$

$$a_{l,l-N_x N_y} = -k_{ix,iy,iz+\frac{1}{2}}\frac{h_x h_y}{h_z} \qquad (A.49)$$

If the bottom face neighbors another grid-block, then

$$a_{l,l} = k_{ix,iy,iz-\frac{1}{2}}\frac{h_x h_y}{h_z} + a_{l,l;old} \qquad (A.50)$$

$$a_{l,l+N_x N_y} = -k_{ix,iy,iz-\frac{1}{2}}\frac{h_x h_y}{h_z} \qquad (A.51)$$

The $N_x N_y N_z \times N_x N_y N_z$ coefficient matrix is septa-diagonal (i. e., it has non-zero entries only on the main, $n \pm 1$, $n \pm N_x$, and $n \pm N_x N_y$ diagonals) and symmetric.

Once A and $\mathbf{f}$ have been assembled, we need only solve the system $A\Phi = \mathbf{f}$. For this work, we use a pre-conditioned conjugate gradient algorithm [Gill, Murray and Wright, 1990], a detailed description of which is beyond the scope of this paper. Suffice it to say that the conjugate gradient method is an iterative technique used to minimize the norm of the residual vector r, where $r = A\Phi - \mathbf{f}$. Convergence of the iterative process depends on properties of the matrix A, which can be dramatically improved by preconditioning.

APPENDIX B

Comparison Between Volume Averaged and Effective Numerical Natural Log Permeability
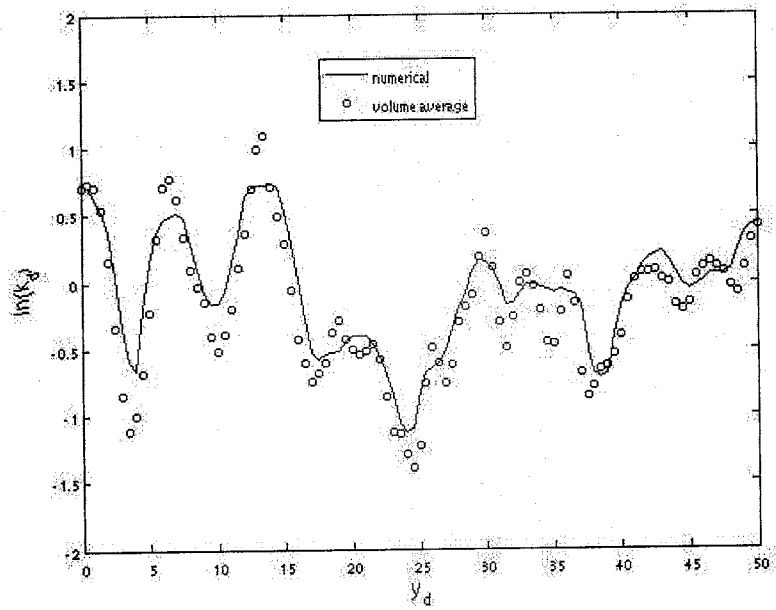
Figure B.1: Comparison between $\ln(k_{1,num})$ and $\ln(k_{A1})$.
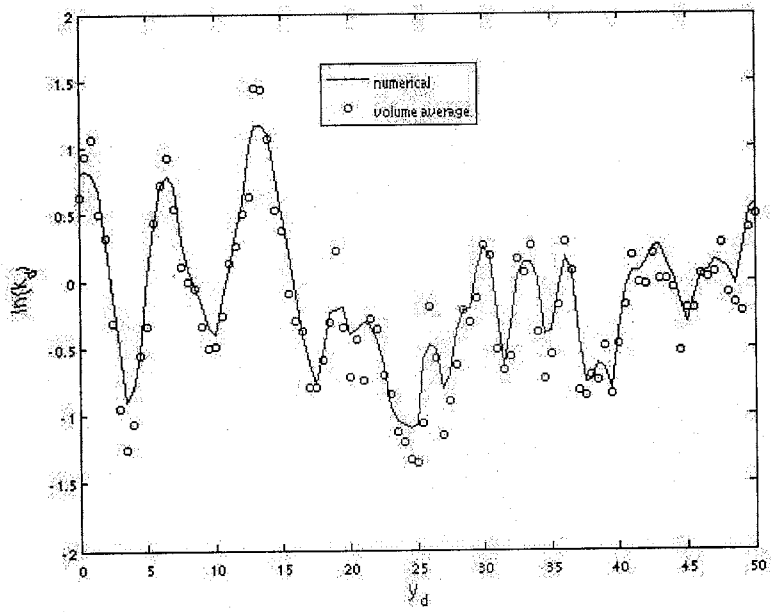
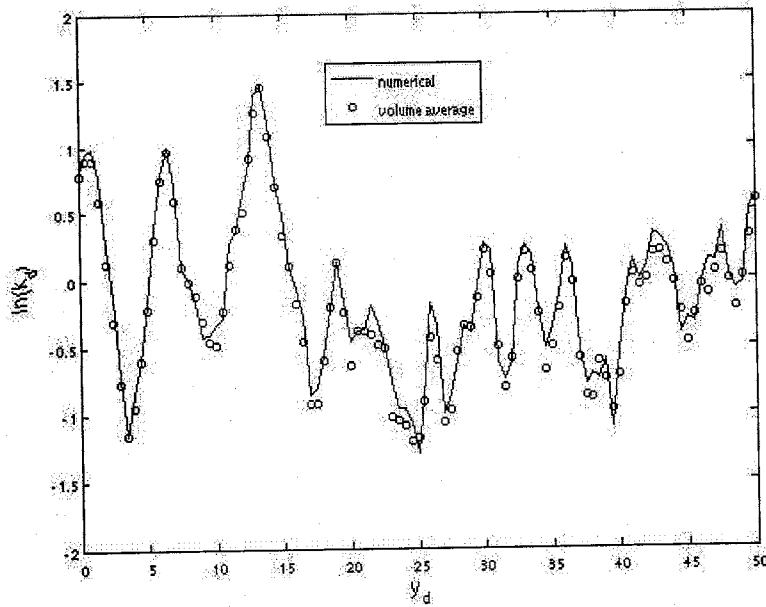Figure B.2: Comparison between $\ln\left(k_{2,num}\right)$ and $\ln\left(k_{A2}\right)$.
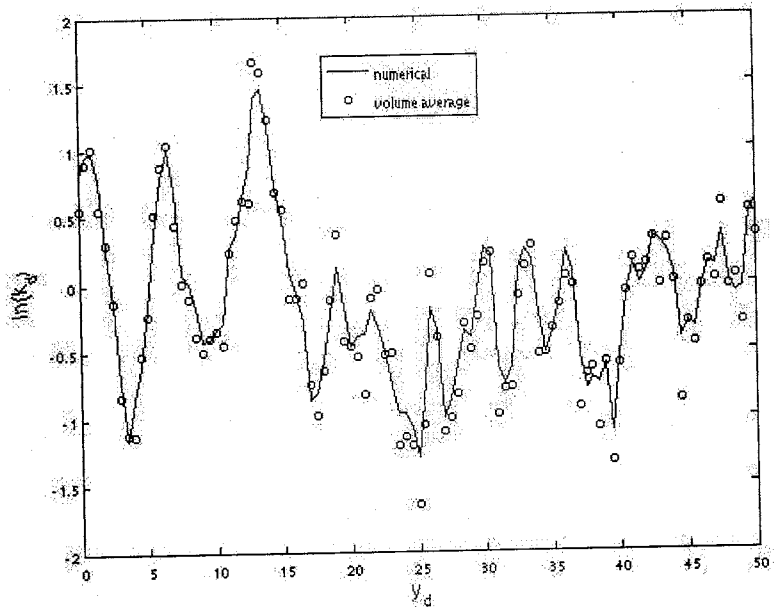
Figure B.3: Comparison between $\ln\left(k_{4,num}\right)$ and $\ln\left(k_{A4}\right)$.
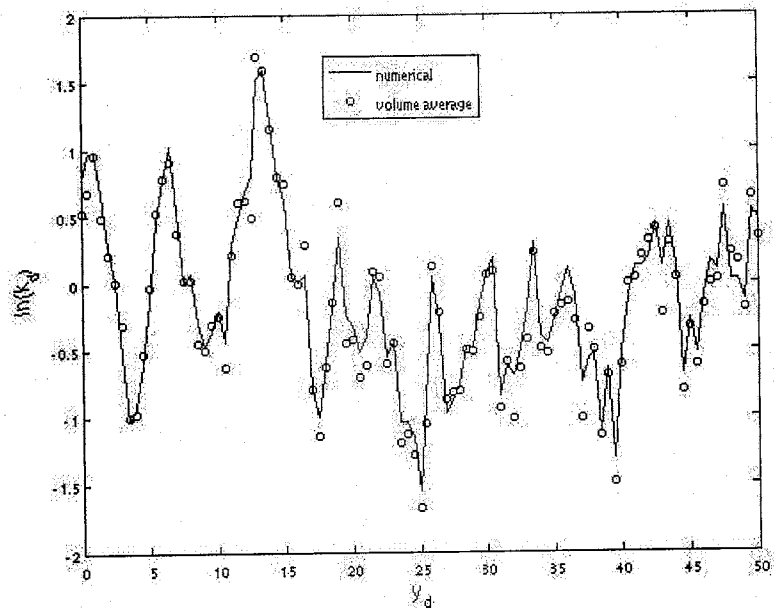
Figure B.4: Comparison between $\ln\left(k_{8,num}\right)$ and $\ln\left(k_{A8}\right)$.
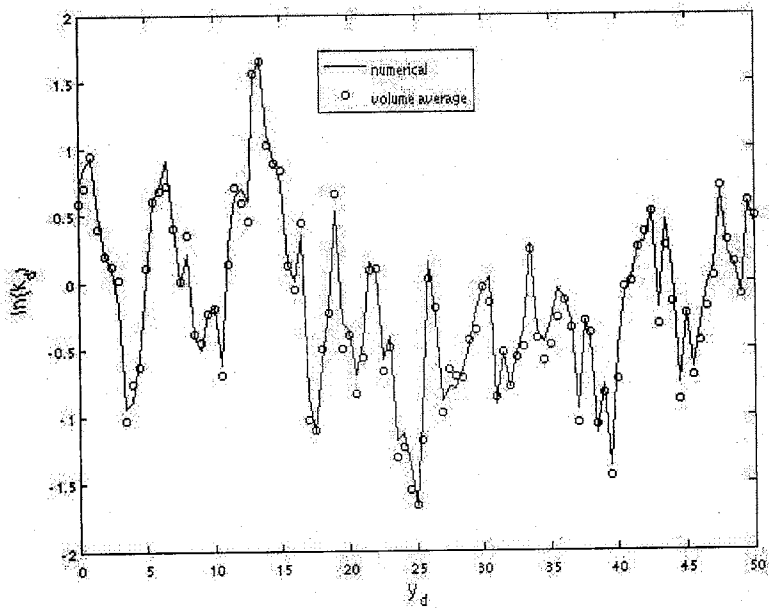
Figure B.5: Comparison between $\ln\left(k_{16,num}\right)$ and $\ln\left(k_{A16}\right)$.
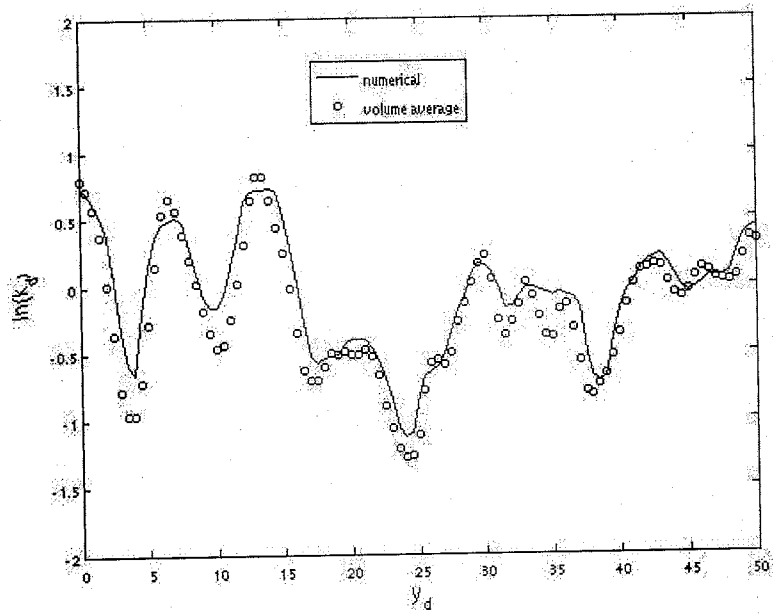
Figure B.6: Comparison between $\ln(k_{1,num})$ and $\ln(k_{B1})$.

116
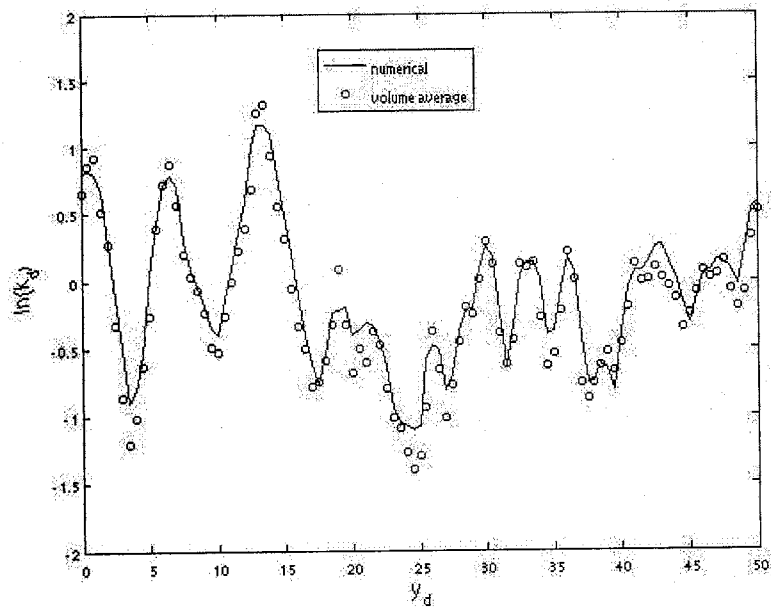
Figure B.7: Comparison between $\ln\left(k_{2,num}\right)$ and $\ln\left(k_{B2}\right)$.
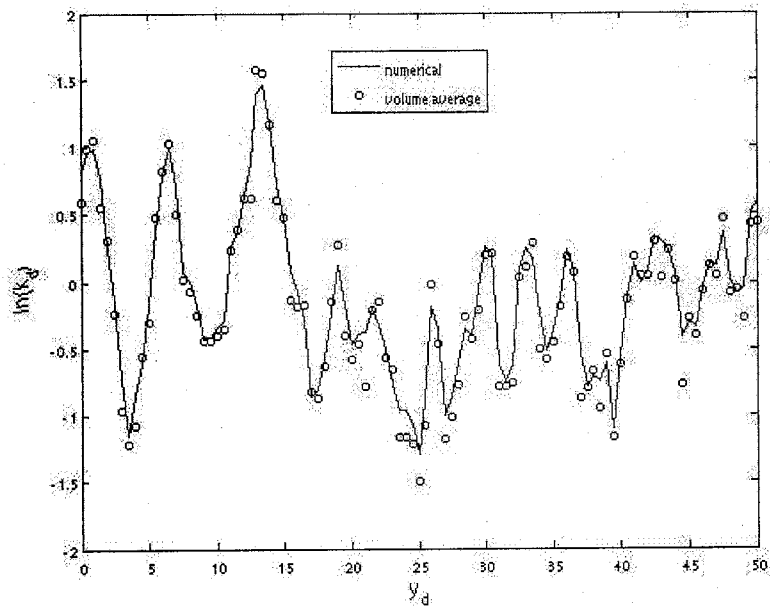
Figure B.8: Comparison between $\ln\left(k_{4,num}\right)$ and $\ln\left(k_{B4}\right)$.
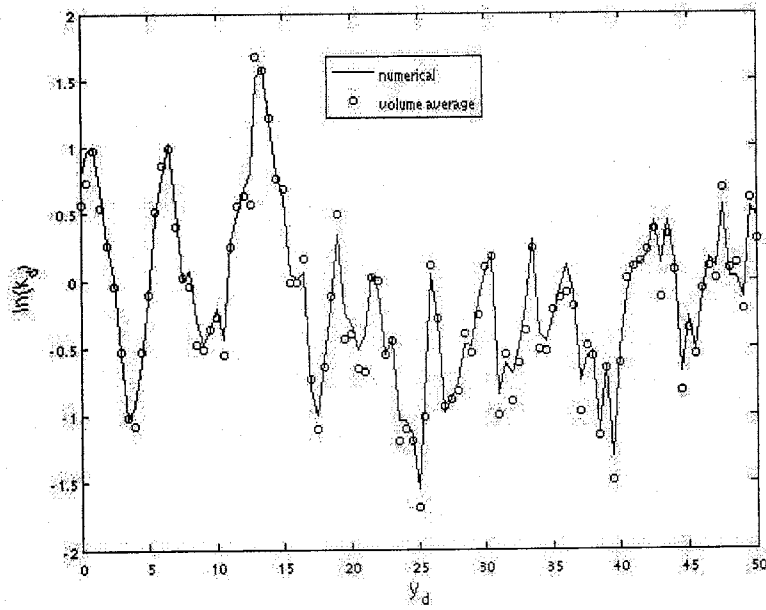
Figure B.9: Comparison between $\ln\left(k_{8,num}\right)$ and $\ln\left(k_{B8}\right)$.
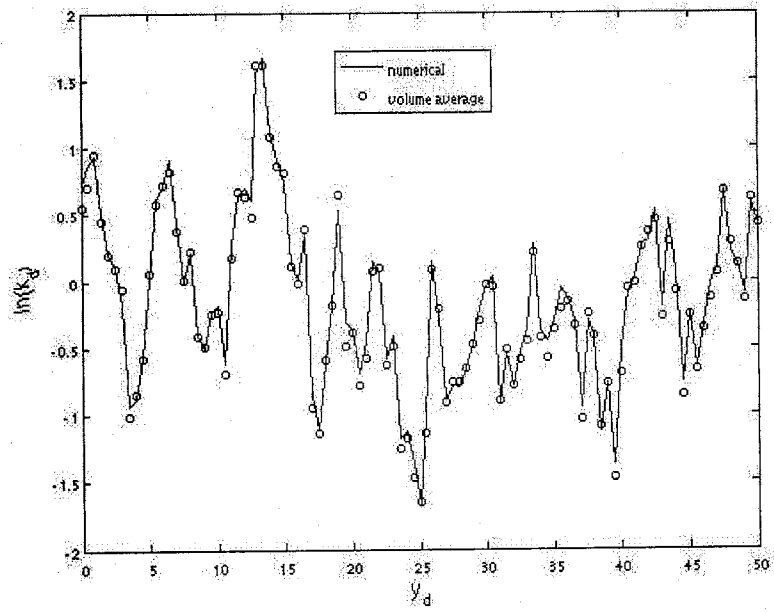
Figure B.10: Comparison between $\ln\left(k_{16,num}\right)$ and $\ln\left(k_{B16}\right)$.
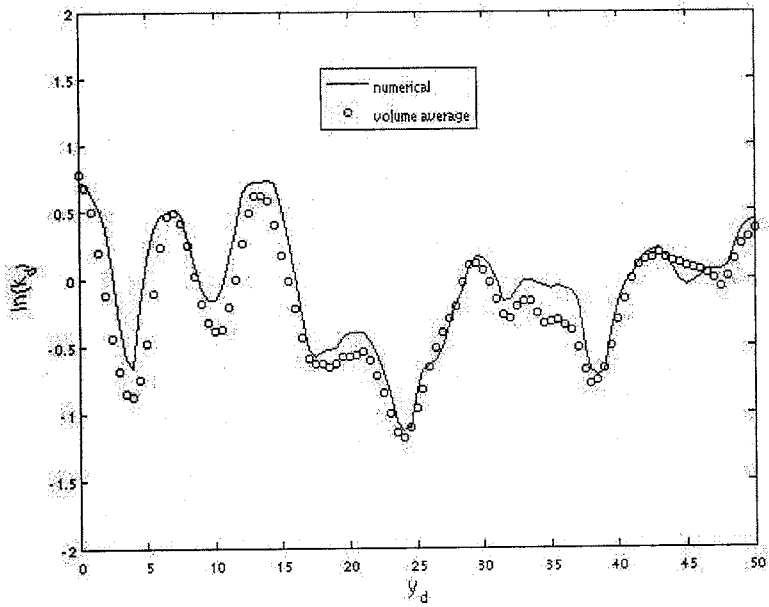
Figure B.11: Comparison between $\ln\left(k_{1,num}\right)$ and $\ln\left(k_{C1}\right)$.
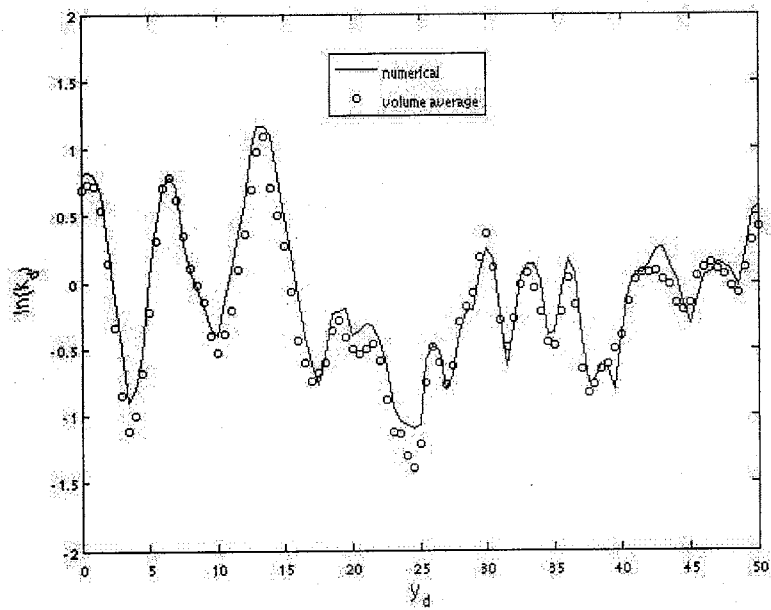
Figure B.12: Comparison between $\ln\left(k_{2,num}\right)$ and $\ln\left(k_{C2}\right)$.
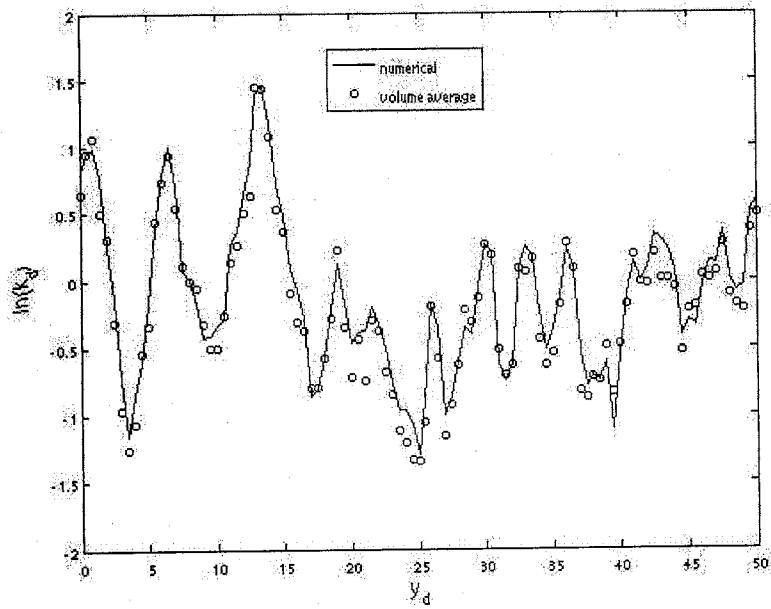
Figure B.13: Comparison between $\ln\left(k_{4,num}\right)$ and $\ln\left(k_{C4}\right)$.
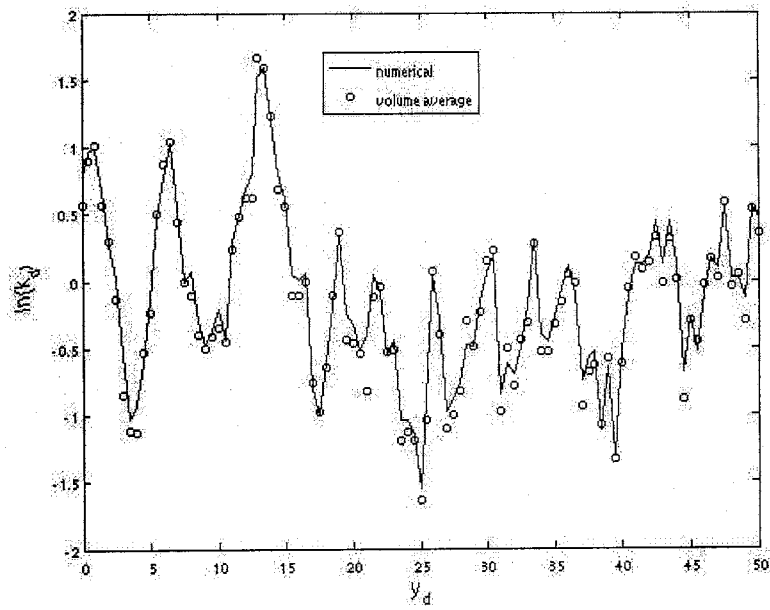
Figure B.14: Comparison between $\ln\left(k_{8,num}\right)$ and $\ln\left(k_{C8}\right)$.
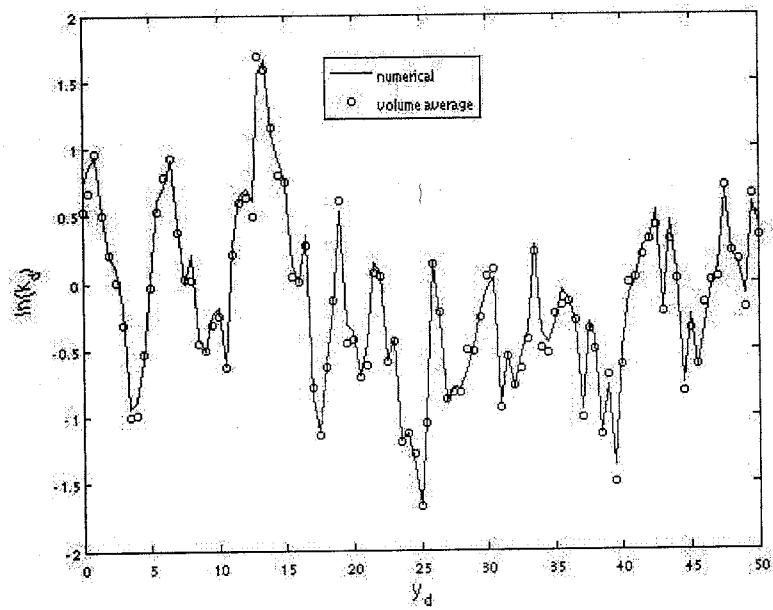
Figure B.15: Comparison between $\ln\left(k_{16,num}\right)$ and $\ln\left(k_{C16}\right)$.
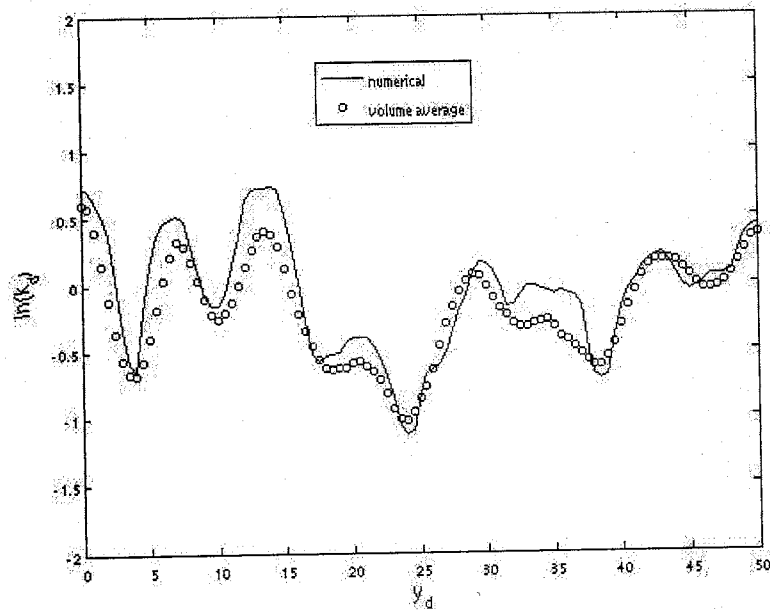
Figure B.16: Comparison between $\ln(k_{1,num})$ and $\ln(k_{D1})$.
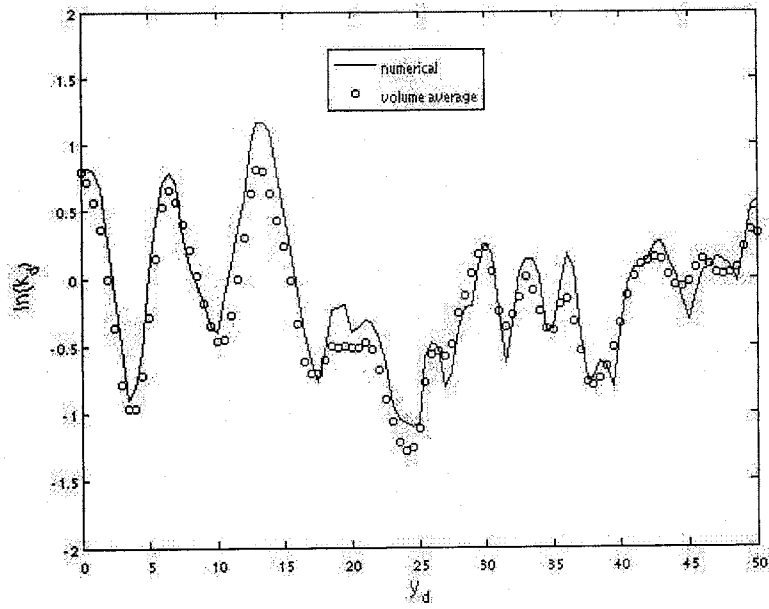
Figure B.17: Comparison between $\ln(k_{2,num})$ and $\ln(k_{D2})$.
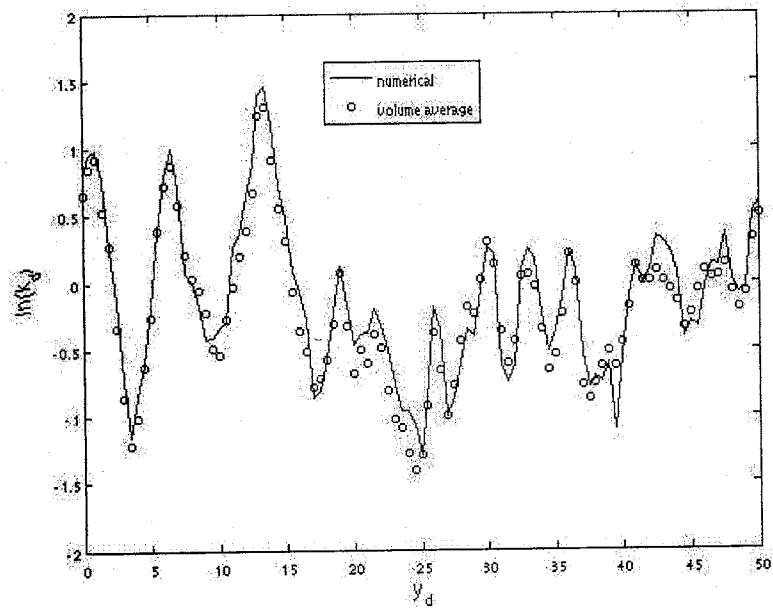
Figure B.18: Comparison between $\ln(k_{4,num})$ and $\ln(k_{D4})$.
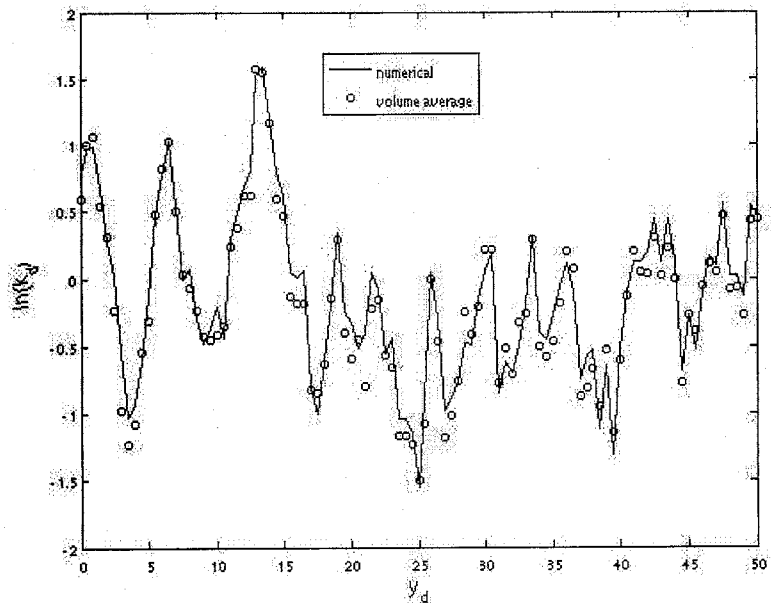
Figure B.19: Comparison between $\ln(k_{8,num})$ and $\ln(k_{D8})$.
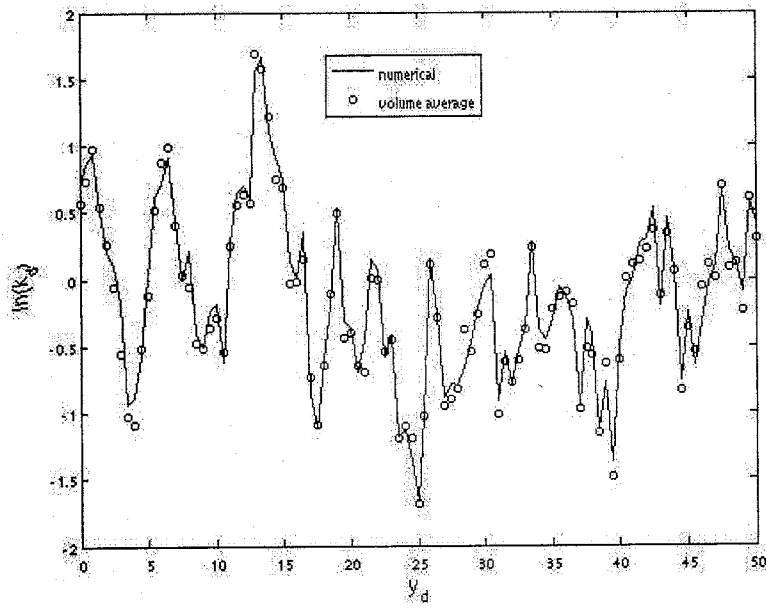
Figure B.20: Comparison between $\ln\left(k_{16,num}\right)$ and $\ln\left(k_{D16}\right)$.
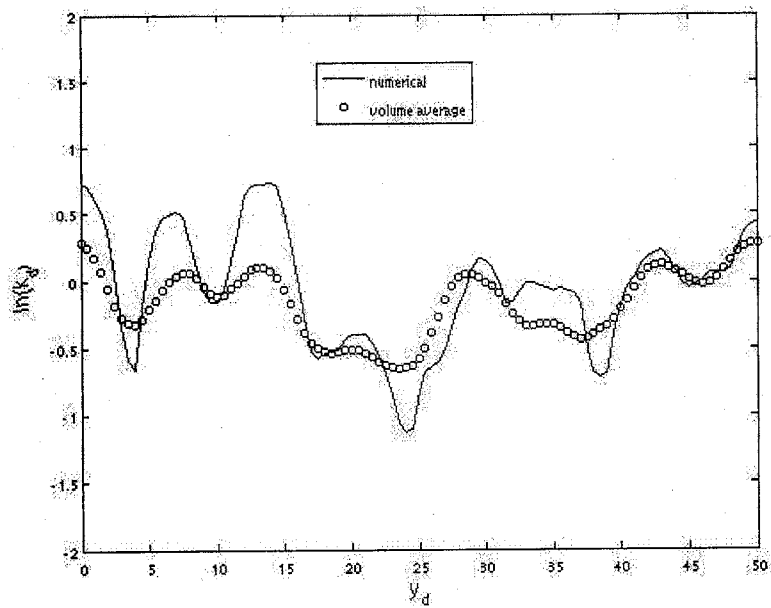
Figure B.21: Comparison between $\ln(k_{1,num})$ and $\ln(k_{E1})$.
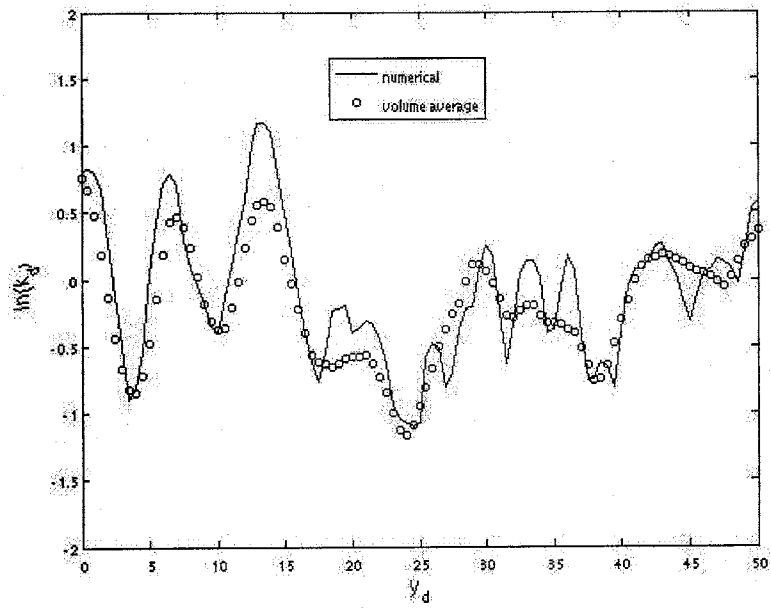
Figure B.22: Comparison between $\ln\left(k_{2,num}\right)$ and $\ln\left(k_{E2}\right)$.
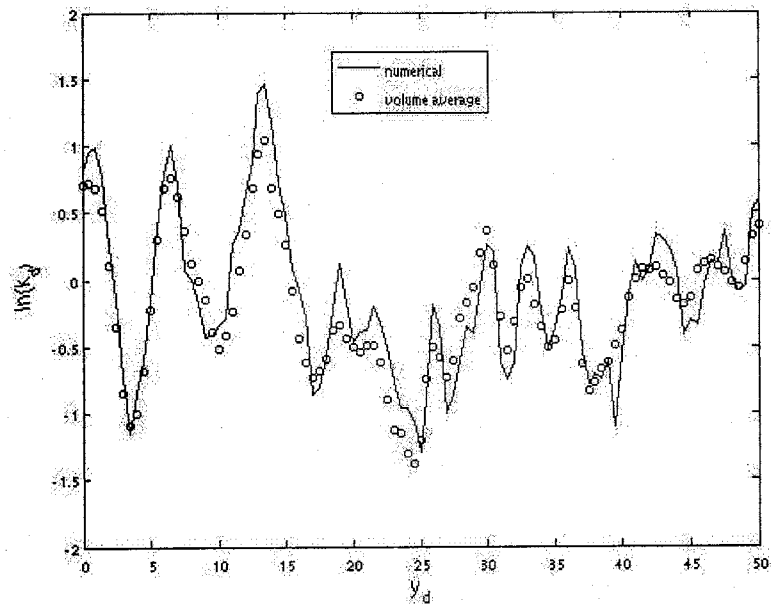
Figure B.23: Comparison between $\ln\left(k_{4,num}\right)$ and $\ln\left(k_{E4}\right)$.
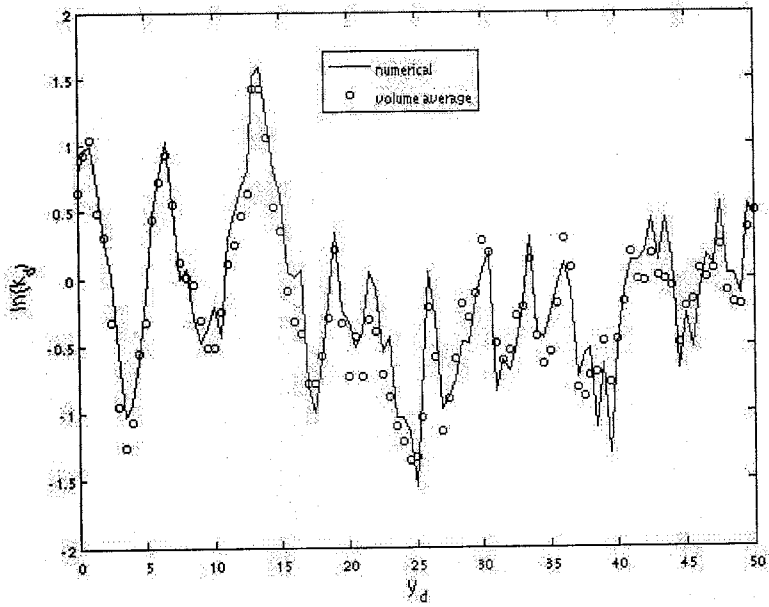
Figure B.24: Comparison between $\ln\left(k_{8,num}\right)$ and $\ln\left(k_{E8}\right)$.
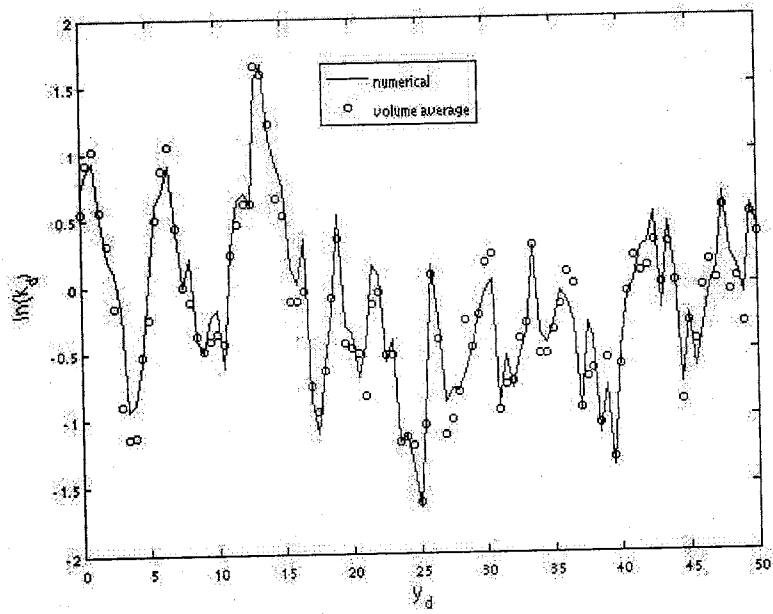
Figure B.25: Comparison between $\ln(k_{16,num})$ and $\ln(k_{E16})$.
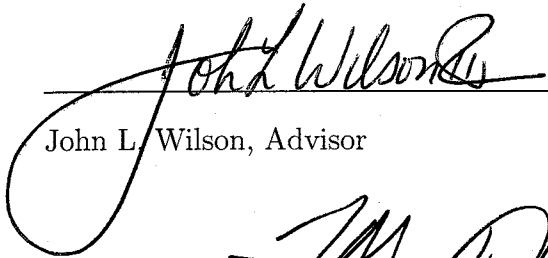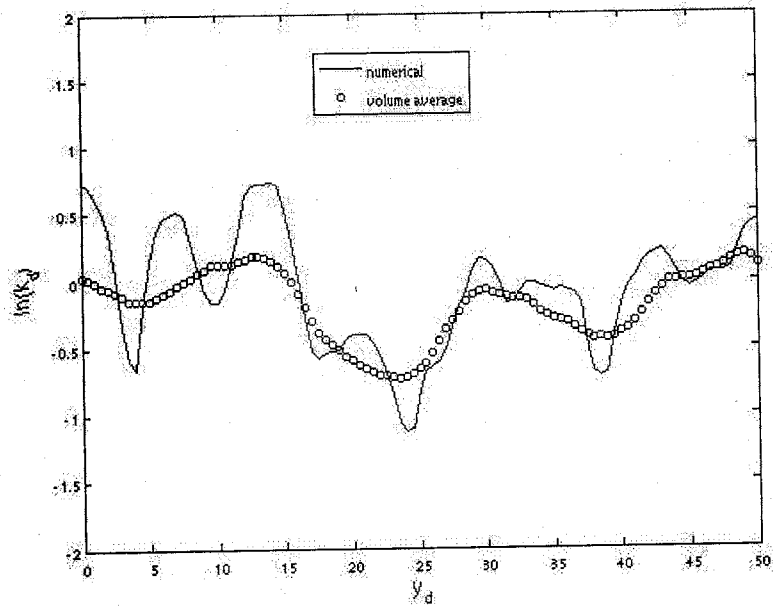
Figure B.26: Comparison between $\ln\left(k_{1,num}\right)$ and $\ln\left(k_{F1}\right)$.
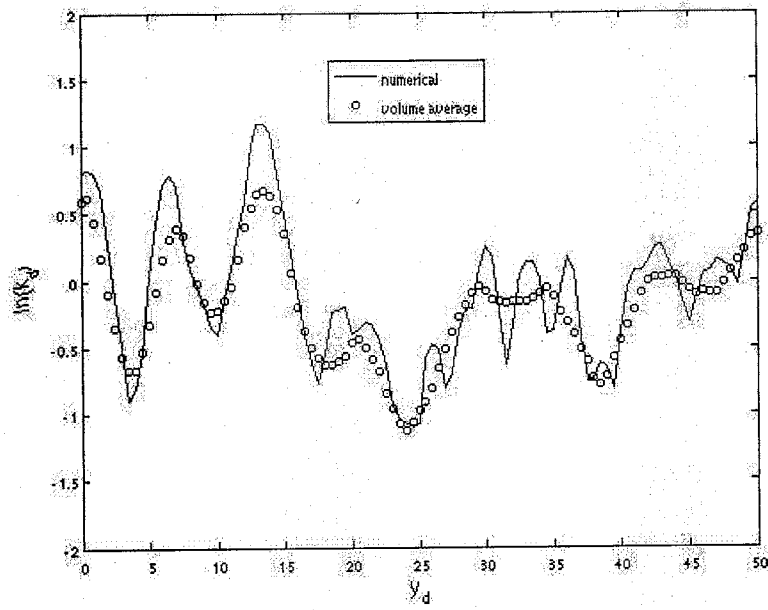
Figure B.27: Comparison between $\ln(k_{2,num})$ and $\ln(k_{F2})$.
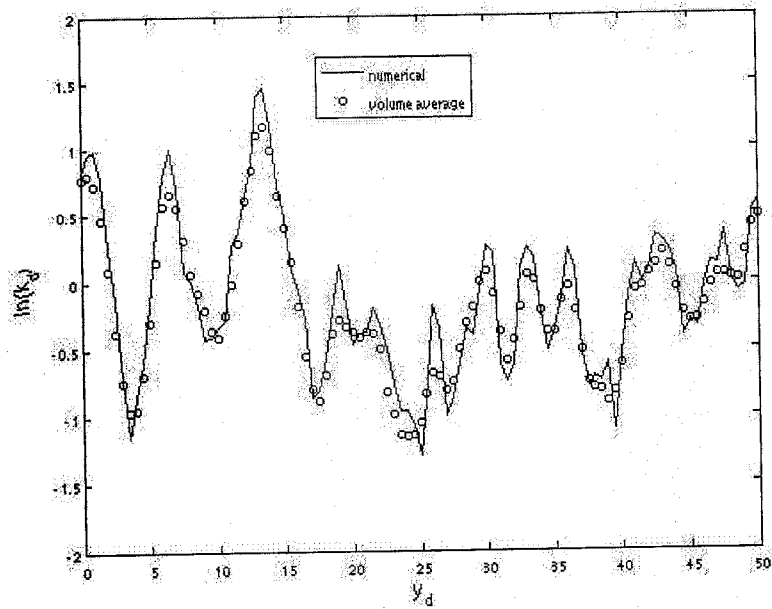
Figure B.28: Comparison between $\ln\left(k_{4,num}\right)$ and $\ln\left(k_{F4}\right)$.
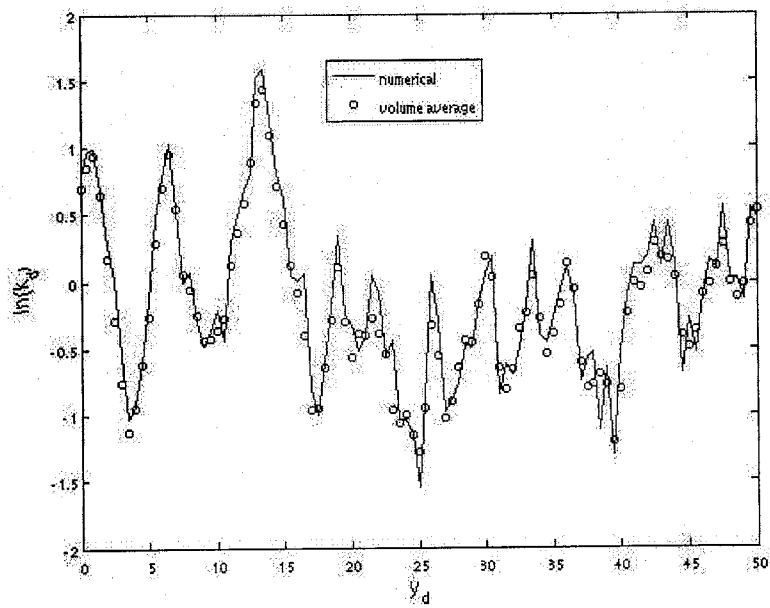
Figure B.29: Comparison between $\ln\left(k_{8,num}\right)$ and $\ln\left(k_{F8}\right)$.
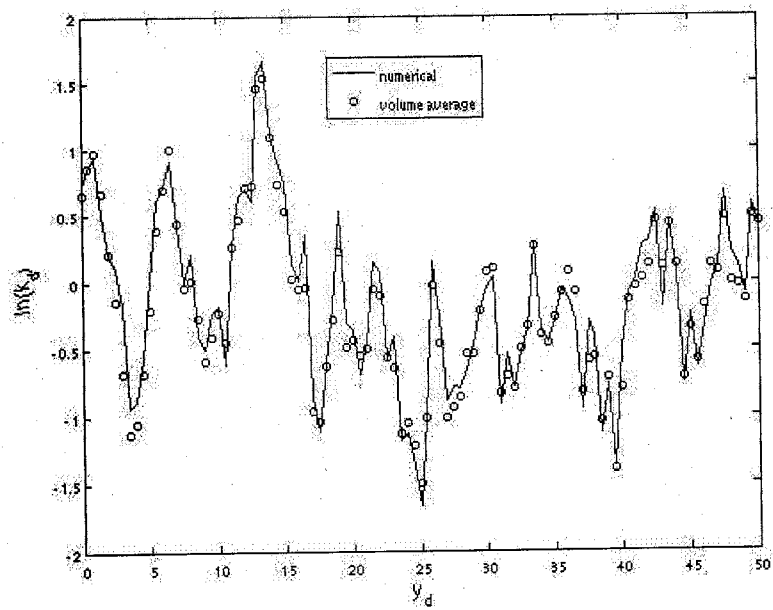
Figure B.30: Comparison between $\ln\left(k_{16,num}\right)$ and $\ln\left(k_{F16}\right)$.
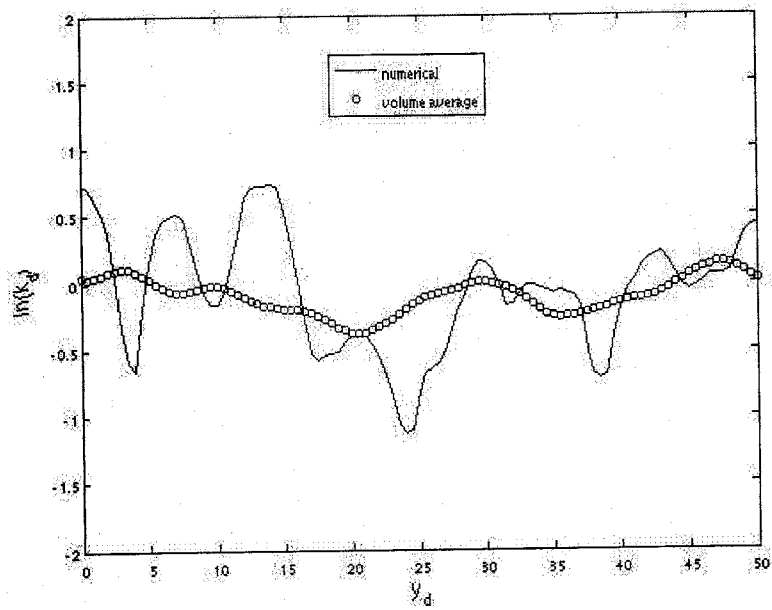
Figure B.31: Comparison between $\ln\left(k_{1,num}\right)$ and $\ln\left(k_{G1}\right)$.

141
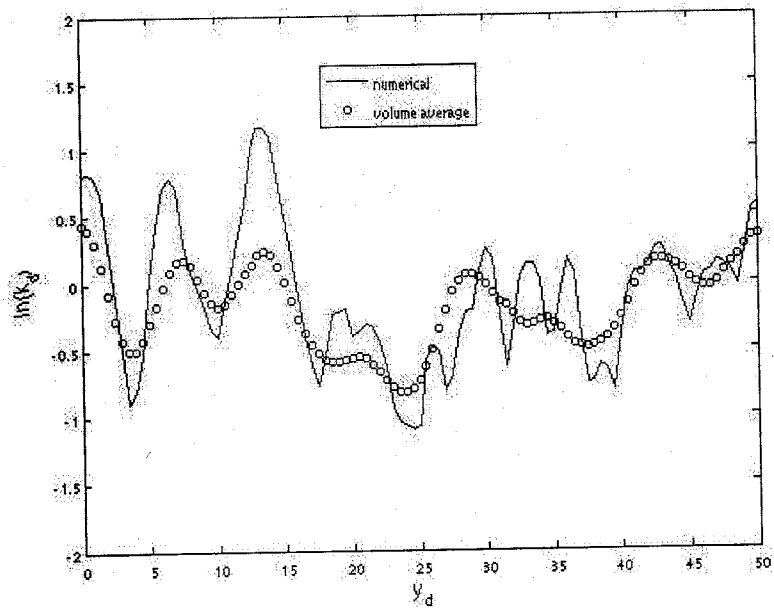
Figure B.32: Comparison between $\ln\left(k_{2,num}\right)$ and $\ln\left(k_{G2}\right)$.
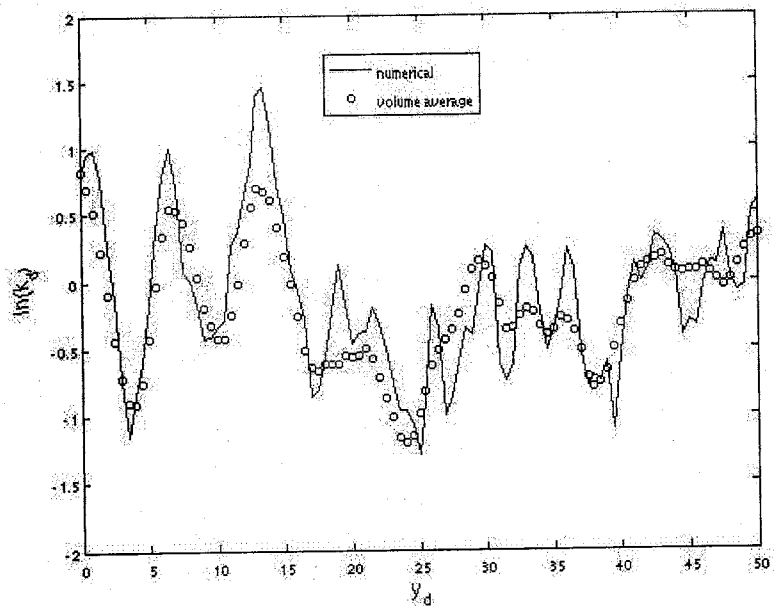
Figure B.33: Comparison between $\ln(k_{4,num})$ and $\ln(k_{G4})$.

143
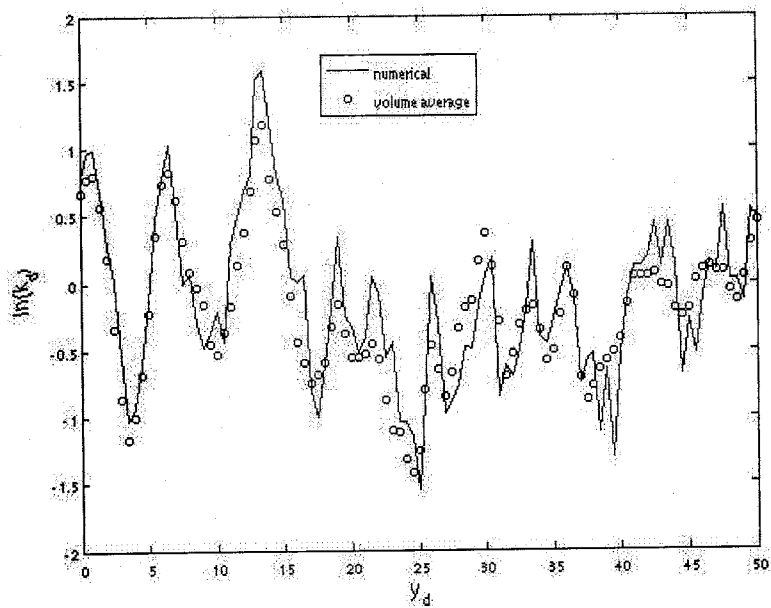
Figure B.34: Comparison between $\ln\left(k_{8,num}\right)$ and $\ln\left(k_{G8}\right)$.

144
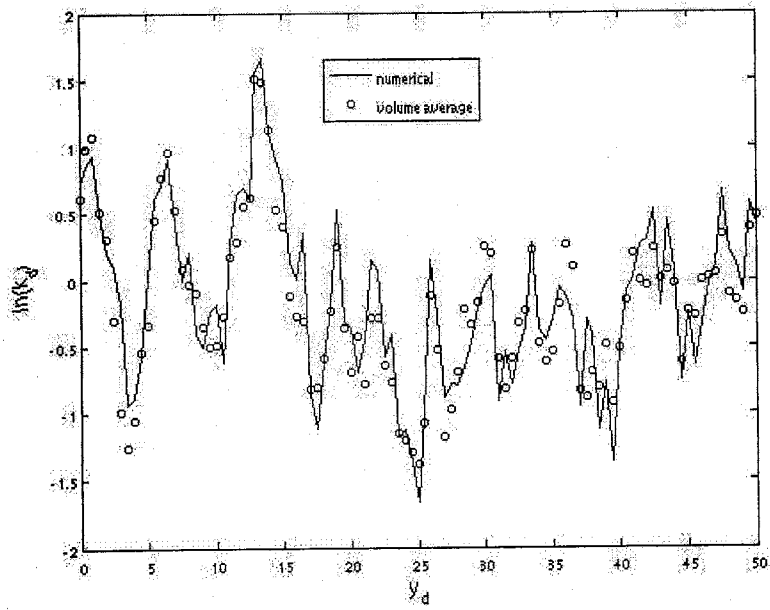
Figure B.35: Comparison between $\ln\left(k_{16,num}\right)$ and $\ln\left(k_{G16}\right)$.
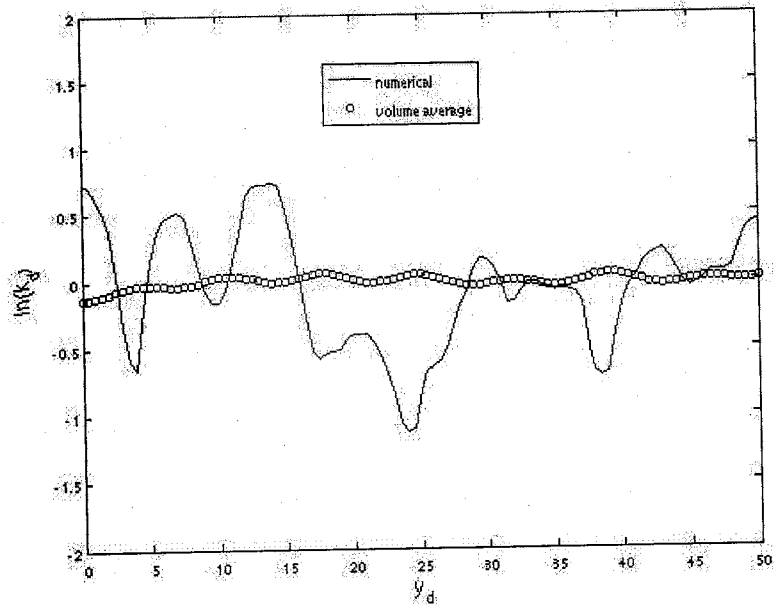
Figure B.36: Comparison between $\ln{(k_{1,num})}$ and $\ln{(k_{H1})}$.
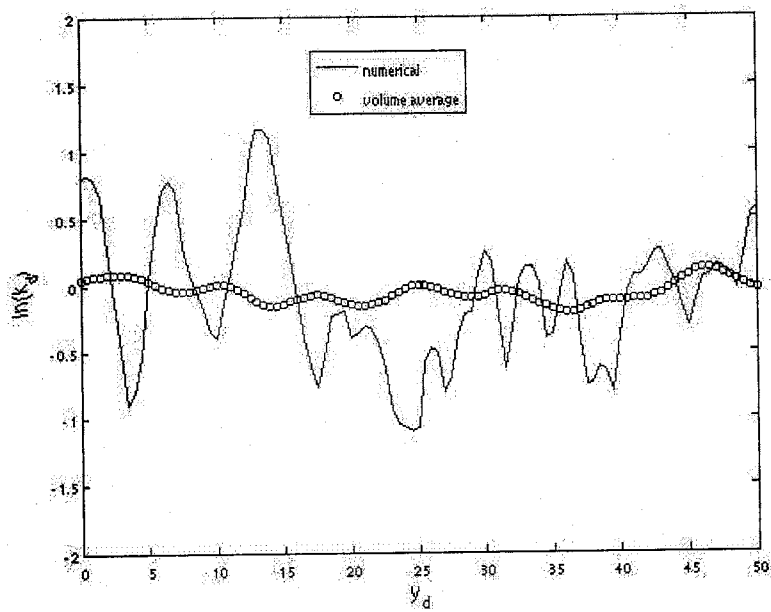
Figure B.37: Comparison between $\ln\left(k_{2,num}\right)$ and $\ln\left(k_{H2}\right)$.
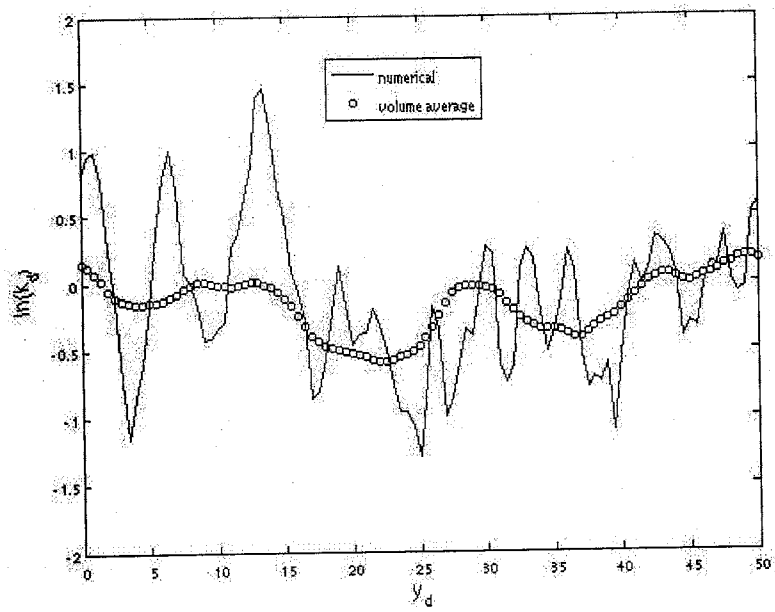
Figure B.38: Comparison between $\ln\left(k_{4,num}\right)$ and $\ln\left(k_{H4}\right)$.
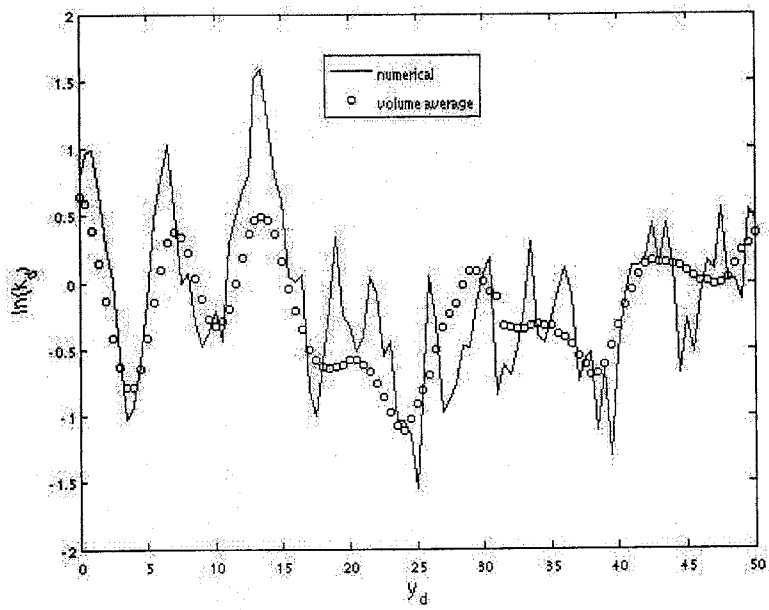
Figure B.39: Comparison between $\ln\left(k_{8,num}\right)$ and $\ln\left(k_{H8}\right)$.
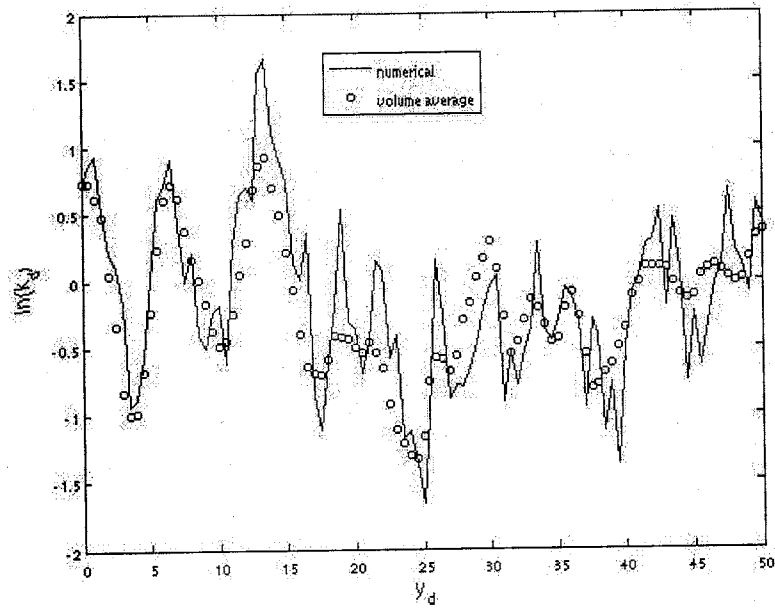
Figure B.40: Comparison between $\ln\left(k_{16,num}\right)$ and $\ln\left(k_{H16}\right)$.
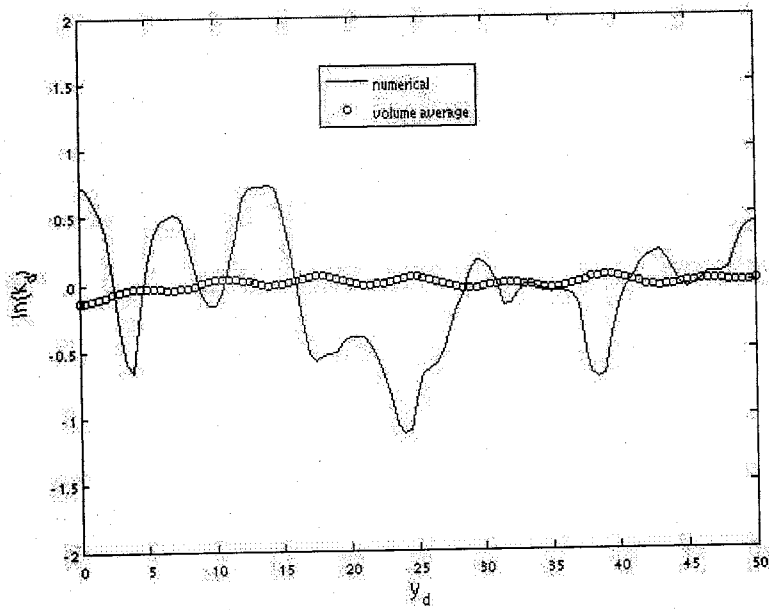
Figure B.41: Comparison between $\ln\left(k_{1,num}\right)$ and $\ln\left(k_{U1}\right)$.
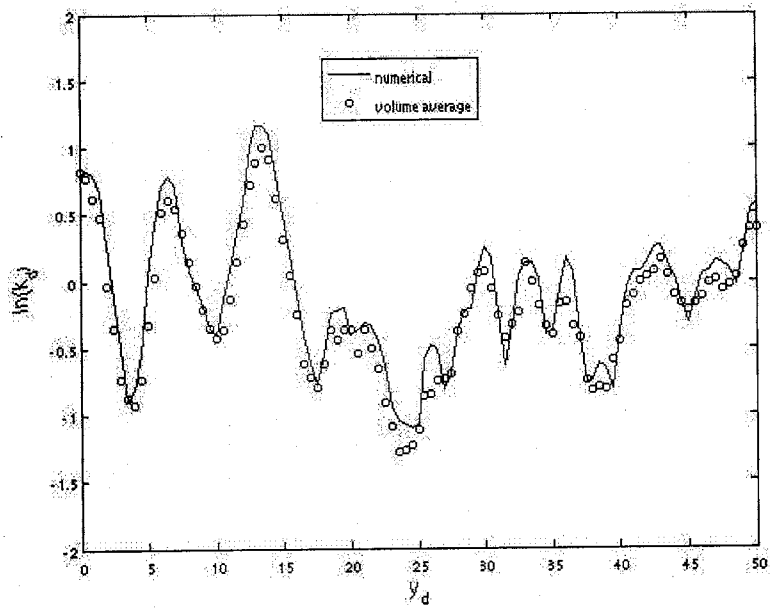
Figure B.42: Comparison between $\ln\left(k_{2,num}\right)$ and $\ln\left(k_{U2}\right)$.

Figure B.43: Comparison between $\ln\left(k_{4,num}\right)$ and $\ln\left(k_{U4}\right)$.
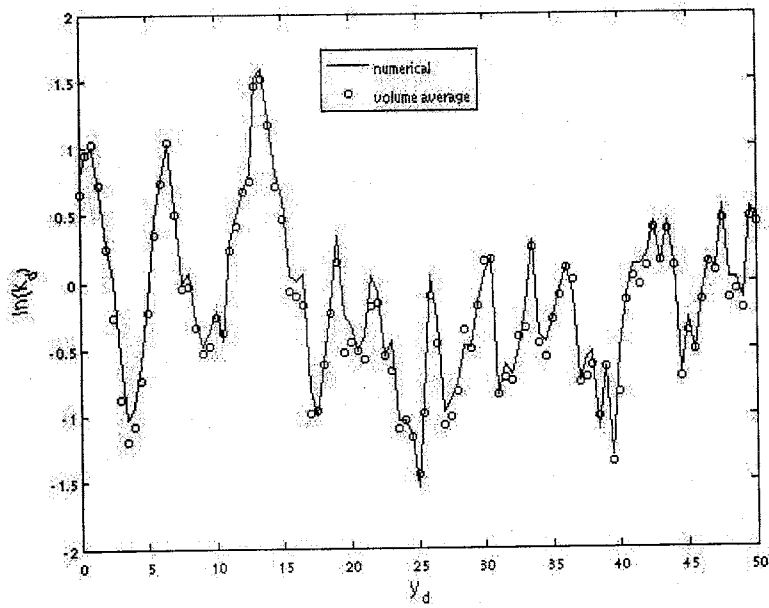
Figure B.44: Comparison between $\ln(k_{8,num})$ and $\ln(k_{U8})$.

154
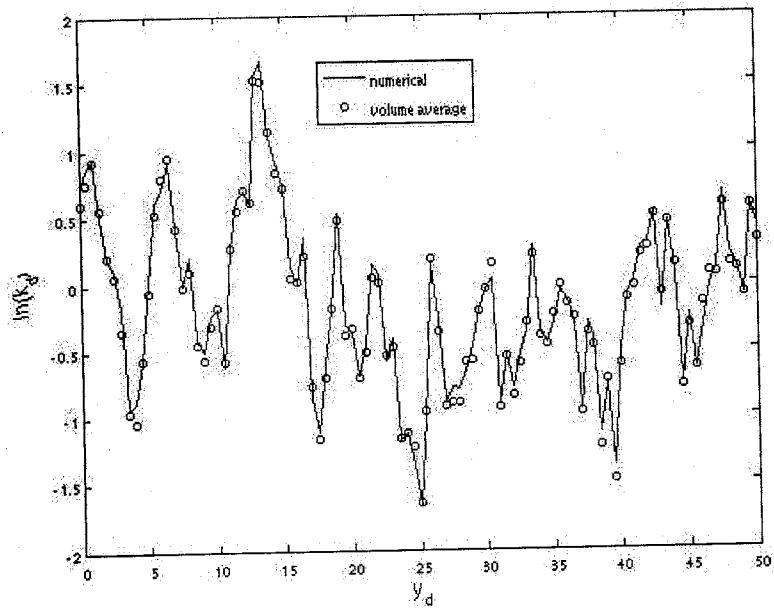
Figure B.45: Comparison between $\ln\left(k_{16,num}\right)$ and $\ln\left(k_{U16}\right)$.

APPENDIX C

Scatter Plots of Volume Averaged vs. Effective Numerical Natural Log Permeability
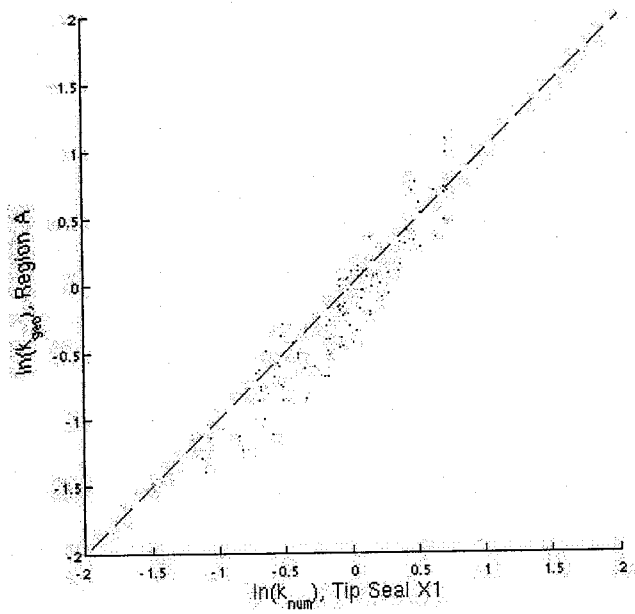
Figure C.1: Scatter plot of $\ln(k_{A1})$ vs. $\ln(k_{1,num})$.
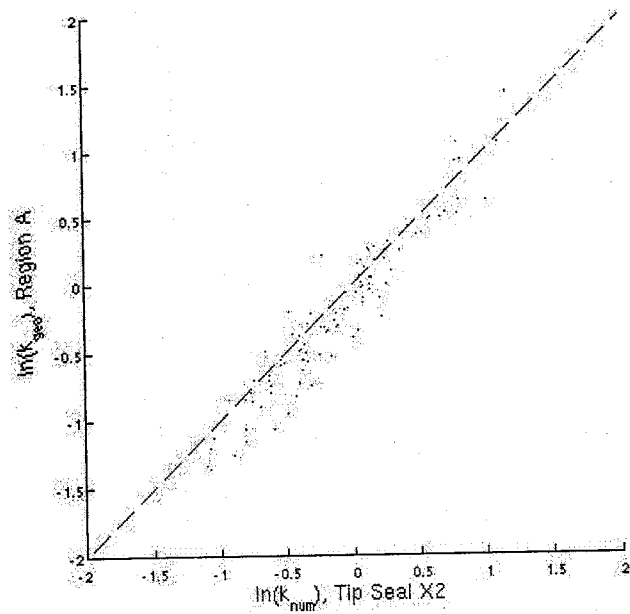
Figure C.2: Scatter plot of $\ln\left(k_{A2}\right)$ vs. $\ln\left(k_{2,num}\right)$.
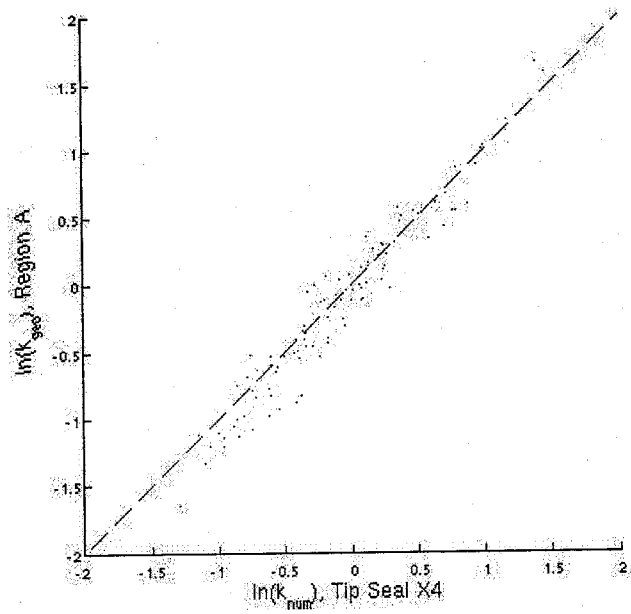
Figure C.3: Scatter plot of $\ln(k_{A4})$ vs. $\ln(k_{4,num})$.
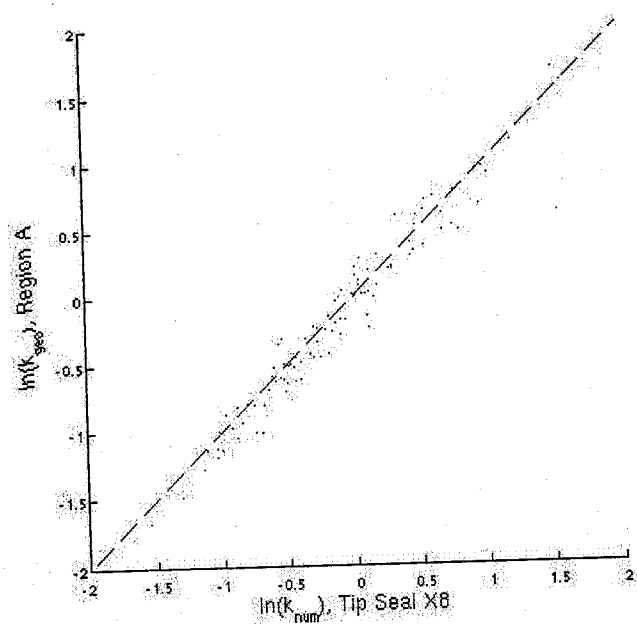
Figure C.4: Scatter plot of $\ln\left(k_{A8}\right)$ vs. $\ln\left(k_{8,num}\right)$.

160
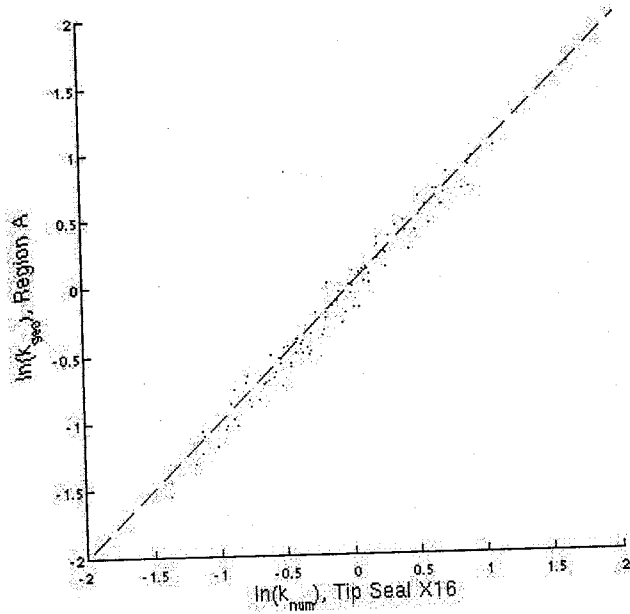
Figure C.5: Scatter plot of $\ln(k_{A16})$ vs. $\ln(k_{16,num})$.
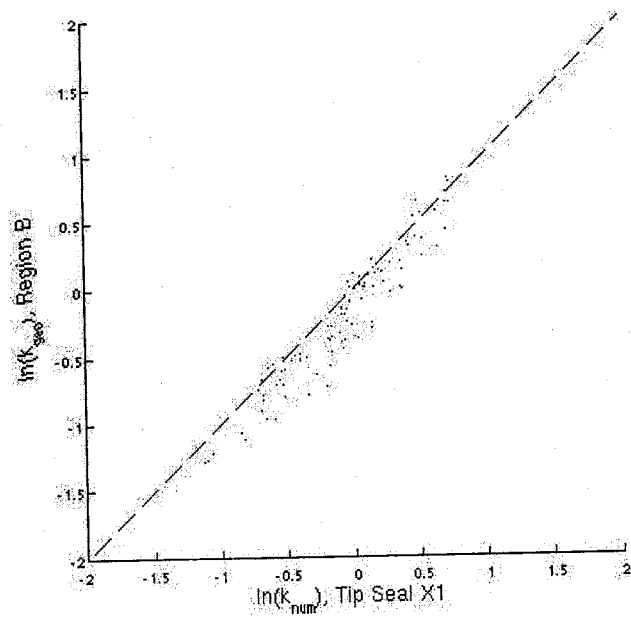
Figure C.6: Scatter plot of $\ln\left(k_{B1}\right)$ vs. $\ln\left(k_{1,num}\right)$.
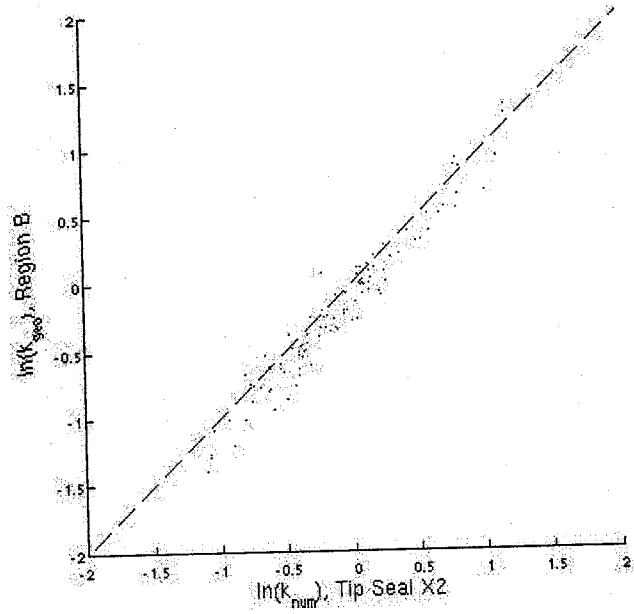
Figure C.7: Scatter plot of $\ln\left(k_{B2}\right)$ vs. $\ln\left(k_{2,num}\right)$.
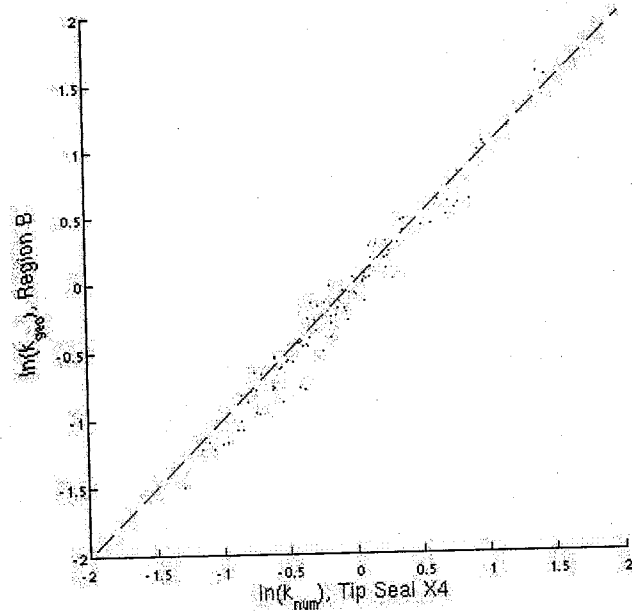
Figure C.8: Scatter plot of $\ln(k_{B4})$ vs. $\ln(k_{4,num})$.
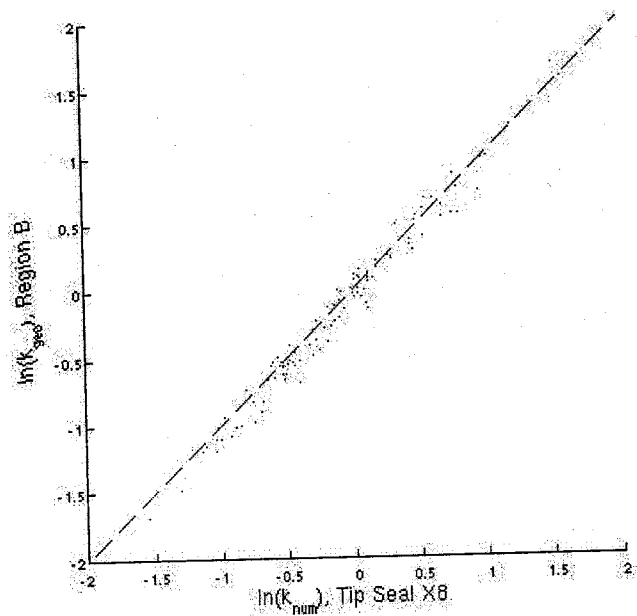
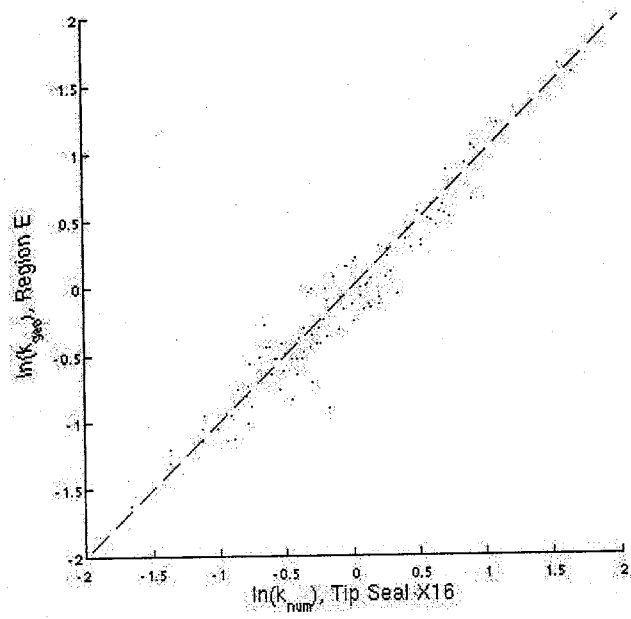Figure C.9: Scatter plot of $\ln(k_{B8})$ vs. $\ln(k_{8,num})$.

165
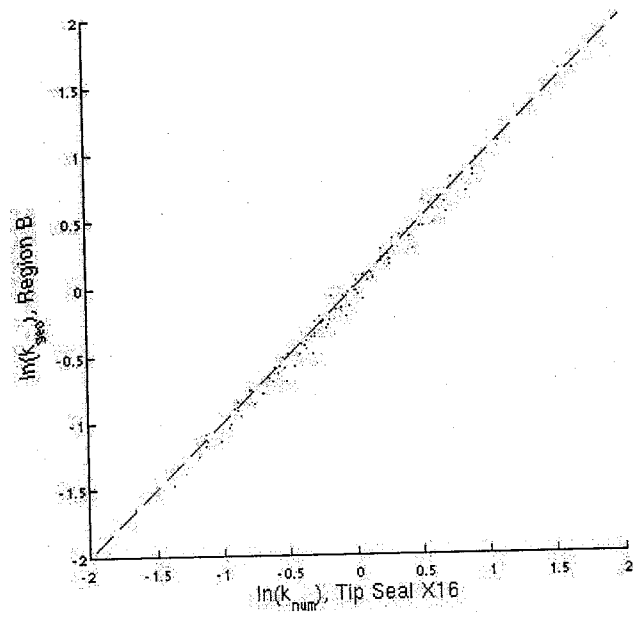
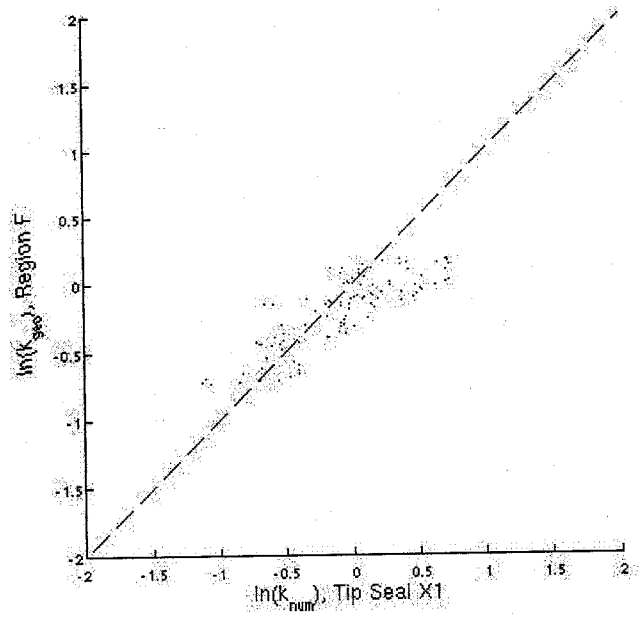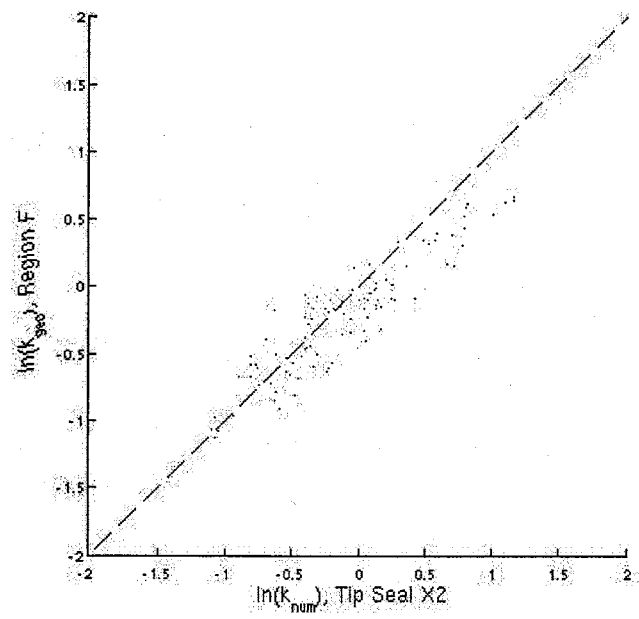Figure C.10: Scatter plot of $\ln(k_{B16})$ vs. $\ln(k_{16,num})$.
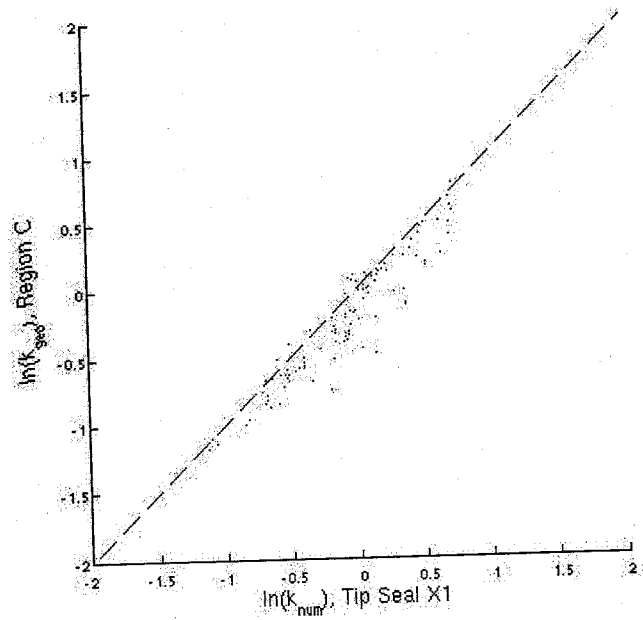
Figure C.11: Scatter plot of $\ln\left(k_{C1}\right)$ vs. $\ln\left(k_{1,num}\right)$.
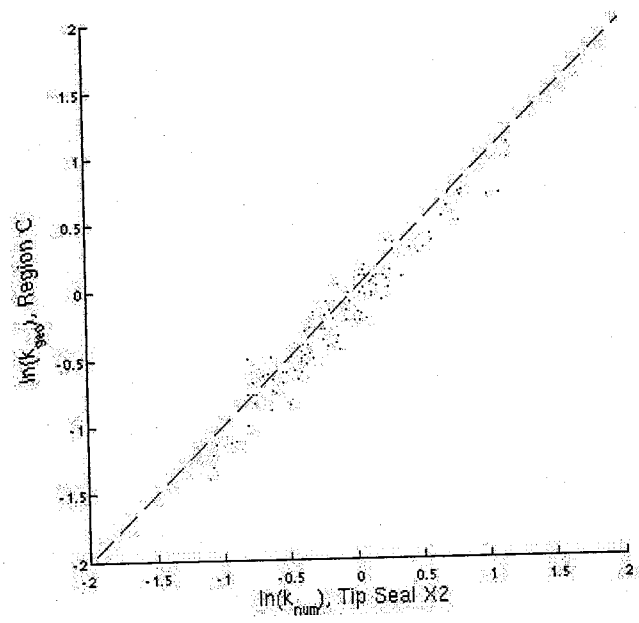
Figure C.12: Scatter plot of $\ln\left(k_{C2}\right)$ vs. $\ln\left(k_{2,num}\right)$.
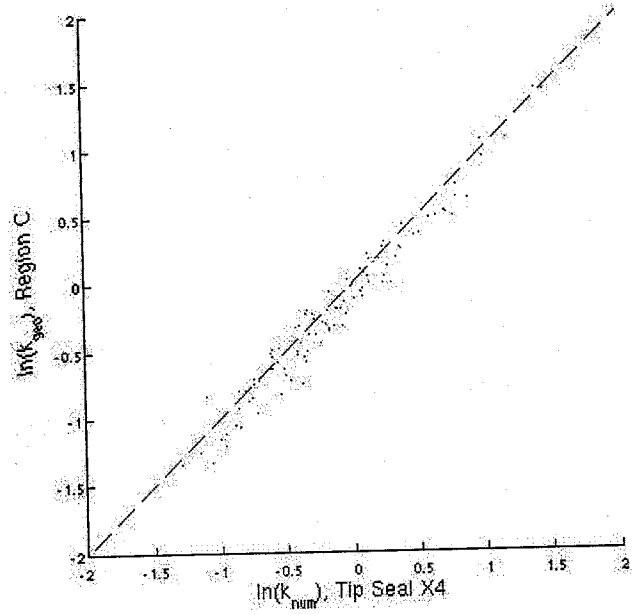
Figure C.13: Scatter plot of $\ln(k_{C4})$ vs. $\ln(k_{4,num})$.
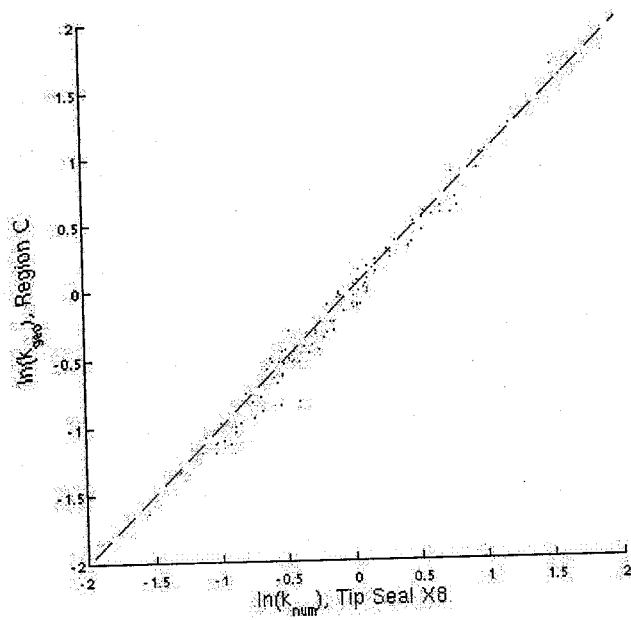
Figure C.14: Scatter plot of $\ln\left(k_{C8}\right)$ vs. $\ln\left(k_{8,num}\right)$.
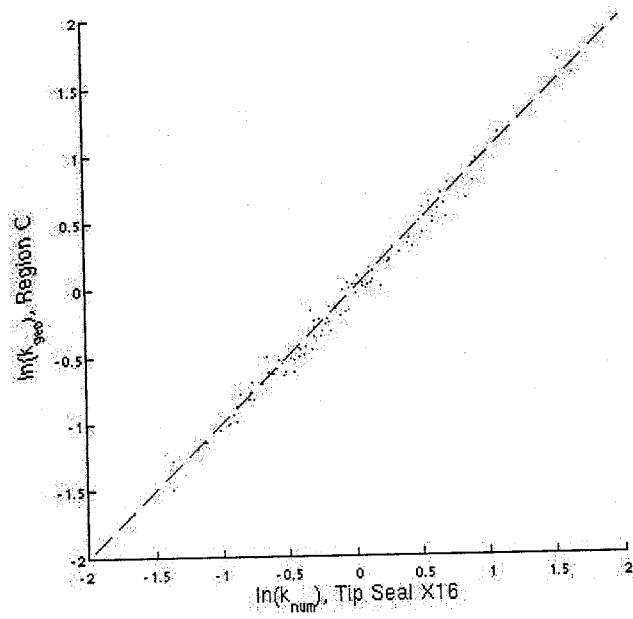
Figure C.15: Scatter plot of $\ln\left(k_{C16}\right)$ vs. $\ln\left(k_{16,num}\right)$.

171
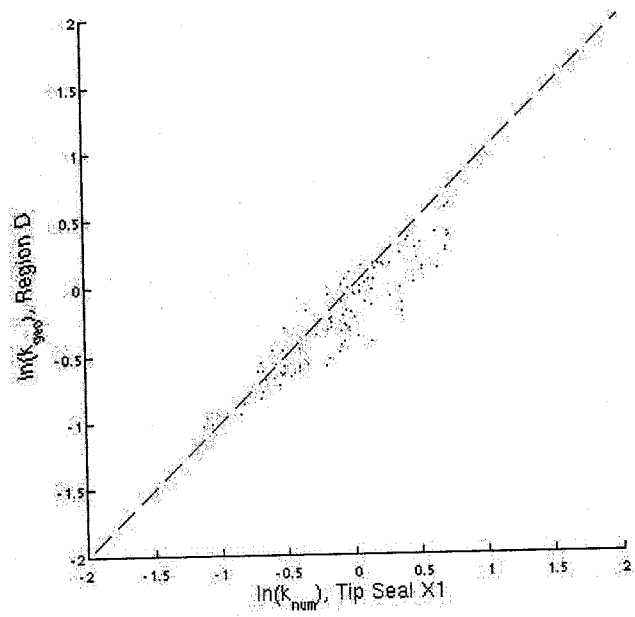
Figure C.16: Scatter plot of $\ln(k_{D1})$ vs. $\ln(k_{1,num})$.
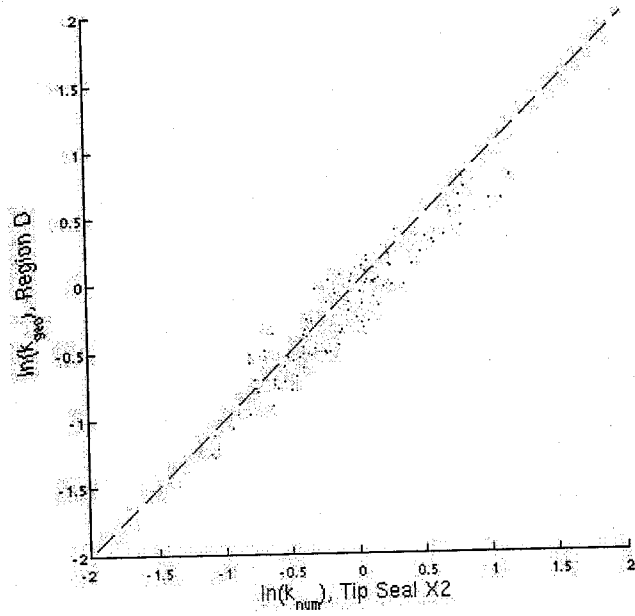
Figure C.17: Scatter plot of $\ln(k_{D2})$ vs. $\ln(k_{2,num})$.
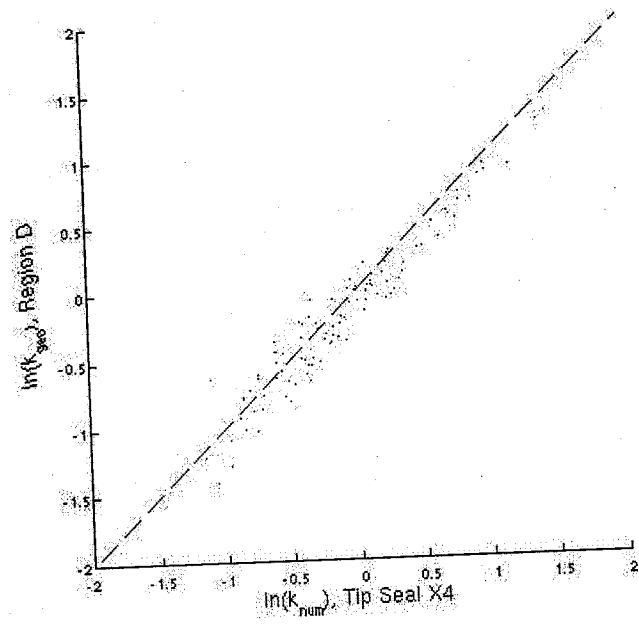
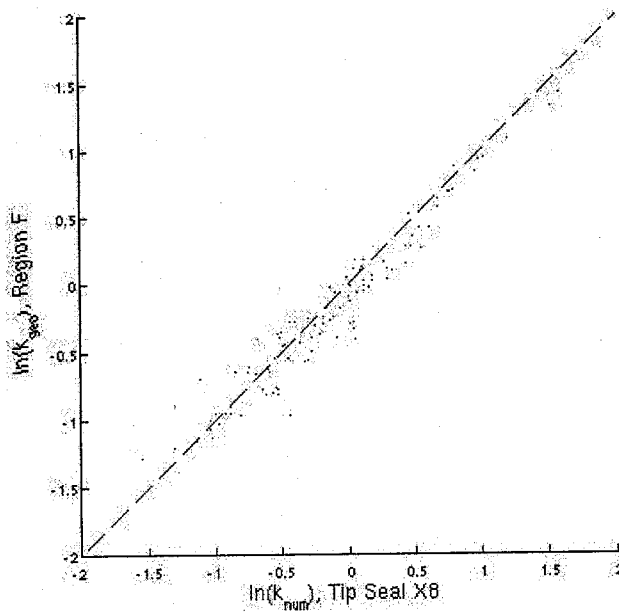Figure C.18: Scatter plot of $\ln(k_{D4})$ vs. $\ln(k_{4,num})$.
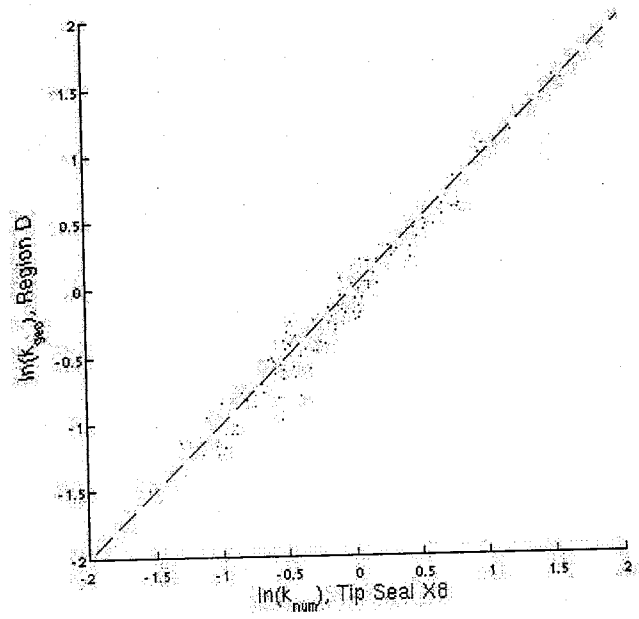
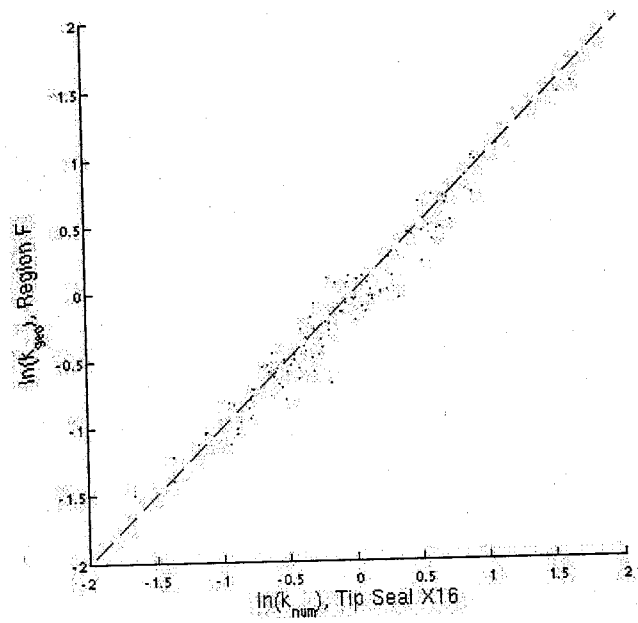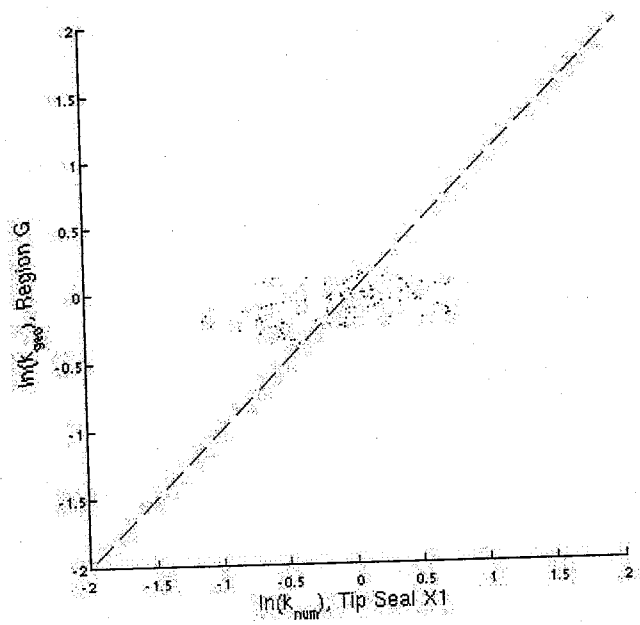Figure C.19: Scatter plot of $\ln(k_{D8})$ vs. $\ln(k_{8,num})$.
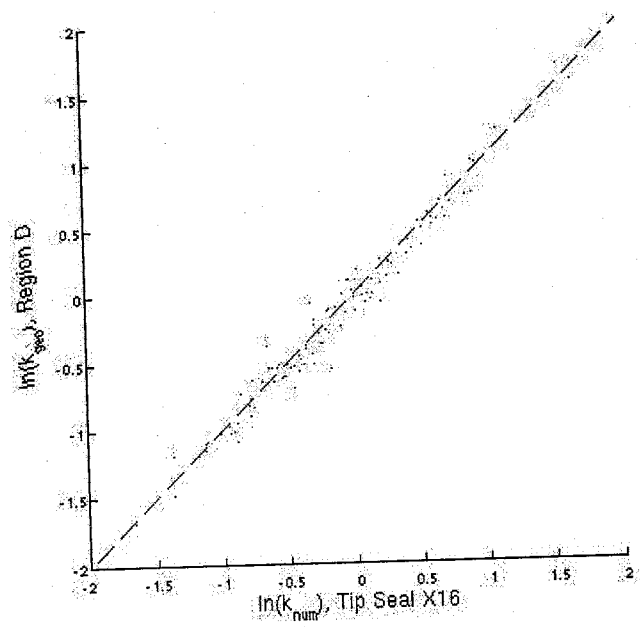
Figure C.20: Scatter plot of $\ln\left(k_{D16}\right)$ vs. $\ln\left(k_{16,num}\right)$.
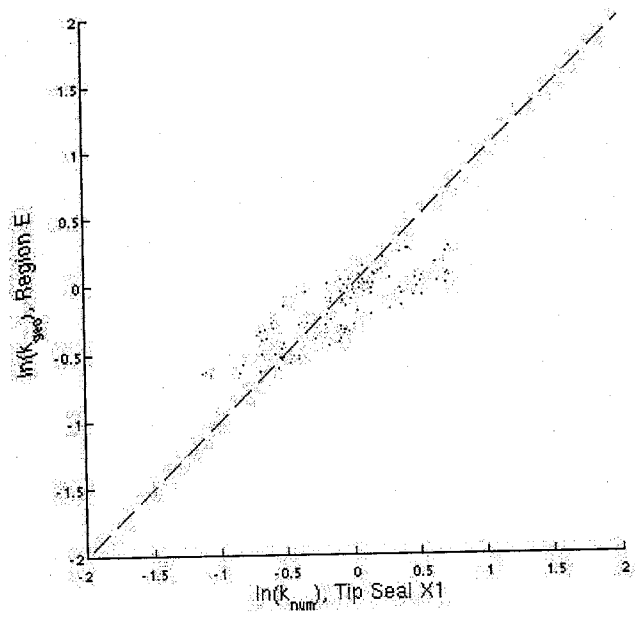
Figure C.21: Scatter plot of $\ln\left(k_{E1}\right)$ vs. $\ln\left(k_{1,num}\right)$.
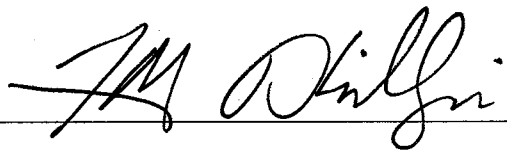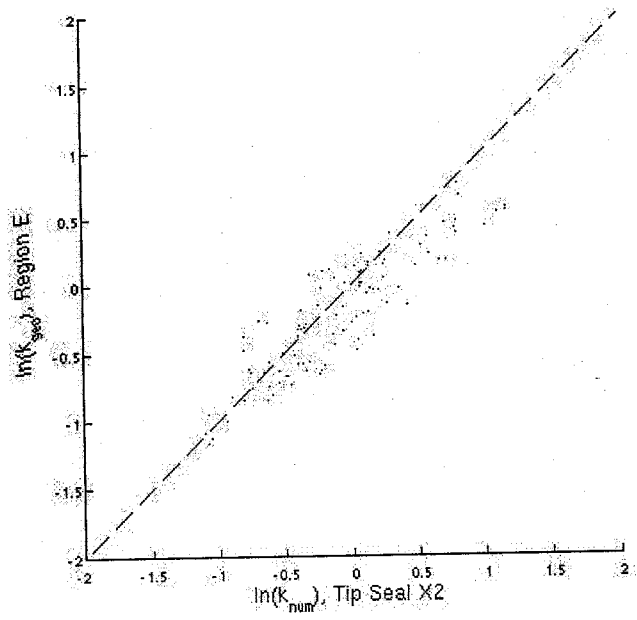
Figure C.22: Scatter plot of $\ln\left(k_{E2}\right)$ vs. $\ln\left(k_{2,num}\right)$.
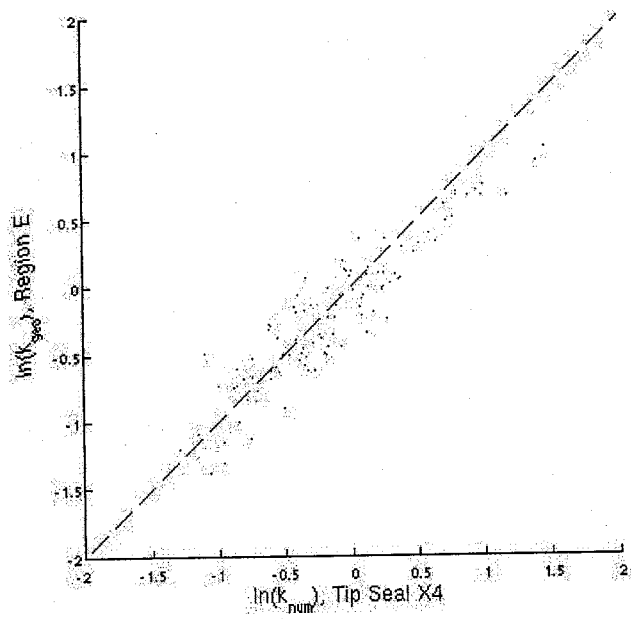
Figure C.23: Scatter plot of $\ln\left(k_{E4}\right)$ vs. $\ln\left(k_{4,num}\right)$.
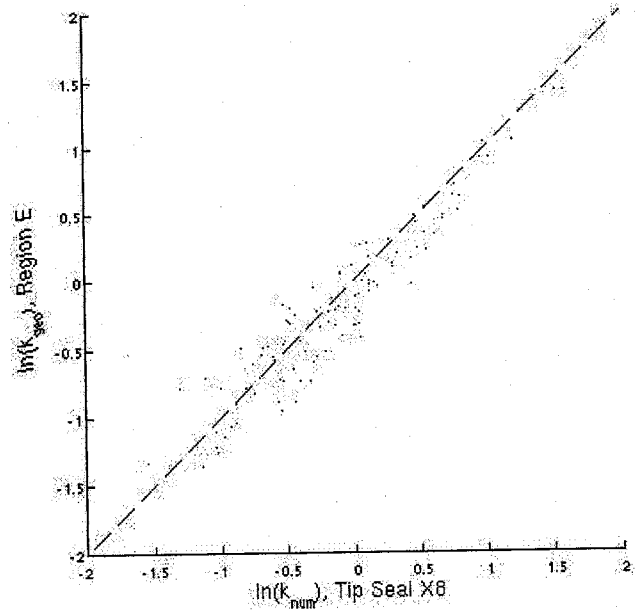
Figure C.24: Scatter plot of $\ln(k_{E8})$ vs. $\ln(k_{8,num})$.

Figure C.25: Scatter plot of $\ln(k_{E16})$ vs. $\ln(k_{16,num})$.

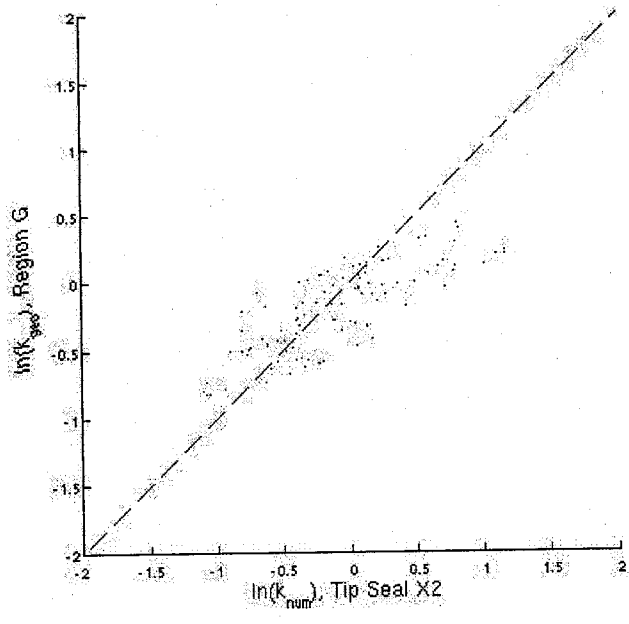Figure C.26: Scatter plot of $\ln(k_{F1})$ vs. $\ln(k_{1,num})$.

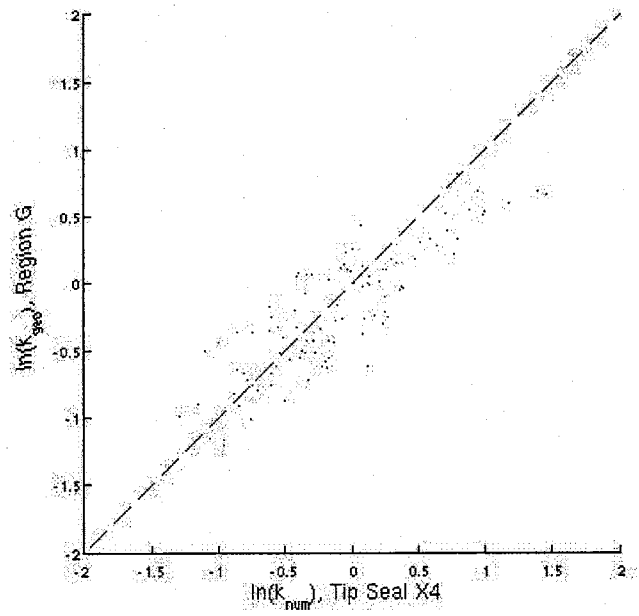Figure C.27: Scatter plot of $\ln(k_{F2})$ vs. $\ln(k_{2,num})$.
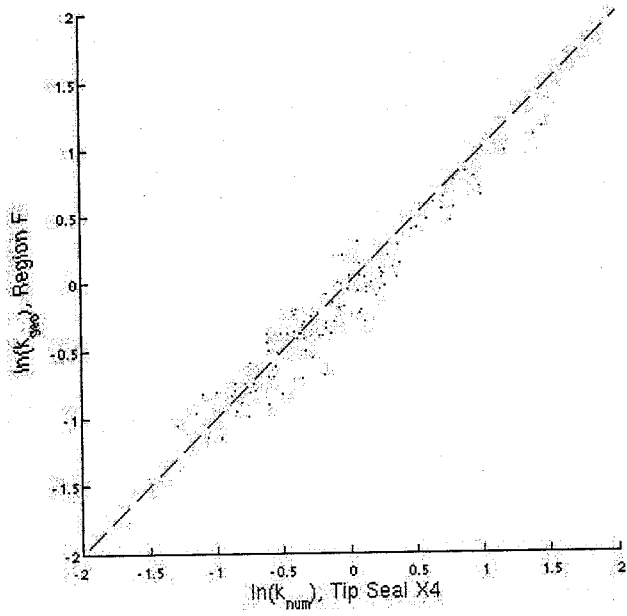
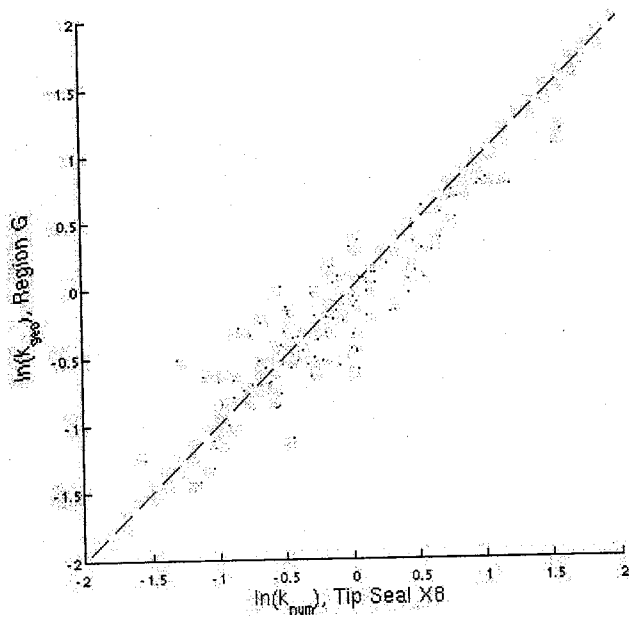Figure C.28: Scatter plot of $\ln(k_{F4})$ vs. $\ln(k_{4,num})$.

Figure C.29: Scatter plot of $\ln\left(k_{F8}\right)$ vs. $\ln\left(k_{8,num}\right)$.
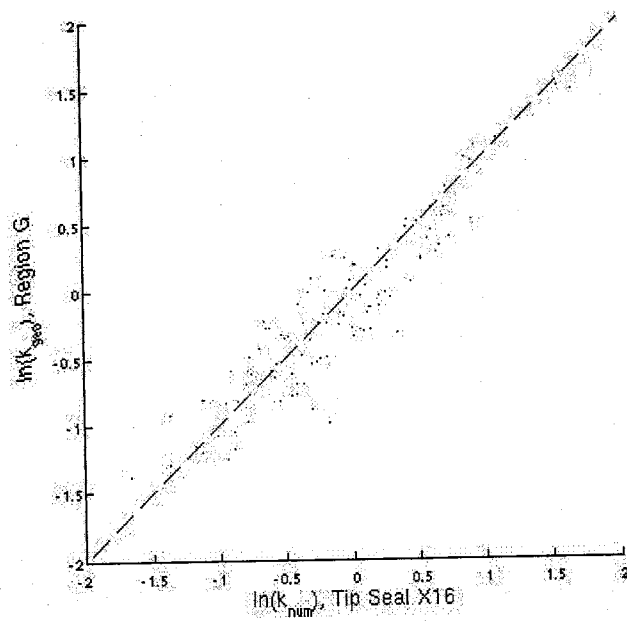
Figure C.30: Scatter plot of $\ln(k_{F16})$ vs. $\ln(k_{16,num})$.

Figure C.31: Scatter plot of $\ln(k_{G1})$ vs. $\ln(k_{1,num})$.

Figure C.32: Scatter plot of $\ln\left(k_{G2}\right)$ vs. $\ln\left(k_{2,num}\right)$.

Figure C.33: Scatter plot of $\ln\left(k_{G4}\right)$ vs. $\ln\left(k_{4,num}\right)$.

Figure C.34: Scatter plot of $\ln\left(k_{G8}\right)$ vs. $\ln\left(k_{8,num}\right)$.

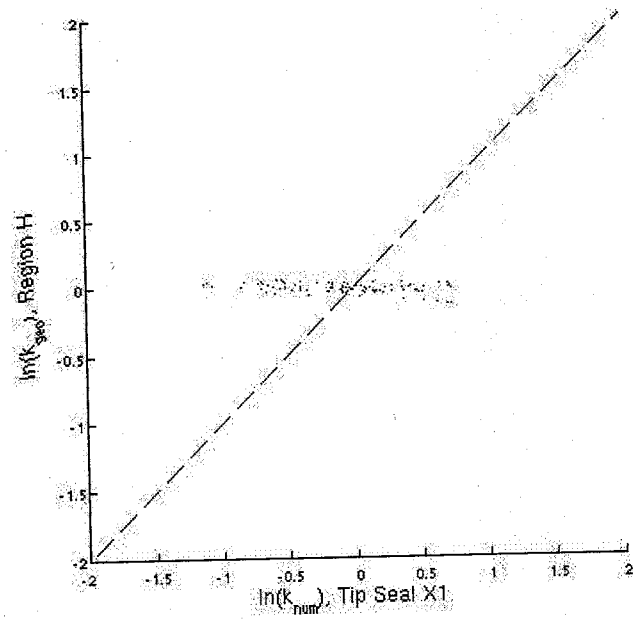Figure C.35: Scatter plot of $\ln(k_{G16})$ vs. $\ln(k_{16,num})$.

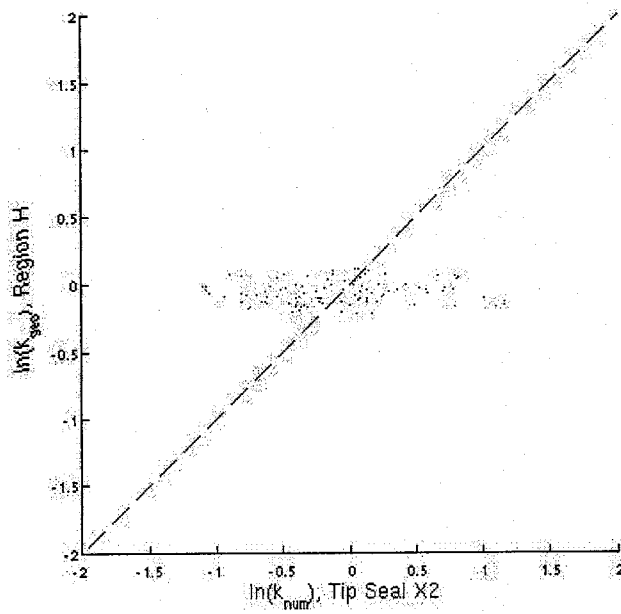Figure C.36: Scatter plot of $\ln(k_{H1})$ vs. $\ln(k_{1,num})$.

Figure C.37: Scatter plot of $\ln(k_{H2})$ vs. $\ln(k_{2,num})$.
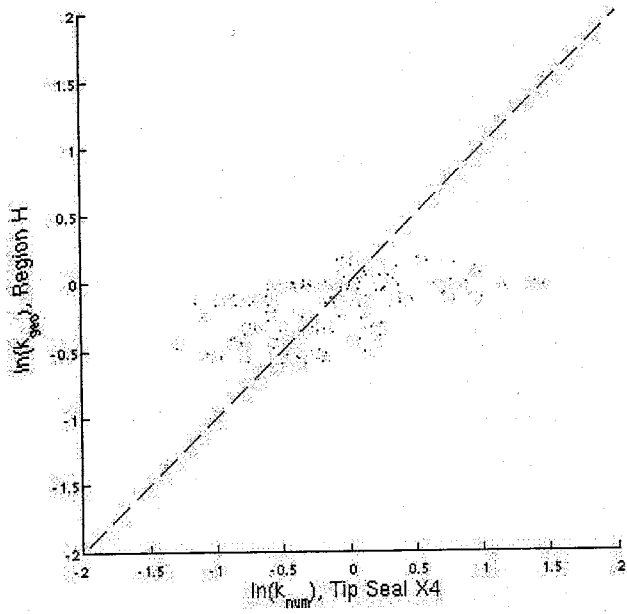
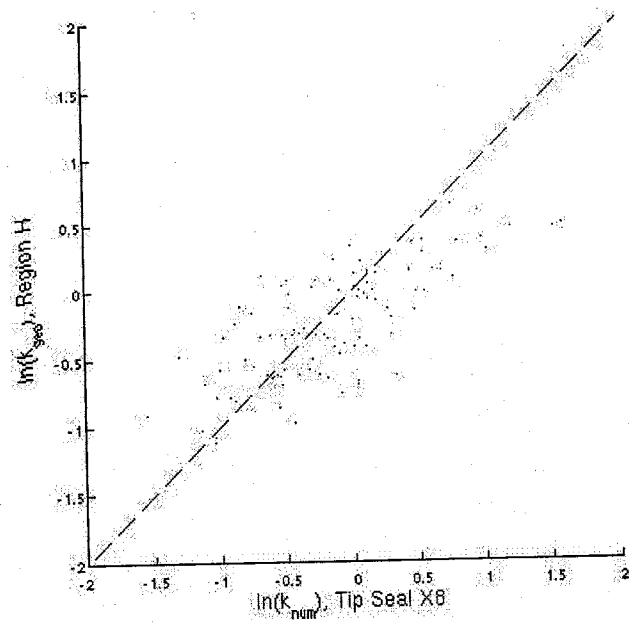Figure C.38: Scatter plot of $\ln(k_{H4})$ vs. $\ln(k_{4,num})$.

Figure C.39: Scatter plot of $\ln(k_{H8})$ vs. $\ln(k_{8,num})$.
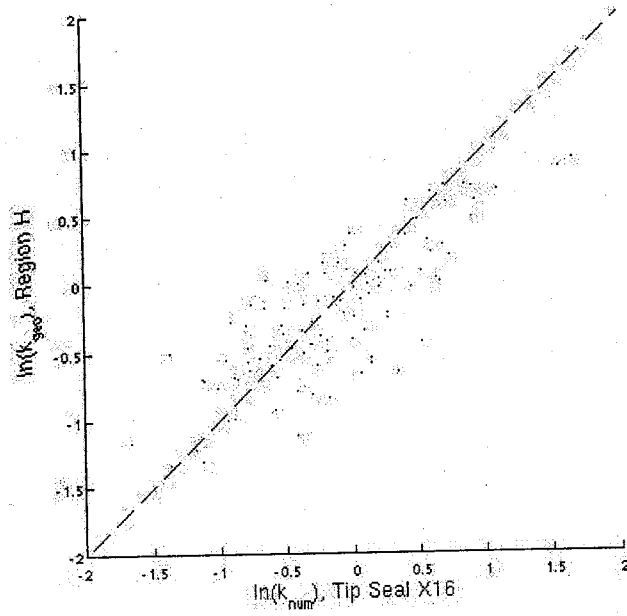
Figure C.40: Scatter plot of $\ln(k_{H16})$ vs. $\ln(k_{16,num})$.
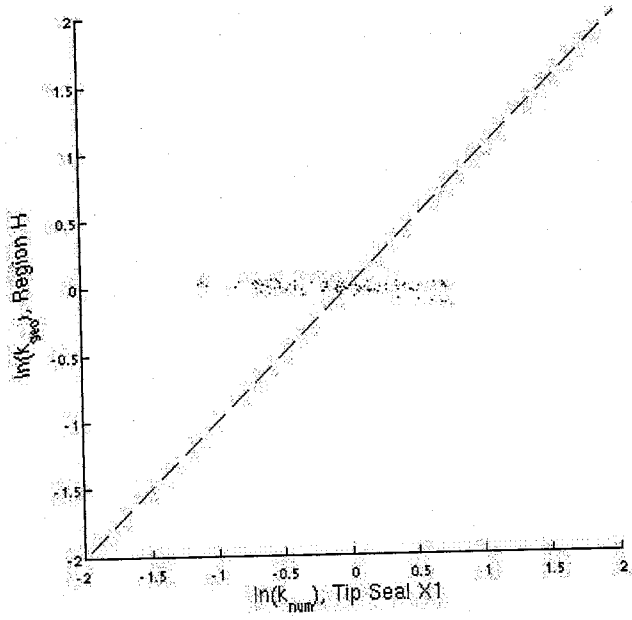
Figure C.41: Scatter plot of $\ln(k_{U1})$ vs. $\ln(k_{1,num})$.
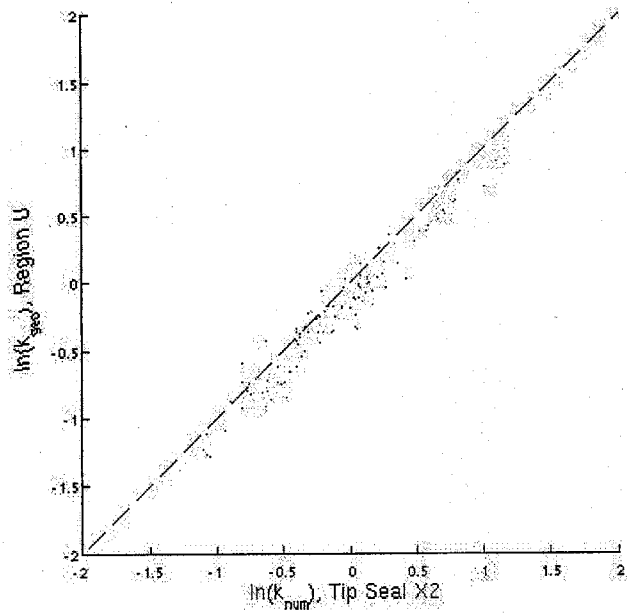
Figure C.42: Scatter plot of $\ln\left(k_{U2}\right)$ vs. $\ln\left(k_{2,num}\right)$.
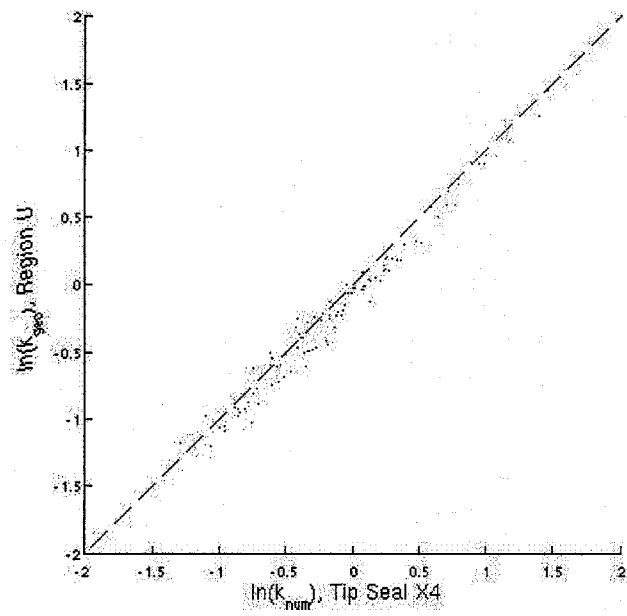
Figure C.43: Scatter plot of $\ln\left(k_{U4}\right)$ vs. $\ln\left(k_{4,num}\right)$.

Figure C.44: Scatter plot of $\ln(k_{U8})$ vs. $\ln(k_{8,num})$.

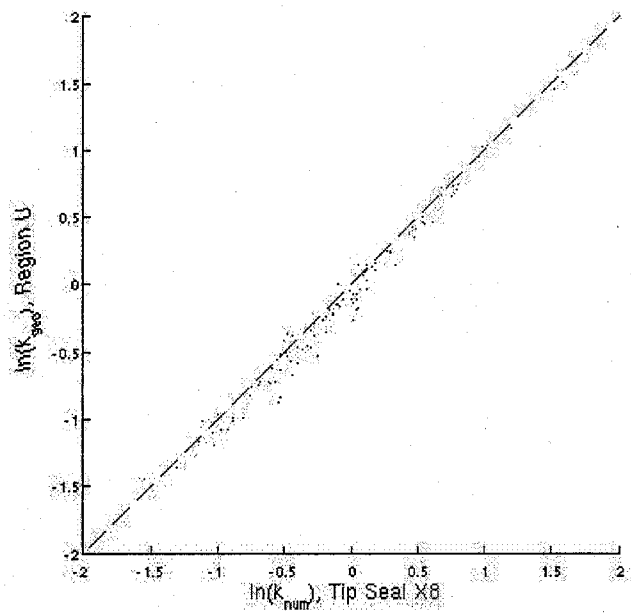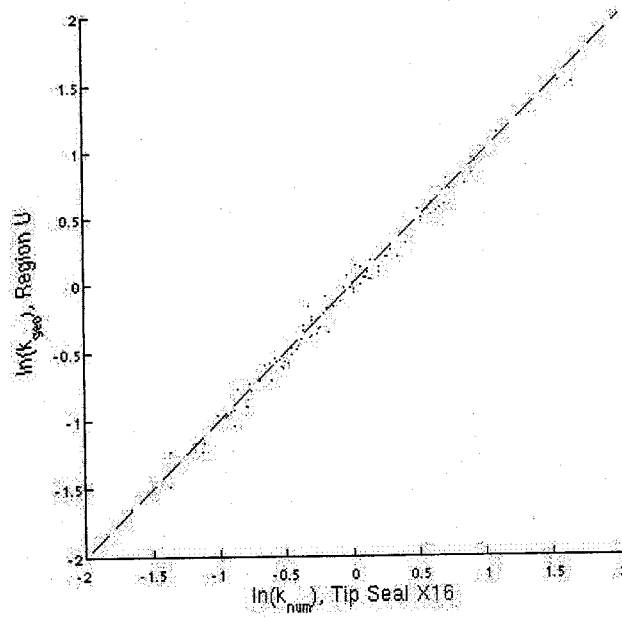Figure C.45: Scatter plot of $\ln\left(k_{U16}\right)$ vs. $\ln\left(k_{16,num}\right)$.

REFERENCES

Aronson,E., *Modeling Investigations on Gas Permeameters: Spatial Weighting Functions and Layered Systems*, MS Thesis, Hydrology, New Mexico Institute of Mining and Technology, May 1999

Bachu, S. and D. Cuthiell, Effects of core-scale heterogeneity on steady state and transient fluid flow in porous media: Numerical analysis, *Water. Resour. Res.*, 26(5), 863–874, 1990.

Bear, J., *Dynamics of Fluids in Porous Media*, Elsevier Sci., New York, 1972.

Beckie, R., Measurement scale, network sampling, and groundwater model parameters, *Water. Resour. Res.*, 32(1), 65–76, 1996.

Boufadel, M.C., L. Silong, F.J. Molz, D. Lavallee, Multifractal scaling of the intrinsic permeability, *Water. Resour. Res.*, 36(11), 3211–3222, 2000.

Brace, W.F., Permeability of crystalline rocks: New in situe measurements, *J. Geophys. Res.*, 89(B6), 4327–4330, 1984.

Bracewell, R.N., *The Fourier Transform and it Applications, 3rd ed.*, McGraw-Hill, New York, 2000.

Briggs, W.L. and V.E. Henson, *The DFT: An Owner's Manual for the Discrete Fourier Transform*, SIAM, Philadelphia, 1995.

Chapin, M., *Thesis Title*, M.S. Thesis, Geology, New Mexico Institute of Mining and Technology, Socorro, New Mexico, 2001.

Chen, Z., *Mathematical Basis for Permeability and Porosity Measurements by Minipermeameters*, M.S. Thesis, Petroleum Engineering Department, New Mexico Institute of Mining and Technology, Socorro, New Mexico, 1992.

Clauser, C., Permeability of crystalline rocks, *Eos. Trans. AGU*, 73(21), 233, 1992.

Cushman, J.H., On measurement, scale and scaling, *Water. Resour. Res.*, 22(2), 129–134, 1986.

Davis, J.M, J.L. Wilson, and F.M. Phillips, A portable air-minipermeameter for rapid *in situ* field measurements, *Ground Water*, 32(2), 258–266, 1994.

Desbarats, A.J., Numerical estimation of effective permeability in sand-shale formations, *Water. Resour. Res.*, 23(2), 273–286, 1987.

Desbarats, A.J., Spatial averaging of hydraulic conductivity in three-dimensional heterogeneous porous media, *Math. Geol.*, 24(3), 249–267, 1992.

Deutsch, C.V. and A.G. Journel,*GSLIB, Geostatistical Software Library and User's Guide*, Oxford Univ. Press, New York, 1992.

Di Frederico, V. and S.P. Neuman, Scaling of random fields by means of truncated power variograms and associated spectra, *Water. Resour. Res.*, 33(5), 1075–1085, 1997.

Durlofsky, L.J., Representation of grid-block permeability in coarse scale models of randomly heterogeneous porous media, *Water. Resour. Res.*, 28(7), 1791–1800, 1992.

Dykaar, B.B. and P.K. Kitanidis, Determination of the effective hydraulic conductivity for heterogeneous porous media using a numerical spectral approach 1: Method, *Water. Resour. Res.*, 28(4), 1155–1166, 1992a.

Dykaar, B.B. and P.K. Kitanidis, Determination of the effective hydraulic conductivity for heterogeneous porous media using a numerical spectral approach 1: Results, *Water. Resour. Res.*, 28(4), 1167–1178, 1992b.

Gelhar, L.W., and C.L. Axness, Three-dimensional stochastic analysis of macrodispersion in aquifers, *Water. Resour. Res.*, 28(7), 1955–1974, 1983.

Gill, P.E., M.H. Murray, and W. Wright, *Numerical Linear Algebra*, Addison-Wesley, New York, 1990.

Goggin, D.J., R.L. Thrasher, and L.W. Lake, A theoretical and experimental analysis of minipermeameter response including gas slippage and high velocity flow effects, *In Situ*, 12(1-2), 79–116, 1988.

Gomez-Hernandez, J.J. and S.M. Gorelick, Effective groundwater model parameter values: Influence of spatial variability of hydraulic conductivity, leakance, and recharge, *Water. Resour. Res.*, 25(3), 405–419, 1989.

Gutjahr, A.L., L.W. Gelhar, A.A. Bakr, and J.R. Macmillan, Stochastic analysis of spatial variability in subsurface flows, 2, Evaluation and application, *Water. Resour. Res.*, 14(5), 953–960, 1978.

Hanor, J.s., Effective hydraulic conductivity of fractured clay beds at a hazardous waste landfill, Louisiana Gulf Coast, *Water. Resour. Res.*, 29(11), 3691–3698, 1993.

Indelman, P. and G. Dagan, Upscaling of heterogeneous formations: General approach and application to isotropic porous media, *Transport in Porous Media*, 12,61–183, 1993.

Journel and Huijbregts, *Mining Geostatistics*, Academic Press, New York, 1978.

anduau, L.D., and E.M. Lifshitz, *Electrodynamics of Continuous Media*, Pergamon, New York, 1960.

Liu, H.H. and F.J. Molz, Multifractal analyses of hydraulic conductivity distributions, *Water. Resour. Res.*, 33(11), 2483–2488, 1997.

Matheron, G., *Les Variables Regionalisees et Leur Estimation*, Masson, Paris, 1967.

Molz, F.J., C.L. Dinwiddie, and J.L. Wilson, What does an instrument measure? A physical basis for calculating spatial weighting functions applicable to hydraulic conductivity and intrinsic permeability measurements, *Water. Resour. Res.*, 39(4), 1096–????, 2003.

Neuman, S.P., Universal scaling of hydraulic conductivities and dispersivities in geologic media, *Water. Resour. Res.*, 1990.

Neuman, S.P. and S. Orr, Prediction of steady state flow in nonuniform geologic media by conditional moments: Exact nonlocal formalism, effective conductivities, and weak approximation, *Water. Resour. Res.*, 29(2), 341–364, 1993.

Parker, J.C. and K.A. Albrecht, Sample volume effects on solute transport predictions, *Water. Resour. Res.*, 23(12), 2293–2301, 1987.

Pyrcz, M.J. and C.V. Deutsch, The whole story on the hole effect, *Geostatistical Association of Australasia*, 18,May 2003.

Renard, P. and G. de Marsily, Calculating equivalent permeability: A review, *Advances in Water Resources*, 20(5,6), 253–278, 1997.

Rubin, Y. and J.J. Gomez-Hernandez, A stochastic approach to the problem of upscaling of conductivity in disordered media: Theory and unconditional numerical simulations, *Water. Resour. Res.*, 26(4), 691–701, 1990.

Sanchez-Vila, X., Radially convergent flow in heterogeneous porous media, *Water. Resour. Res.*, 33(7), 1633–1641, 1997.

Suboor, M.A. and J.P. Heller, Minipermeameter characteristics critical to its use, *In Situ*, 19(3), 225–248, 1995.

Schulze-Makuch, D. and D.S. Cherkauer, Method developed for extrapolating scale behavior, *Eos. Trans. AGU*, 78(1), 3, 1997.

Tidwell, V.C. and J.L. Wilson, Laboratory method for investigating permeability upscaling, *Water. Resour. Res.*, 30(7), 1607–1616, 1997.

Tidwell, V.C. and J.L. Wilson, Permeability upscaling measured on a block of Berea Sandstone: Results and interpretation, *Math. Geol.*, 31(7), 749–769, 1999a.

Tidwell, V.C. and J.L. Wilson, Upscaling experiments conducted on a block of volcanic tuff: Results for a bimodal permeability distribution, *Water. Resour. Res.*, 35(11), 3375–3387, 1999b.

Tidwell, V.C., A.L. Gutjahr, and J.L. Wilson, What does an instrument measure? Empirical spatial weighting functions calculated from permeability data sets measured on multiple sample supports, *Water. Resour. Res.*, 35(1), 43–54, 1999.

Tidwell, V.C. and J.L. Wilson, Heterogeneity, permeability patterns, and permeability upscaling: Physical characterization of a block of Massillon sandstone exhibiting nested scales of heterogeneity, *SPE Reservoir Evaluation and Engineering*, 4(3), 283–292, 2000.

Warren, J.E. and H.S. Price, Flow in heterogeneous porous media, *SPE J.*, 1, 153–169, 1961.

Winterbottom, F.A., *Numerical modeling of a minipermeameter*, M.Engr. Thesis, Heriot-Watt University, Edinburgh, 1990.